

DTIC FILE COPY

2

AFGL-TR-89-0008

Analysis of Teleseismic P Wave Amplitude
and Coda Variations for Underground Explosions

Thorne Lay
Christopher S. Lynnes
Brian Cohee

University of Michigan
Department of Geological Sciences
Ann Arbor, MI 48109-1063

1 January 1989

Final Report
1 January 1987-31 December 1988

APPROVED FOR PUBLIC RELEASE; DISTRIBUTION UNLIMITED

AIR FORCE GEOPHYSICS LABORATORY
AIR FORCE SYSTEMS COMMAND
UNITED STATES AIR FORCE
HANSCOM AIR FORCE BASE, MASSACHUSETTS 01731-5000

DTIC
ELECTE
S 3 APR 1989 D
E

89 4 08 091

AD-A206 231

Unclassified

SECURITY CLASSIFICATION OF THIS PAGE

REPORT DOCUMENTATION PAGE

1a. REPORT SECURITY CLASSIFICATION Unclassified		1b. RESTRICTIVE MARKINGS	
2a. SECURITY CLASSIFICATION AUTHORITY		3. DISTRIBUTION/AVAILABILITY OF REPORT Approved for Public Release: Distribution Unlimited	
2b. DECLASSIFICATION/DOWNGRADING SCHEDULE			
4. PERFORMING ORGANIZATION REPORT NUMBER(S) UM-TR-88-01		5. MONITORING ORGANIZATION REPORT NUMBER(S) AFGL-TR-89-0008	
6a. NAME OF PERFORMING ORGANIZATION University of Michigan	6b. OFFICE SYMBOL (If applicable)	7a. NAME OF MONITORING ORGANIZATION Air Force Geophysics Laboratory (LWT)	
6c. ADDRESS (City, State and ZIP Code) Department of Geological Sciences 1006 C. C. Little Bldg. Ann Arbor, Michigan 48109-1063		7b. ADDRESS (City, State and ZIP Code) Hanscom Air Force Base Massachusetts 01731-5000	
8a. NAME OF FUNDING/SPONSORING ORGANIZATION DARPA (DoD)	8b. OFFICE SYMBOL (If applicable)	9. PROCUREMENT INSTRUMENT IDENTIFICATION NUMBER F19628-87-X-0010	
8c. ADDRESS (City, State and ZIP Code) 1400 Wilson Blvd. Arlington, VA 22209-2308		10. SOURCE OF FUNDING NOS.	
		PROGRAM ELEMENT NO.	PROJECT NO.
		61101E	7A10
11. TITLE (Include Security Classification) Analysis of Teleseismic P Wave Amplitude and Coda Variations for (over)		TASK NO.	WORK UNIT NO.
		DA	CF
12. PERSONAL AUTHOR(S) Thorne Lay, Christopher S. Lynnes, Brian Cohee			
13a. TYPE OF REPORT Final Report	13b. TIME COVERED FROM 1 Jan 37 TO 31 Dec 88	14. DATE OF REPORT (Yr., Mo., Day) 1989 January 1	15. PAGE COUNT 126
16. SUPPLEMENTARY NOTATION Sponsored by Defense Advanced Research Projects Agency (DARPA), Defense Sciences Office, Geophysical Sciences Division, DARPA/DSO, Physical Characterizations of Seismic Sources, DARPA ORDER Number 5299			
17. COSATI CODES		18. SUBJECT TERMS (Continue on reverse if necessary and identify by block number)	
FIELD	GROUP	SUB. GR.	
		Explosion Seismology Tectonic Release	
		P Wave Coda Teleseismic P Waves	
19. ABSTRACT (Continue on reverse if necessary and identify by block number)			
<p>This report presents the results of four investigations, which have as their common goal, the development and application of techniques for determining near-source contributions to the observed variations in short-period P wave amplitudes, travel times, waveforms and coda for underground explosions.</p> <p>A waveform modeling analysis of long-period teleseismic SH and SV waves from two large underground explosions at the Southern Novaya Zemlya test site indicates that the appropriate equivalent double couple orientation for the tectonic release is vertical strike slip. Complete waveform modeling of the SV signals using the method of Baag and Langston allows us to distinguish between the strike slip and 45° dipping thrust geometries. The resulting mechanism and associated F-factors indicate that teleseismic P waves from these events are probably not strongly affected by tectonic release radiation, consistent with the previous coda and P wave amplitude analysis we conducted under our previous contract.</p> <p style="text-align: right;">(over)</p>			
20. DISTRIBUTION/AVAILABILITY OF ABSTRACT UNCLASSIFIED/UNLIMITED <input type="checkbox"/> SAME AS RPT <input type="checkbox"/> DTIC USERS <input type="checkbox"/>		21. ABSTRACT SECURITY CLASSIFICATION Unclassified	
22a. NAME OF RESPONSIBLE INDIVIDUAL James Leifowicz		22b. TELEPHONE NUMBER (Include Area Code) (617) 325-1111	22c. OFFICE SYMBOL AFGL-TR-89-0008

Cont. of Block 11:

Underground Explosions.

19. Continued

The early P wave coda of underground explosions at the Nevada Test Site has been studied using 2082 teleseismic short-period recordings. Small magnitude events tend to have relatively high coda levels in the 0.4-0.8 Hz frequency band for both Yucca Flat and Pahute Mesa explosions. This does not appear to be the result of signal-to-noise ratio variations, and requires enhanced scattering of lower frequency signals into the coda for the smaller events. The coda complexity is negatively correlated with burial depth for Pahute Mesa events, indicating that surface wave excitation may be a factor. Coda complexity in the 0.8-1.1 Hz passband is positively correlated with magnitude and depth for Pahute Mesa events, but has no such dependence for Yucca Flat tests. This observation is primarily due to pP interference for the largest of the Pahute Mesa events, but frequency dependent defocussing also appears to play a role. Strong azimuthal patterns are observed for both direct arrivals and early P coda, indicating a need for careful path corrections for coda magnitude estimates.

Analysis of 1020 teleseismic P waves from 32 Yucca Flat explosions has been conducted to establish our ability to identify the locations of any isotropic point scatterers in the near-source region. The procedure involves slant stacking the data to seek coherent arrivals in the coda. The coherency measure, semblance, is used. Numerous tests of potential resolution, array bias, and noise effects are conducted. Some coherent structure in the coda is detected, which may involve scattering of higher mode surface waves to P energy off of topography near Half Pint Mountain, or this may be the manifestation of random scattering contributions from very close to the sources which cannot be deterministically analyzed.

A very large data set of short period P wave amplitudes and travel times from the Nevada Test Site is inverted for thin lens models of upper mantle and deep crustal velocity heterogeneity below the test site. The observations exhibit systematic variations, with low amplitudes correlating weakly with fast travel times, which motivates the model parameterization. The stability of the thin lens results is tested by constructing synthetic seismograms using the Kirchhoff-Helmholtz method. Both the intersite (near-source) and intrasite (very near-source) amplitude differences between events are qualitatively well predicted. The travel time anomalies are underpredicted by the thin lens models which match the data, indicating that additional, very smooth velocity heterogeneity is present, but causes little amplitude anomaly. The interpretation of the amplitude patterns as resulting from focussing and defocussing rather than systematic tectonic release contamination is given further credibility by these results.

TABLE OF CONTENTS

	<u>Page</u>
Executive Summary	1
Section 1: Modeling Teleseismic SV Waves From Underground Explosions With Tectonic Release: Results for Southern Novaya Zemlya	2
Section 2: Observations of Teleseismic P Wave Coda for Underground Explosions	24
Section 3: Inversion of P Coda for Isotropic Scatterers at the Yucca Flat Test Site	44
Section 4: Effects of Lateral Velocity Heterogeneity Under the Nevada Test Site on Short Period P Wave Amplitudes and Travel Times	77

Accession For	
NTIS GRA&I	<input checked="" type="checkbox"/>
DTIC TAB	<input type="checkbox"/>
Unannounced	<input type="checkbox"/>
Justification	
By	
Distribution/	
Availability Codes	
Dist	Avail and/or Special
A-1	



EXECUTIVE SUMMARY

This document presents the results of a 24 month contract for data-intensive analysis of the amplitudes, travel times, and coda characteristics of teleseismic short period P waves from underground explosions. The basic objective of this line of research is to attain an understanding of the near-source contributions to the variability of the seismic observations. This will improve our fundamental understanding of the seismic radiation and provide guidance for improved yield estimation methodologies. In addition, analysis of the scattered wavefield in the P coda will lead to a better knowledge of scattering processes which dominate regional seismograms. The most basic contribution of this work has been the demonstration that even using teleseismic signals alone, it is possible to characterize near source effects on amplitudes and travel times for events in a given test site. The importance of upper mantle velocity heterogeneity is strongly demonstrated, as is the relative stability of P wave coda. We have made the first attempt to deterministically analyze near-source scattering in the P wave coda, as well as statistically documenting magnitude dependent relative anomalies between direct arrivals and P coda.

Section 1

Modeling Teleseismic SV Waves From Underground Explosions
With Tectonic Release: Results for Southern Novaya Zemlya

MODELING TELESEISMIC SV WAVES FROM UNDERGROUND EXPLOSIONS WITH TECTONIC RELEASE: RESULTS FOR SOUTHERN NOVAYA ZEMLYA

BY BRIAN P. COHEE AND THORNE LAY

ABSTRACT

Detailed forward modeling of long-period shear waves for two large underground explosions at the Southern Novaya Zemlya test site indicates that the appropriate equivalent double-couple orientation for the tectonic release radiation is vertical strike-slip. Previous studies of observed teleseismic *SH* waveforms and *SV* amplitudes for the 27 October 1973 and 2 November 1974 events using geometric ray theory could not distinguish between vertical strike-slip and 45°-dipping thrust geometries. Either mechanism can match the observed four-lobed *SH* radiation pattern, and the two-lobed *SV* amplitude pattern can be produced by interference with an appropriate size explosion *pS* signal. However, the complexity of the observed *SV* waveforms arising from *Sp* conversions near the receiver, diffracted *Sp*, and shear-coupled *PL* phases is not accounted for in the ray theory synthetics. Incorporating more realistic Green's functions using Baag and Langston's (1985b) WKBJ spectral method allows more complete modeling of the *SV* signals. Due to differences in frequency content between the explosion and double-couple *SV* waveforms, constructive interference occurs more efficiently than destructive interference when the two signals are linearly superimposed. As a result, using tectonic release moments determined from the *SH* waves and the optimum *F* factors required to match the *SV* amplitude patterns, the waveforms produced by the strike-slip and thrust orientations differ substantially at some azimuths. The strike-slip solution yields a consistently superior match to the data. Using the EU2 model of Lerner-Lam and Jordan (1987) for the source region and either EU2 or TNA (Grand and Helmberger, 1984) for the receiver structure, together with an attenuation model similar to SL8, we obtain a double-couple moment, $M_0 = 3.2 \times 10^{24}$ dyne-cm and explosion source strength, $\psi_s = 3.8 \pm 0.5 \times 10^{11}$ cm³ for the 27 October 1973 event, and $M_0 = 1.7 \times 10^{24}$ dyne-cm and $\psi_s = 2.0 \pm 0.3 \times 10^{11}$ cm³ for the 2 November 1974 event. Complete waveform modeling of *SV* signals can thus provide improved constraints on tectonic release radiation and explosion source strength.

INTRODUCTION

Numerous studies have addressed the existence of nonisotropic seismic radiation accompanying large underground nuclear explosions (e.g. Press and Archambeau, 1962; Toksöz *et al.*, 1965; Hirasawa, 1971; Wallace *et al.*, 1983, 1985). Long-period horizontal shear wave motions, including Love waves and teleseismic *SH* body waves, result directly from this nonisotropic component and can be used to constrain the transverse source contribution. Although many uncertainties remain concerning the precise physical source of this transverse energy, it is generally attributed to the release of preexisting tectonic strain accumulation in the vicinity of the explosion (tectonic release). Two general theories for tectonic release have been suggested: the triggering of displacement on a nearby fault (Brune and Pomeroy, 1963; Aki *et al.*, 1969; Aki and Tsai, 1972), or the release of *in situ* stress from vaporized and fractured rock during formation of the ex-

plosion cavity (Press and Archambeau, 1962; Archambeau and Sammis, 1970; Archambeau, 1972; Lambert *et al.*, 1972). For either tectonic release model, the long-period far-field radiation may be represented by an equivalent double-couple dislocation; however, it is challenging to find a unique focal mechanism solution.

The ambiguity intrinsic to determination of the tectonic release focal mechanism using long-period *S* waves was explored by Wallace *et al.* (1985). Both vertical strike-slip and 45°-dipping (thrust or normal) faults can produce identical four-lobed *SH* (and Love wave) radiation patterns, with the corresponding moments for the dip-slip mechanisms being doubled and strike azimuths being rotated $\pm 45^\circ$ relative to the strike-slip mechanism (see Aki and Tsai, 1972; Given and Mellman, 1985; Burger *et al.*, 1986b). As a result, uncertainty in the true orientation has direct consequences for the appraisal of long-period source amplitude and corresponding explosion strength. Wallace *et al.* (1985) demonstrate that this uncertainty cannot be resolved using *SH* data alone, but the inclusion of *SV* data can yield a unique model. Tectonic release studies incorporating both *SH* and *SV* waves have still been unable to uniquely resolve the double-couple orientation in cases (which are frequently encountered) where the focal mechanism is either vertical strike-slip or 45° dip-slip, because it has been difficult to quantitatively model the complex *SV* arrivals (Burger *et al.*, 1986b).

The complexity inherent in modeling *SV* wave propagation results from the contributions of additional phases within a 30-sec window containing the direct *S* arrival. *Sp* conversions occurring at the Moho and other discontinuities beneath the receiver immediately precede and obscure direct *S*. The long-period shear-coupled *PL* (*SPL*) phase, initially recognized and investigated by Oliver (1961), follows and often overshadows the initial pulse (Baag and Langston, 1985a). The *SPL* phase is set up as a normally dispersed leaking mode in the crustal wave guide with trapped *P* waves (leaking downgoing *S* energy) and *SV* reverberations. Diffracted *Sp* (Frazer, 1977) is a diffracted head wave set up at the base of the crust by a critically incident *S* wave, which arrives after direct *S* at distances greater than 50° (Baag and Langston, 1986). The propagation paths and characteristics of these auxiliary *SV* energy contributions are examined in more detail by Burdick and Langston (1977) and Baag and Langston (1985a, 1986). These additional phases are very sensitive to source and receiver structure, particularly for shallow sources, further complicating the analysis of explosion signals. The difficulty of interpreting the *SV* wave train has limited its use for source investigations. However, this very complexity contains potential for increased resolution of the tectonic release orientation if the wave field can be accurately computed.

In forward modeling of teleseismic signals from explosions with tectonic release, it is commonly assumed that both sources are coincident in space and time and can thus be represented by the linear superposition of the explosion and double-couple waveforms. This superposition necessitates dependable Green's functions to realistically account for interference between the two source signals.

Ray theory can be used to construct teleseismic *SH* and *SV* synthetics (Langston and Helmberger, 1975), which is usually sufficient to match the simple *SH* waveforms. However, the *SV* synthetics include only the direct geometric phases of the explosion (*pS*) and tectonic release (*S*, *sS*, *pS*) signals. At distances less than 60°, these are a poor approximation of the total *SV* arrival (Langston and Baag, 1985). A more complete calculation that includes *SPL*, *Sp* conversions, and diffracted *Sp*, and accounts for their excitation dependence on source type, is

required to model the complex interference between the two sources. A significant contribution to the understanding of the *SV* system at distances between 30° and 90° was recently made by Baag and Langston (1985a, b). A WKBJ spectral method for creating teleseismic synthetic *SV* waves was presented, which requires substantially less computation time than previously necessary to compute adequate Green's functions. The WKBJ spectral method couples WKBJ theory for a generalized ray in a vertically inhomogeneous half-space with the Watson (1970) compound-matrix technique in near-surface homogeneous layers at both the source and receiver. The validity of the method has been demonstrated through comparison with Kind's (1978) reflectivity treatment of the *P-SV* wave propagation equations (Baag and Langston, 1985b).

In this study, we construct synthetic *SV* waveforms to resolve the ambiguity of the double-couple orientation of tectonic release for two Soviet underground nuclear tests, 27 October 1973 and 2 November 1974, and to determine appropriate explosion and tectonic release source strengths. These two explosions are among a series of large underground nuclear tests conducted by the Soviet Union on the island of Novaya Zemlya in the Barents Sea (Figure 1). The tectonic release focal mechanisms for nine events at a northern site were found to be oblique

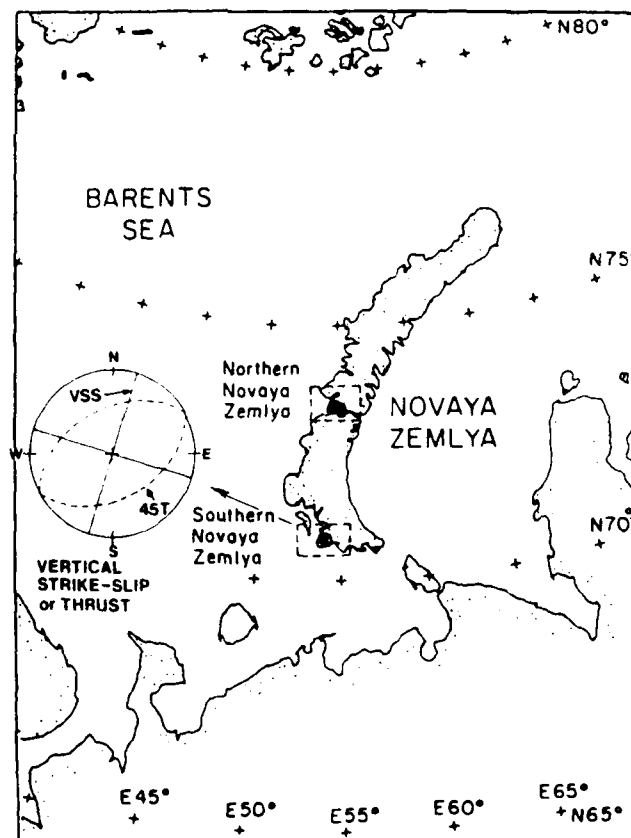


FIG. 1. Base map showing the two Novaya Zemlya test sites. The northern and southern test sites are separated by about 300 km. The two nuclear explosions analyzed in this study occurred at the southern site. The lower hemisphere projection shows *P*-wave radiation nodes for the two possible tectonic release orientations that satisfy the *SH* observations.

normal by Burger *et al.* (1986b) based on the *SH* radiation pattern. *SH* observations from the Southern Novaya Zemlya site however, could not distinguish between vertical strike-slip and 45° dip-slip double-couple orientations. Long-period, teleseismic *SV* waves for the 27 October 1973 and 2 November 1974 Southern Novaya Zemlya events are modeled to discern characteristic traits of each tectonic release double-couple and its interference with the explosion signal, and to resolve the true orientation by comparison with observed waveforms.

SHEAR WAVE OBSERVATIONS AND RAY THEORY MODELING

The 27 October 1973 and 2 November 1974 Southern Novaya Zemlya explosions are among the largest underground nuclear tests ever conducted (see Table 1). As a result, numerous long-period WWSSN and CSN records are available from teleseismic distances. Selected *SH* data for the 27 October 1973 event are shown in Figure 2. Systematic polarity reversals near 60°, 150°, 240°, and 330° define a four-lobed amplitude pattern with vertical nodal planes. Both vertical strike-slip and 45° dip-slip mechanisms are characterized by such an *SH* radiation pattern. The 2 November 1974 *SH* data are presented in a similar format by Burger *et al.* (1986b, Figure 3). Comparison of the observations for both explosions reveal a similar *SH* radiation, indicative of a common tectonic release orientation.

The simple *SH* pulses are well-modeled using ray theory for a half-space (Langston and Helmberger, 1975) and a point-source dislocation with a 3.0-sec duration trapezoid source-time function (1 sec rise, 1 sec top, 1 sec fall) convolved with an appropriate 15–100 WWSSN instrument response. Source depth was placed at 1 km. The assignment of additional model parameters (*P* velocity, $\alpha = 6.08$ km/sec; *S* velocity, $\beta = 3.5$ km/sec; density, $\rho = 2.74$ gm/cm³; and Futterman attenuation operator, $t_3^* = 4.5$ sec) strongly affects the moment required to match the observed *SH* amplitudes. These parameters are poorly constrained due to uncertainty regarding the appropriate source structure and attenuation for the mantle. The input parameters for the *SH* synthetics differ from those used by Burger *et al.* (1986b) in order to be consistent with the EU2 structure (Lerner-Lam and Jordan, 1987) adopted later in the more involved WKB spectral *SV* modeling. The moments in Figure 2 are the values required to match the observed peak-to-peak 27 October 1973 *SH* amplitudes with the strike-slip solution (strike $\phi = 287^\circ$; dip, $\delta = 90^\circ$; rake, $\lambda = 0^\circ$). Twenty-seven nonnodal stations yield an average double-couple moment of 3.2×10^{24} dyne-cm for 27 October 1973 and 1.7×10^{24} dyne-cm (20 nonnodal observations) for the 2 November 1974 event.

TABLE 1
EVENT INFORMATION*

	27 October 1973	2 November 1974
Date	27 October 1973	2 November 1974
UTC	06:59:57	04:59:57
Latitude (°N)	70.78	70.82
Longitude (°E)	54.18	54.18
m_s	6.94 ± 0.018	6.78 ± 0.020
M_s	5.51 ± 0.052	5.29 ± 0.040
m_s yield (kt)	4050	2100
M_s yield (kt)	2840	1690
Average yield (kt)	3450 ± 610	1890 ± 210

* Locations are from Dahlman and Israelson (1977). Magnitudes and yields are from Bykes and Wiggins (1986).

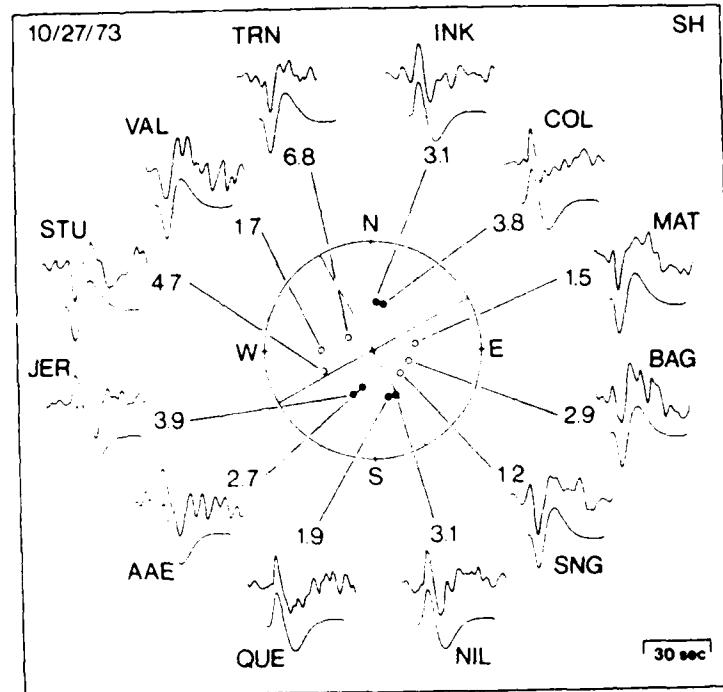


FIG. 2. Long-period *SH* observations and half space synthetics for the 27 October 1973 explosion. Numbers are the moments required to match the observed amplitudes at each station ($\times 10^{24}$ dyne-cm). The lower hemisphere, equal-area projection shows the *SH* first motions (filled circles are clockwise) and the *SH* radiation nodes for the vertical strike-slip mechanism.

These moments are both twice as large as the values found by Burger *et al.* (1986b), due primarily to the faster source velocity used in our synthetics. The tectonic release moment for the 1973 event is 1.9 times larger than that for the 1974 explosion. The same amplitude ratio is also found for the long-period *P* and *SV* amplitudes at common stations for the two events (Burger *et al.*, 1986b).

In order to decide which mechanism is correct, it is necessary to model the *SV* data. The observed *SV* waveforms are remarkably similar for both events, even 60 sec after the initial *S* arrival. This is demonstrated in Figure 3 where selected radial and vertical *SV* observations from each event are compared. The waveform similarity further establishes the consistency of the tectonic release orientation for both explosions as well as the stability of the *SV* wave field. Note that the *SV* energy is distributed over a long time window, unlike the simple *SH* pulses in Figure 2, and that the first arrival waveforms vary substantially. The azimuthal dependence of the direct *S* arrival is masked by variation in the long-period *SPL* amplitudes, which are primarily attributable to variations in receiver structure and epicentral distance. Note also the prograde elliptical polarization of the *SPL* phase (Figure 3). A more complete azimuthal coverage of the observed radial *SV* data for the 27 October 1973 event is presented in Figure 4. The amplitudes shown are peak-to-peak measurements of direct *S* in millimicrons ($m\mu$) normalized to 50° distance by a geometric spreading correction (Langston and Helmberger, 1975). The direct *S* amplitudes display a clear two-lobed azimuthal pattern, with weak arrivals near 152° and 332° (NIL, AAM) and large amplitudes near 62° and 242° (COL, COP). The amplitude variation of the initial *S* arrival

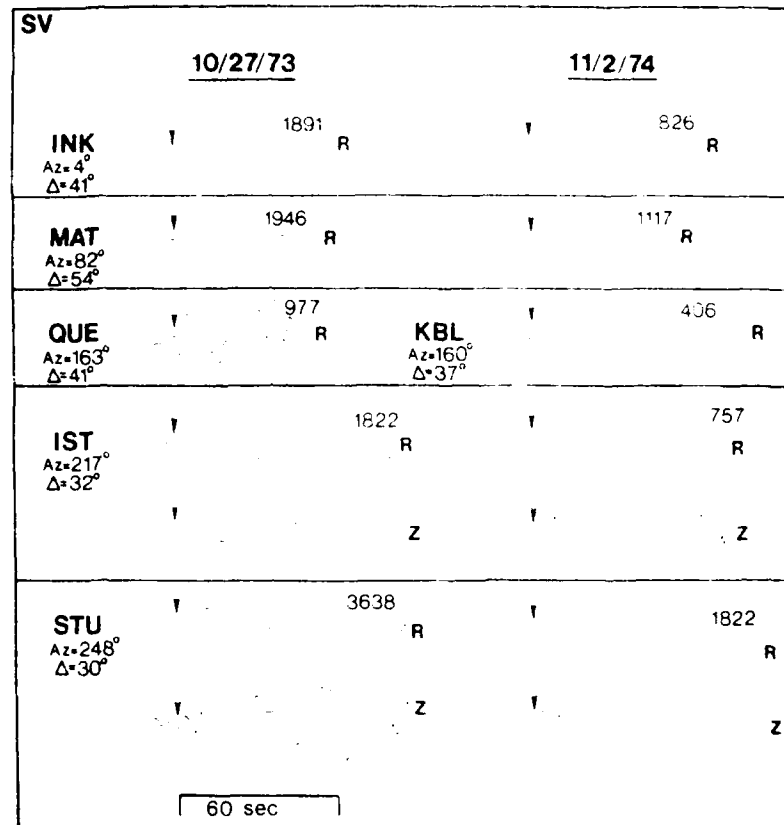


FIG. 3. Long-period radial (R) and vertical (Z) component SV observations for 27 October 1973 and 2 November 1974 explosions. Downward motion on the radial components indicates motion toward the source. The numbers are direct S peak-to-peak amplitudes in millimicrons corrected for geometric spreading to 50° distance. Arrows indicate the arrival time of the direct S pulse. The long-period oscillations later in the waveform are the SPL phase.

cannot be attributed to variations of receiver structure, and instead, must represent interference between the explosion and tectonic release signals. Burger *et al.* (1986b, Figure 4) show a corresponding figure with numerous radial SV signals for the 2 November 1974 explosion, which have very similar wave shapes.

While recognizing the limitations of ray theory for SV signals, we generated SV half-space synthetics, including the explosion (*pS*) and tectonic release arrivals (*S*, *sS*, *pS*) to identify first-order interference effects. These synthetics are constructed with the same parameters used in the *SH* modeling. The explosion is represented by a modified Haskell bomb source (Helmberger and Hadley, 1981) constructed using an overshoot parameter $B = 0.1$ and rise time parameter $K = 7.5 \text{ sec}^{-1}$. The long-period explosion SV synthetics are not especially sensitive to the choice of B and K ; however, these values are in agreement with the *P* wave modeling by Burger *et al.* (1986b) for the same two events.

The polarity of the radial component of direct *S* for the normal fault solution is toward the source at all azimuths, the same as for the explosion (*pS*) pulse. Accordingly, the two signals constructively interfere in the first cycle of the direct *S* arrival, and the amplitude of the smallest observed SV waves near azimuths of 152° and 332° must represent the size of the explosion signal alone. Thus, the

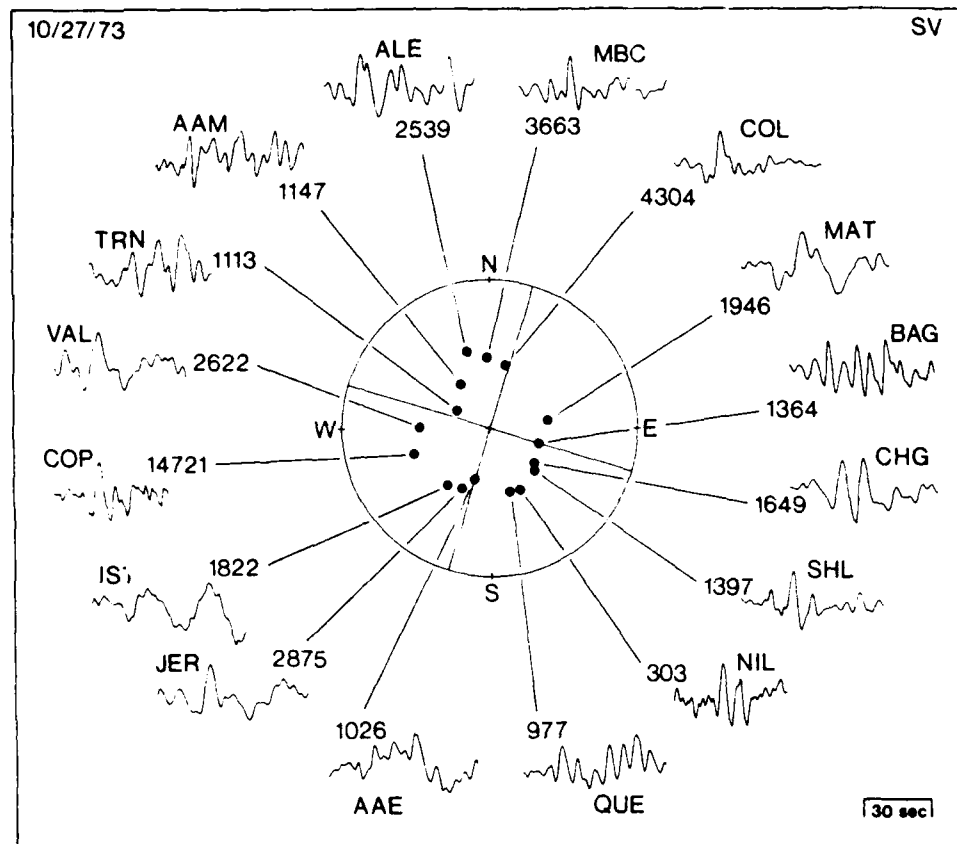


FIG. 4. Long-period radial component SV observations for 27 October 1973. The numbers are the observed peak-to-peak amplitudes of direct S in millimicrons normalized to 50° distance using a geometric spreading correction. The lower hemisphere, equal-area projection shows the location of each observation and the SV radiation nodes for the strike-slip mechanism. The large amplitude at COP ($\Delta = 23^\circ$) results from an upper mantle triplication.

explosion source strength, ψ_x , for the 45° normal fault solution must be negligible to produce the observed radiation pattern which has clear nodes. Due to this, and additional problems discussed later with the WKB spectral modeling, the normal solution is deemed inappropriate.

Ray theory SV waveforms for the explosion and the two remaining plausible double-couple orientations, are shown separately and superimposed in Figure 5. In each case, the explosion pS amplitude is adjusted to achieve the desired two-lobed radiation pattern and to match the observed 27 October 1973 amplitudes at 50° distance. All amplitudes are 1.9 times smaller for the 2 November 1974 event. Both double-couple orientations, when combined with the explosion source, can produce the basic amplitude variation observed in the data; however, the azimuthal interference behavior differs for the two mechanisms. The shape of the Green's function for the thrust solution is very similar to the strike-slip solution in the destructive (upward direct S) lobe ($\phi = 242^\circ$). The Green's function for the strike-slip solution in the constructive (downward direct S) lobe ($\phi = 332^\circ$) is also similar, but with opposite polarity. One might expect that the similarity of the double-couple waveforms over two out of four quadrants would com-

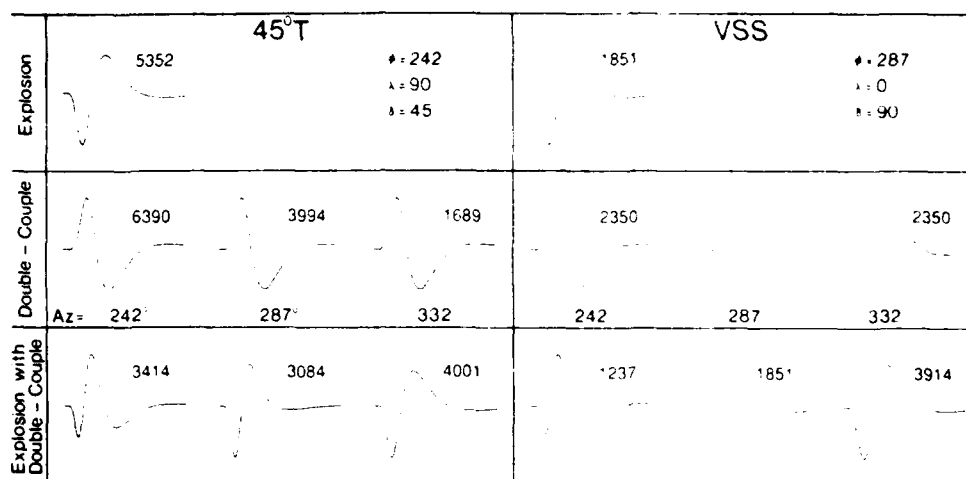


FIG. 5. Half-space radial component SV synthetics at 50° distance showing first-order interference effects between the explosion signal and the 45° -dipping thrust (left) and vertical strike-slip (right) tectonic release solutions. The focal mechanism parameters (strike, ϕ ; rake, λ ; dip, δ) and azimuths are appropriate for the Southern Novaya Zemlya test site. The top row depicts the explosion waveform alone with the peak-to-peak amplitude in millimicrons required to produce the observed SV radiation pattern for the 27 October 1973 event. The double-couple synthetics at various azimuths are shown in the middle row, and the waveforms resulting from superposition of the explosion and double-couple radiation are shown in the bottom row.

pligate efforts to distinguish between the two solutions, regardless of the presence of additional SV phases. Indeed, for stations in the two destructive strike-slip quadrants, no preference can be made for either choice of focal mechanism, even for more complete SV synthetics. However, as will be shown, the observations in the constructive lobes of the strike-slip solution allow identification of the true tectonic release orientation.

The thrust double-couple solution ($\phi = 242^\circ$, $\delta = 45^\circ$, $\lambda = 90^\circ$) for the half-space ($M_0 = 6.5 \times 10^{24}$ dyne-cm, $\psi_s = 8.7 \times 10^{11}$ cm³) has an upward first motion over all azimuths, opposite that of the explosion signal, resulting in dominantly destructive interference. The slight differences in the thrust and explosion waveforms result in destructive interference behaving less efficiently than constructive interference. However, this interference is very sensitive to the time alignment of the explosion and double-couple arrivals, which is poorly known. Small time shifts can cause much smaller amplitudes at an azimuth of 242° .

The SV waves for the strike-slip solution ($M_0 = 3.2 \times 10^{24}$ dyne-cm, $\psi_s = 3.2 \times 10^{11}$ cm³) have a $\sin 2\theta$ radiation pattern. This results in alternating lobes of constructive and destructive interference in the first cycle of the combined explosion plus double-couple synthetics. Figure 5 shows the relevant half-space synthetics for the strike-slip solution. The ψ_s for the strike-slip case is only 37 per cent of the thrust case, indicating the importance of determining the correct focal mechanism. The explosion alone must contribute the energy observed at the strike-slip nodes, thus, ψ_s is constrained to generate an amplitude of ≈ 1900 m μ , corresponding to the average observed value at the strike-slip nodal azimuths. The synthetic SV amplitude pattern for the strike-slip case matches the data reasonably well for both events, as shown in Figure 6. The asymmetry in the SV amplitude pattern is caused by a slight reversal of the first motion in the

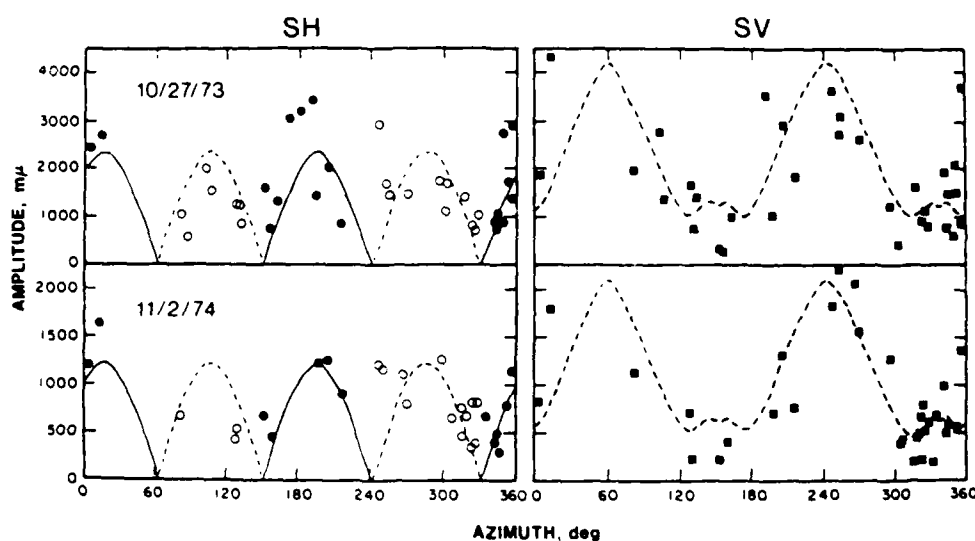


FIG. 6. Observed and half-space synthetic *SH* and *SV* amplitude patterns for the 27 October 1973 and 2 November 1974 events corrected for geometric spreading to a distance of 50° . The source model for the synthetic amplitudes is the explosion plus strike-slip tectonic release model.

destructive quadrants. The synthetic amplitudes of the explosion plus thrust solution do not fit the observed pattern as well, but can be made to do so by slight adjustment (≈ 1 sec) of the relative timing of the arrivals. Thus, for the ray theory *SV* synthetics, either solution is equally viable. The synthetic *SH* amplitudes and polarities over the full azimuthal range also closely match the observations and are presented in Figure 6. The large number of observations for both events narrowly constrain the possible focal mechanisms. It is evident from the similarity of interference that both events had a tectonic release component with the same orientation.

The *SV* ray theory modeling has eliminated the normal fault tectonic release orientation; however, it does not discriminate between the thrust and strike-slip solutions. Clearly, the radial *SV* waveforms in Figures 3 and 4 do not resemble the simple synthetics of Figure 5 for either solution. It is necessary to enlarge the time window under consideration and include the additional phases of *SV* wave propagation to reveal any diagnostic interference behavior of the two possible focal mechanisms. To accomplish this, the WKB spectral method may be applied to the *SV* propagation problem.

WKB SPECTRAL MODELING

Baag and Langston (1985b) coupled WKB theory for a generalized ray with the Watson compound-matrix method to generate a computationally efficient, accurate treatment of *SV* wave propagation. The method is based on Frazer (1977), but also includes anelasticity, parameterized as complex-valued velocity, and near-source reverberations that contribute downgoing *S* energy, particularly for shallow sources. A depth is chosen for coupling the propagator matrix with the generalized rays, so as to include the upper mantle regions with strong velocity gradients and low-velocity zones in the near-surface layers. Since *SPL* spends a large amount of time in the crustal wave guide through multiple reflections and *P-S* conversions, the choice of velocity model is important. Diffracted

S_p is likewise sensitive to crustal structure. The earth model is discretized above the coupling boundary into homogeneous layers and smoothed below to form a continuous, vertically inhomogeneous structure. The calculated downgoing reflectivity potential is used as the impulse for the WKBJ treatment. The range of ray parameter is chosen so as to include only those rays that turn below the coupled boundary in the WKBJ domain. The upgoing WKBJ ray is eventually converted to the propagator matrix coefficient and evaluated in the near-receiver layers. An earth flattening transformation of the earth structure is used for treatment in a cylindrical coordinate system (Chapman, 1973; Müller, 1977), and the solution is evaluated in the frequency domain over a designated range of real-valued wavenumbers. The resulting Green's function is then convolved with an appropriate source-time function and instrument response, and inverse Fourier transformed to produce displacements in the time domain.

The WKBJ spectral method requires specification of numerous parameters to constrain the earth model, source type, and various computational options. Three earth models were considered in this study: the EU2 model of Lerner-Lam and Jordan (1987), and models TNA and SNA of Grand and Helmberger (1984). These three structures are shown to 600 km depth in Figure 7. Below this depth, the three models have the same shear velocity. The TNA and SNA structures are extended down to the core-mantle boundary with the Jeffreys-Bullen-A (JBA) model. Since it is not necessary to compute P potentials deep in the mantle for teleseismic SV waves, the P -wave velocity is only defined in the homogeneous near-surface layers. For the TNA and SNA models, the P -wave velocity structure is prescribed by the JBA model. The SV wave train is sensitive to crustal structure and each of the three earth models promote unique behavior; thus, it was desired to use one model for the majority of the modeling in order to isolate structural effects from other variables. As shown in Figure 7, the EU2 model generally has velocities intermediate between TNA and SNA. Additionally, EU2 was formulated by a waveform inversion of fundamental and higher mode Rayleigh waves propagating across northern Eurasia. Accordingly, it seems appropriate to use

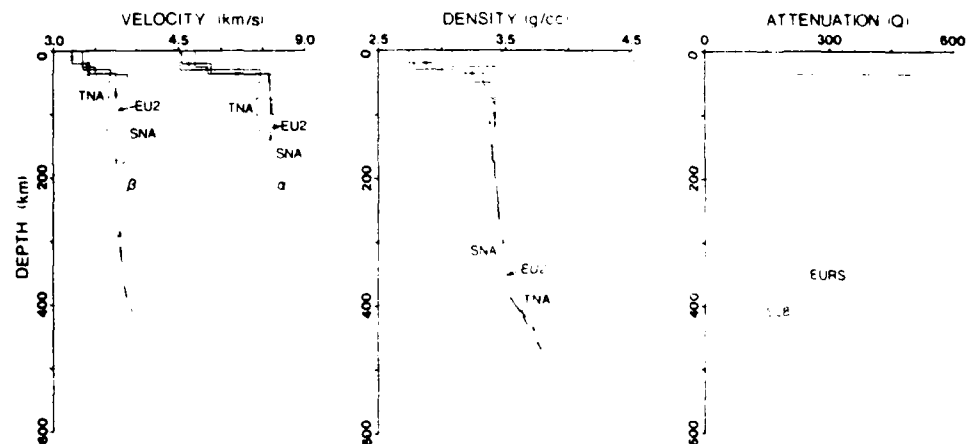


FIG. 7. Seismic velocity and density for the EU2, TNA, and SNA earth models and the modified SL8 and EURS attenuation structures. While the velocity and density of the three models are equivalent below 600 km, the EURS Q model continues to diverge from the modified SL8 model below this depth.

EU2 for the Novaya Zemlya source structure throughout the modeling, and whenever possible for the receiver structure.

A Q structure similar to SL8 (Anderson and Hart, 1978) was used in all synthetics (Figure 7). The effects of the frequency-dependent Q model (EURS) of Der *et al.* (1986), formulated from seismic observations for Eurasian seismic paths, are addressed later in the "Discussion." The boundary between the homogeneous layers and the vertically inhomogeneous half-space is set at 200 km depth to keep the WKBJ ray turning smoothly below the strong velocity gradients and low-velocity zone in the crust. The source depth is placed at 1 km for both the explosion and the tectonic release component. Although the depth of the double-couple source is not constrained as well as for the explosion, there is no evidence for distinct depth phase arrivals in either the SH or SV data. Depths from 0.5 to 1.5 km were also explored, but the effect on the waveforms and amplitudes is negligible. This is not particularly surprising considering the limited resolution of the synthetic Green's functions, which are calculated with 128 frequency points and a 2.0-sec sampling interval. This coarse sampling rate was found to be adequate for our comparisons with long-period data. The higher frequency information is not crucial to our understanding of the general wave behavior, and the additional computation time required for a smaller sampling interval is not justified. Because the convolution of the source-time function and instrument response is discretized at a 2.0-sec interval, longer duration source-time functions are preferred to avoid sampling errors. As before, a 3.0-sec trapezoid is used for the tectonic release component source-time function, and a modified Haskell bomb source with $B = 0.1$, and $K = 7.5 \text{ sec}^{-1}$ describes the isotropic source component. These source-time functions are consistent with results from relative waveform analysis by Burger *et al.* (1986a) for the Southern Novaya Zemlya explosions. Although the sensitivity of the synthetics to the different source-time functions is limited, care has been exercised to maintain the absolute amplitude information for each source.

For the purposes of this study, we have restricted our attention to observations in the distance range of 30° to 60° . The different sources considered here are most distinct in this distance range. Beyond 60° , the SV phases other than direct S become less important and the SV waveforms can be accurately represented with ray theory modeling (Langston and Baag, 1985). Furthermore, receivers between 30° and 60° are not influenced by upper mantle triplications or ScS and SKS phases. Vertical and radial components of the WKBJ spectral synthetics for both the explosion and double-couple sources are displayed in Figure 8 for the EU2 source and receiver structure. In Figure 8, the double-couple waveforms shown correspond to either the thrust signals at all azimuths or the destructive quadrants of the strike-slip solution. Recall that the shape of the Green's function for the thrust solution at all azimuths is very similar to that of the strike-slip solution in the two destructive quadrants. The Green's function for the strike-slip solution in the constructive lobe also has the same shape, but with opposite polarity.

The important phases of the SV wave train are identified in Figure 8. The Sp conversion immediately precedes S as a small amplitude arrival of opposite polarity on the radial component. The exact timing and strength of the Sp arrival are dependent on crustal velocities and depths to velocity discontinuities under the receiver. This phenomenon of Sp precursors to direct S has been investigated by Jordan and Frazer (1975) and Burdick and Langston (1977) as a means of discerning receiver structure. The long-period SPL phase is frequently the most

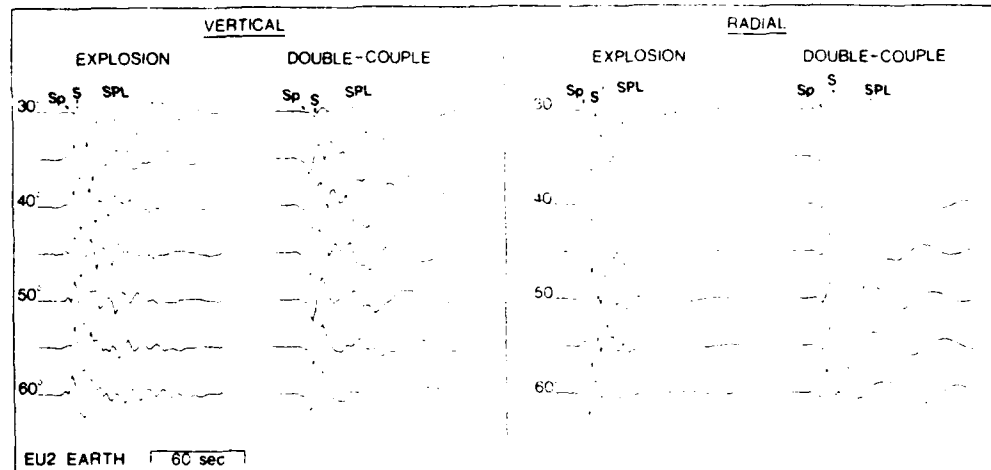


FIG. 8. Vertical and radial SV WKB spectral synthetics for the explosion and double-couple sources in the distance range 30° to 60°. The double-couple waveforms correspond to the thrust signals at all azimuths and the destructive quadrants of the strike-slip solution. The important phases of the SV wave train are identified except for diffracted *Sp*, which arrives after direct *S* at distances greater than 50°.

diagnostic feature of the SV wave train. The normal dispersion of the phase is evident over the 30° range shown, and the *SPL* amplitudes gradually decrease with greater distance. *SPL* is preferentially excited by the double-couple source relative to the explosion source, particularly at closer distances. Additionally, the overall synthetic explosion waveform contains more high frequency energy than the double-couple source. Even if the *Sp* precursor is ignored, the synthetics in Figure 8 are considerably different in the first 20 sec from the half-space synthetics shown in Figure 5. The rigorous treatment of the SV propagation problem afforded by the WKB spectral method produces synthetic waveforms that begin to include the complexities seen in Figures 3 and 4. The accurate computation of the Green's function becomes even more crucial when the two sources are superimposed. No time shift of the double-couple relative to the explosion source is utilized for any of the modeling, but small time shifts prove less important than in the half-space modeling because we are comparing the full waveform.

The two focal mechanisms combined with an appropriate size explosion source are shown in Figure 9 over a 90° azimuthal range. In comparison to the ray theory amplitudes, the WKB spectral method amplitudes for the thrust solution ($M_0 = 6.5 \times 10^{24}$ dyne-cm, $\psi_x = 3.8 \pm 0.6 \times 10^{11}$ cm³) better match the variation seen in the data (Figure 6), and the ψ_x required to accomplish this is less than half of the half-space value. This change in ψ_x can be attributed to components in the WKB spectral waveforms producing slightly more efficient destructive interference effects than are possible with the half-space modeling. The strike-slip solution ($M_0 = 3.2 \times 10^{24}$ dyne-cm, $\psi_x = 3.8 \pm 0.5 \times 10^{11}$ cm³) also matches the amplitude variation of Figure 6, but ψ_x is roughly the same as for the half-space modeling.

The synthetic seismograms of Figures 8 and 9 were constructed using an EU2 earth structure. The suitability of EU2 for the source structure has been discussed. As a receiver structure, EU2 performs satisfactorily in most cases, and

1170

BRIAN P. COHEE AND THORNE LAY

a constant receiver structure is preferred to isolate the interference effects of each solution. However, the relationship between receiver structure and the resulting SV phases is quite complicated, and it is therefore necessary to examine different source-receiver paths to establish the structural effects. Figure 10 depicts WKB spectral seismograms for the strike-slip solution combined with the explosion at 40° distance for numerous source-receiver structural combinations. Throughout this modeling, the source depth is maintained at 1 km, and as a

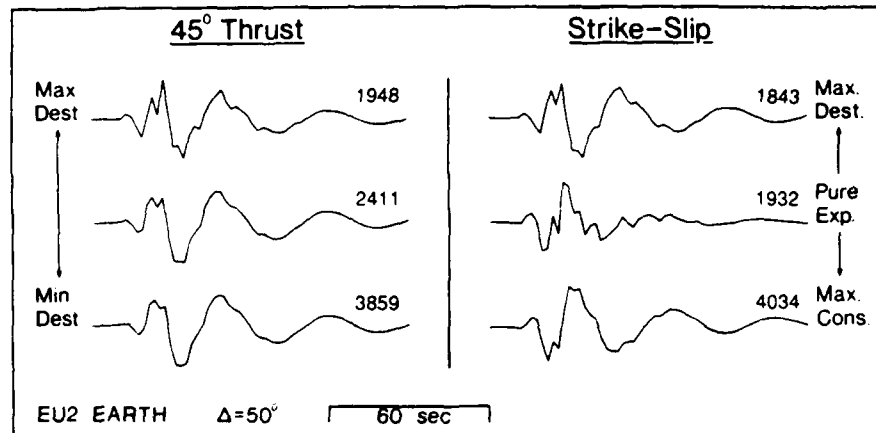


FIG. 9. Radial SV WKB spectral synthetics for each tectonic release solution combined with an appropriate size explosion over a representative 90° azimuthal range. The 45°-dipping thrust signal interferes destructively with the explosion at all azimuths. The four-lobed strike-slip solution signal alternates between destructive and constructive interference in opposite lobes. The amplitudes are in millimicrons and are appropriate for the 27 October 1973 event.

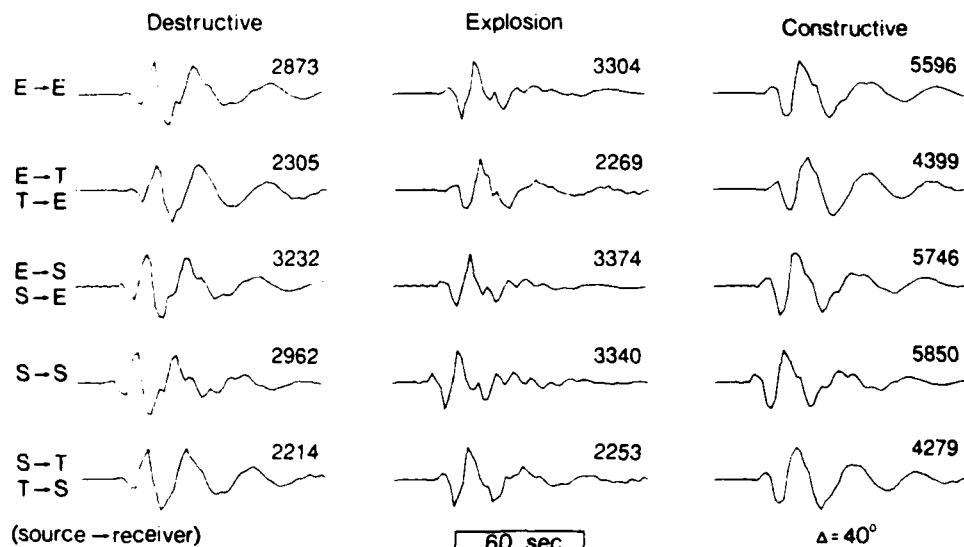


FIG. 10. Radial SV WKB spectral synthetics for the strike-slip solution superimposed with the explosion signal for various source-receiver structural combinations (E, EU2; T, TNA; S, SNA). The waveforms are equivalent when source and receiver structures are exchanged due to near-reciprocity with a 1 km source depth. Numbers are peak-to-peak amplitudes in millimicrons for a distance of 40°.

result, near-reciprocity exists when source and receiver structures are interchanged. Furthermore, this near-reciprocity indicates that source and receiver structures are equally important in the resultant seismogram for shallow sources. The waveforms in Figure 10 differ most dramatically in the relative excitation of the *SPL* phase, the timing of the initial arrival, and the peak-to-peak direct *S* amplitudes. The variance in amplitude and arrival time is an expected result of the different velocities of each structural combination. The amplitude information in Figure 10 does not help constrain the appropriate earth structure, since source strengths may be weighted accordingly to fit the observations. Likewise, the timing of the initial *S* arrival is not resolved well enough in the observations for diagnostic analysis. Relative excitation of the *SPL* phase, however, may be used to distinguish earth structure. With an EU2 source structure, the EU2 and SNA receiver structures yield nearly identical wave shapes and amplitudes. The TNA receiver structure increases *SPL* relative to direct *S* more than SNA or EU2 for the distance range considered. This result differs from that of Baag and Langston (1985a) who found SNA excited *SPL* more than TNA. This apparent inconsistency results from the longer period 30–100 ($T_0 = 30$ sec, $t_g = 100$ sec) WWSSN instrument and long-duration $\left(\exp \left\{ -\frac{1}{t} - \frac{t}{3} \right\} H(t) \right)$ source-time function used in their synthetics.

An additional complication for modeling the Novaya Zemlya data is the assumption of lateral homogeneity in earth structure. Evidence has been presented for the existence of strong lateral variations in upper mantle velocities underlying western Eurasia (England *et al.*, 1977; Rial *et al.*, 1984). Lateral heterogeneity within the source or receiver structure could perturb the SV waveform in a manner that is difficult to identify. Our modeling allows some flexibility in receiver structure that may in some cases account for lateral heterogeneity and other structural complexities. With the availability of representative Green's functions for the explosion and double-couple sources, and insight into the appropriate earth model and relative weighting necessary for each source to produce the observed amplitude variations, the task of isolating a preferred double-couple orientation may be approached.

COMPARISON OF SYNTHETIC AND OBSERVED WAVEFORMS

The strike-slip and thrust tectonic release orientations are combined with an appropriate size explosion source to produce the synthetic waveforms compared with the 27 October 1973 observations in Figure 11. The uniform shape of the two synthetic seismograms at POO and BLC are typical of a number of stations in the strike-slip destructive quadrants. For the 90° azimuth range spanned by each of these lobes, the interference of both tectonic release solutions is destructive, and the resulting waveforms are typically quite similar, suppressing any preference for either solution. However, the observed waveforms at all of the other stations are clearly matched better by the strike-slip solution. In fact, the azimuthal range where the strike-slip solution is preferred actually extends out of the 180° range that defines the constructive lobes. Stations in the destructive quadrants located near the strike-slip nodes (INK) contain relative source contributions that are still considerably different from the thrust solution. For all stations where the two double-couple solutions produce distinct waveforms, the strike-slip orientation consistently produces superior matches with the observed

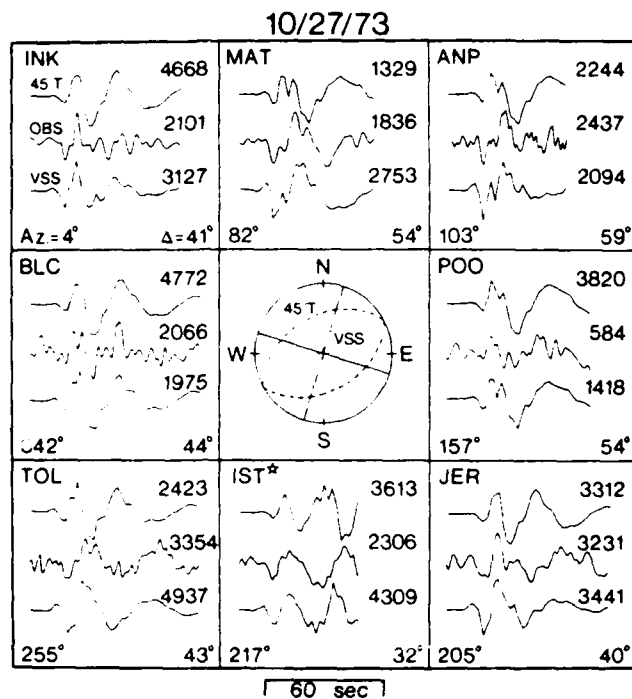


FIG. 11. Radial SV observations for 27 October 1973 compared with the WKB spectral synthetic waveforms for the 45° thrust and vertical strike-slip solutions combined with the explosion source. *P*-wave radiation nodes for the two solutions are shown in the lower hemisphere projection. The source-receiver structures follow the notation of Figure 12. Numbers shown are the observed and synthetic peak-to-peak amplitudes in millimicrons.

seismograms. Given the complexities intrinsic to the SV waveform for both double-couple sources and the explosion, it is remarkable how well the synthetic seismograms resemble the data. The quality of the matches, and the uniqueness and preference of the strike-slip solution over a considerable azimuthal range, permit the elimination of the thrust orientation of tectonic release for the two explosions considered. Thus, careful forward modeling of SV wave propagation can resolve the appropriate tectonic release double-couple in situations where other phases and ray theory modeling fail to yield a unique solution.

A large suite of synthetic SV seismograms are compared with observed waveforms in Figures 12 and 13, for the 27 October 1973 and 2 November 1974 events, respectively. The synthetics are constructed using the aforementioned input parameters and the strike-slip solution. The receiver structure is indicated by a star if different from EU2. The traces have not been filtered; hence, the observed (top) seismograms contain slightly more high-frequency energy than the 2.0-sec sampled synthetic (bottom) traces. Nonetheless, the two signals match remarkably well.

Gradations in relative source contribution and changing polarity cause the waveforms to vary considerably over azimuth. Most of the existing misfit is readily attributable to structural effects; misrepresentation of the actual receiver structure by the idealized models. In some cases, the first-order differences can be diminished by appealing to either TNA or SNA for the receiver structure. This is only necessary for the few anomalous stations indicated. The effects of

10/27/73

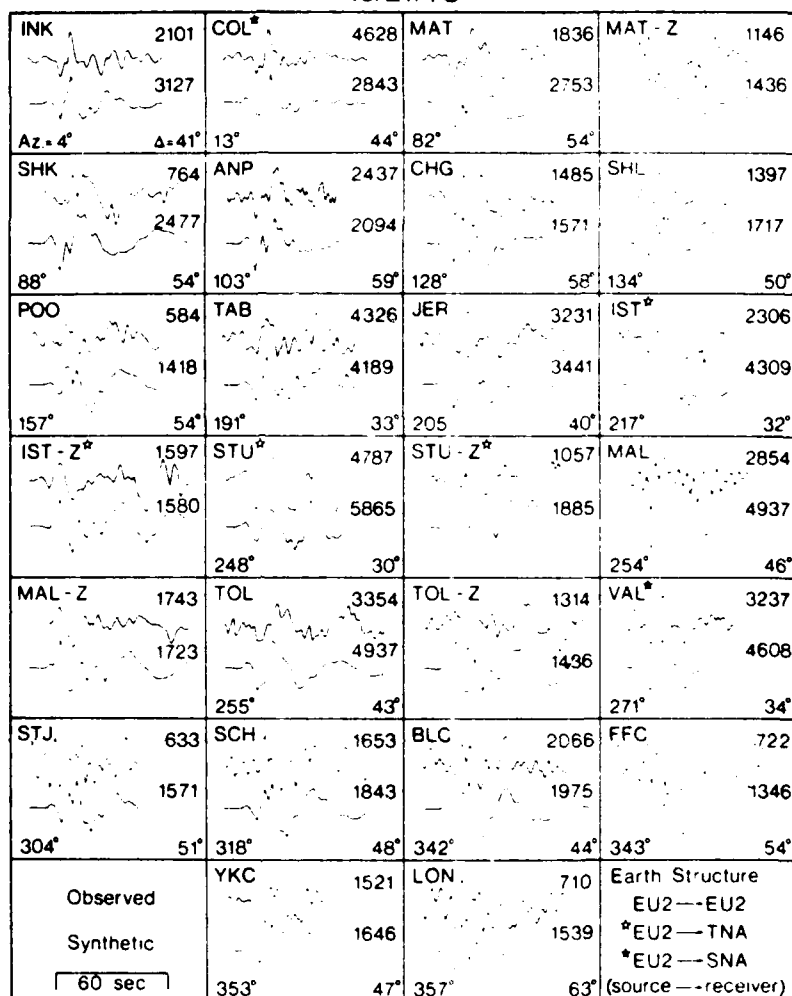


FIG. 12. Observed SV seismograms for 27 October 1973 compared with WKB spectral synthetics using the strike-slip tectonic release solution. Stations are displayed in order of increasing azimuth. Numbers shown are the observed and synthetic peak-to-peak amplitudes in millimicrons. Source-receiver structures are indicated in the key.

each receiver structure for the EU2 source model has been previously addressed and shown in Figure 10. We have not attempted the difficult task of perturbing the earth models to improve the matches. The good quality of the synthetic-observed fits suggests that if receiver structures are well-known for a number of stations, it may be possible to modify the EU2 source model to better understand the seismic structure underlying Novaya Zemlya. An additional source of waveform mismatch arises from the modeling assumption of horizontal velocity discontinuities. Dipping layers, notably a dipping Moho, may alter the dominant period and amplitude of the S_p and SPL phases. The behavior of SPL at MAT, IST, and TOL is likely due to receiver complexities not accounted for in the plane-layered earth models. Hence, the choice of receiver model is not intended to directly reveal the actual receiver velocity structure. Rather, it provides a mod-

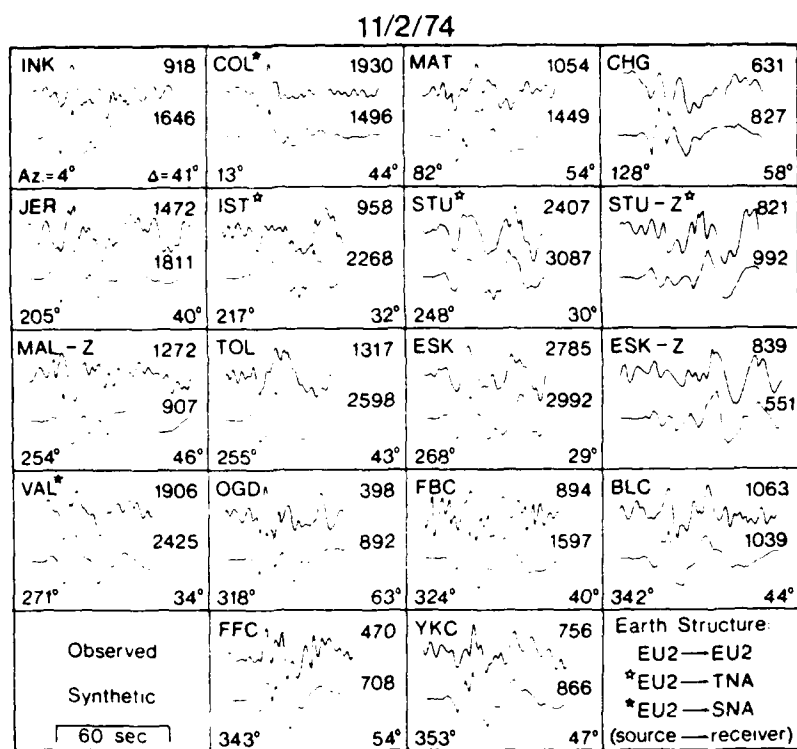


FIG. 13. Same as Figure 12, but for the 2 November 1974 event.

eling flexibility that accounts to first-order for lateral heterogeneity, variable low-velocity zones, and other indeterminate structural complexities.

The peak-to-peak amplitudes in μ for the initial S arrivals are shown in Figures 12 and 13. For most stations, the amplitudes agree within a factor of 2. This is to be expected, given that the observed amplitude pattern was initially used to constrain the relative source contributions. The success of this application of the WKB spectral method encourages application of this procedure to related problems, chiefly because it has involved the calculation, relative weighting, and combination of two very complex Green's functions.

F FACTORS

The F factor was introduced by Toksöz *et al.* (1965) as a means of characterizing the ratio of nonisotropic to isotropic energy,

$$F = 1.5(M_0^{dc}/M_0^{exp})$$

where the moment of the double-couple may be determined by SH modeling and the explosion moment by,

$$M_0^{exp} = 4\pi\rho\alpha^2\psi_x$$

(Aki *et al.*, 1974). The determination of M_0^{exp} depends primarily on the seismic velocity and attenuation structure assumed in the modeling. The poor resolution

of these parameters introduces a baseline uncertainty for the absolute M_0 values. Although the moments are not well constrained, the ratio of energy contributions should remain nearly constant, regardless of the earth model used.

For the assumed source values of α (6.08 km/sec) and ρ (2.74 gm cm³), the double-couple moment is 3.2×10^{24} dyne-cm for the 27 October 1973 event and 1.7×10^{24} dyne-cm for the 2 November 1974 event. The ψ_x determined from strike-slip SV half-space modeling (3.2×10^{11} cm³) translates to $M_0^{exp} = 4.2 \times 10^{24}$ dyne-cm, and $F = 1.2$ for 27 October 1973. The M_0^{exp} and M_0^{dc} for 2 November 1974 are both 1.9 times smaller than the 27 October 1973 values, producing the same F factor. Using the more complete WKBJ spectral results ($\psi_x = 3.8 \times 10^{11}$ cm³ for 27 October 1973 and $\psi_x = 2.0 \times 10^{11}$ cm³ for 2 November 1974), $F = 1.0$ for 27 October 1973 and 2 November 1974. These F factors are within a factor of 2 of the results found by Burger *et al.* (1986b) using a combination of long-period P -wave and S -wave modeling. Given the inherent uncertainties that limit resolution of the F factor, it is not possible to argue a preference for either set of results. However, in both studies, the F factor is relatively small. Consequently, yields based on azimuthally distributed M_S measurements for these events (Sykes and Wiggins, 1986) should not be significantly biased by tectonic release contamination.

DISCUSSION

An unconstrained deviatoric component accompanying explosion signals can potentially alter yield estimates derived from surface waves, pS amplitudes, or P waves. Rayleigh and Love wave excitation by explosive sources has been investigated by numerous authors, but it is not possible to uniquely determine the tectonic release mechanism from fundamental modes alone (Aki and Tsai, 1972; Toksöz and Kehrner, 1972; Given and Mellman, 1986). Patton (1988) included higher mode surface waves to resolve the deviatoric moment tensor, but this method requires knowledge of the source spall characteristics. SV amplitudes have been successfully used in this study and others (Lay *et al.*, 1984b) to determine explosion source strength when tectonic release is either of known orientation or very small. Helmberger (1985) used pS amplitudes at nodal tectonic release stations to obtain accurate yield estimates for NTS events. Wallace *et al.* (1983) identified a strong sP signature in long-period P waves that indicates a high-frequency component of tectonic release radiation. Additionally, Lay *et al.* (1984a) examined short-period P waves and concluded that it is possible that tectonic release can affect teleseismic short-period amplitudes. Assessment of explosion source strength using any of these phases requires the determination of tectonic release moment and focal mechanism.

Application of the WKBJ spectral method has been shown to be an effective tool for discerning the appropriate tectonic release mechanism. Just as important, however, are the implications for further discrimination of source velocity structure and attenuation along the source-receiver path. As previously mentioned, the EU2 source model could possibly be perturbed to produce uniform improvements of the observed-synthetic fits. This endeavor would require detailed information on receiver structures for a suite of stations with little noise contamination, which may be possible using the data set from these two large Novaya Zemlya events. In addition to further understanding of source velocity structure, an appropriate attenuation model could perhaps be better resolved with systematic WKBJ spectral modeling. A frequency-dependent Q model (EURS) was re-

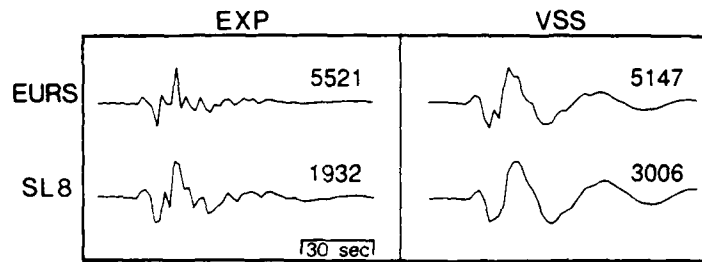


FIG. 14. Radial SV WKB spectral synthetics comparing EURS with the modified SL8 attenuation structure for the explosion and strike-slip sources in an EU2 earth. Numbers are peak-to-peak amplitudes in millimicrons at 50° distance and strike, $\phi = 332^\circ$.

cently proposed by Der *et al.* (1986) using a large data set of teleseismic body waves for Eurasian shield areas. As shown in Figure 7, the EURS model has significantly higher Q values in comparison to the modified SL8 Q structure used previously. As a result, using model EURS produces synthetic waveforms containing more high-frequency information and higher amplitudes for the same relative source strengths. Synthetic seismograms for explosion and vertical strike-slip sources are presented in Figure 14 for an EU2 earth with the EURS Q structure at 0.03 Hz. Although absolute amplitudes will still be ambiguous, the frequency content of synthetic waveforms for a given Q structure could be used to identify a Q model for Novaya Zemlya that is more appropriate than the modified SL8 version we used. Furthermore, exploration of these additional parameters would likely yield improved matches with some of the observed signals, particularly if the Green's functions are sampled at shorter time intervals than used in this study.

CONCLUSIONS

We have demonstrated that quantitative modeling of complete teleseismic SV waveforms for explosions with tectonic release is viable and can provide greater resolution of the double-couple orientation than modeling of SH data alone. Assuming that the nonisotropic source is coincident in space and time with the explosion source, WKB spectral synthetic SV seismograms have been constructed, including Sp , diffracted Sp , and SPL contributions. We apply this procedure to SV signals from large underground explosions for which SH modeling indicates that the tectonic release orientation is either vertical strike-slip or 45° -dipping thrust. Comparison of synthetic and observed SV waveforms for two Southern Novaya Zemlya events strongly suggests that a vertical strike-slip mechanism is appropriate for the 27 October 1973 and 2 November 1974 Southern Novaya Zemlya events. In general, the resolution of true tectonic release orientation has important ramifications for estimates of explosion yield using surface waves (M_S), P waves (m_b), or pS amplitudes. Thus, this modeling approach may be useful for other events for which we lack a well-constrained tectonic release mechanism. The success of this first-order modeling effort also suggests that additional understanding of source velocity and attenuation structure is possible with systematic WKB spectral modeling.

ACKNOWLEDGMENTS

We thank C. A. Langston for providing the spectral synthetic code along with extensive documentation and L. N. Frazer, S. P. Grand, and C. S. Lynnes, and C. J. Young for their helpful comments.

on the manuscript. This research was partially supported by the Advanced Research Projects Agency of the Department of Defense and was monitored by the Air Force Geophysics Laboratory under Contract F19628-87-K-0010. Acknowledgment is also made to the Donors of the Petroleum Research Fund, administered by the American Chemical Society, for the partial support of this research.

REFERENCES

- Aki, K. and Y.-B. Tsai (1972). Mechanism of Love-wave excitation by explosive sources, *J. Geophys. Res.* **77**, 1452-1475.
- Aki, K., P. Reasenberg, T. DeFazio, and Y.-B. Tsai (1969). Near-field and far-field seismic evidences for triggering of an earthquake by the BENHAM explosion, *Bull. Seism. Soc. Am.* **59**, 2197-2207.
- Anderson, D. L. and R. S. Hart (1978). Q of the earth, *J. Geophys. Res.* **83**, 5869-5882.
- Archambeau, C. B. (1972). The theory of stress wave radiation from explosions in prestressed media, *Geophys. J. R. Astr. Soc.* **29**, 329-366.
- Archambeau, C. B. and C. Sammis (1970). Seismic radiation from explosions in prestressed media and the measurement of tectonic stress in the earth, *Rev. Geophys. Space Phys.* **8**, 473-499.
- Baag, C.-E. and C. A. Langston (1985a). Shear-coupled PL, *Geophys. J. R. Astr. Soc.* **80**, 363-385.
- Baag, C.-E. and C. A. Langston (1985b). A WKB spectral method for computation of SV synthetic seismograms in a cylindrically symmetric medium, *Geophys. J. R. Astr. Soc.* **80**, 387-417.
- Baag, C. E. and C. A. Langston (1986). Diffracted Sp generated under the Australian shield, *J. Geophys. Res.* **91**, 9507-9516.
- Brune, J. N. and P. W. Pomeroy (1963). Surface wave radiation patterns for underground nuclear explosions and small-magnitude earthquakes, *J. Geophys. Res.* **68**, 5005-5028.
- Burdick, L. J. and C. A. Langston (1977). Modeling crustal structure through the use of converted phases in teleseismic body waveforms, *Bull. Seism. Soc. Am.* **67**, 677-691.
- Burger, R. W., T. Lay, and L. J. Burdick (1986a). Estimating the relative yields of Novaya Zemlya tests by waveform intercorrelation, *Geophys. J. R. Astr. Soc.* **87**, 775-800.
- Burger, R. W., T. Lay, T. C. Wallace, and L. J. Burdick (1986b). Evidence of tectonic release in long-period S waves from underground nuclear explosions at the Novaya Zemlya test sites, *Bull. Seism. Soc. Am.* **76**, 733-755.
- Chapman, C. H. (1973). The earth flattening transformation in body wave theory, *Geophys. J. R. Astr. Soc.* **35**, 55-70.
- Dahlman, O. and H. Israelson (1977). *Monitoring Underground Nuclear Explosions*, Elsevier, New York, 440 pp.
- Der, Z. A., A. C. Lees, and V. F. Cormier (1986). Frequency dependence of Q in the mantle underlying the shield areas of Eurasia. Part III. The Q model, *Geophys. J. R. Astr. Soc.* **87**, 1103-1112.
- England, P. C., M. H. Worthington, and D. W. King (1977). Lateral variation in the structure of the upper mantle beneath Eurasia, *Geophys. J. R. Astr. Soc.* **48**, 71-79.
- Frazer, L. N. (1977). Synthesis of shear coupled PL, *Ph.D. Thesis*, Princeton University, Princeton, New Jersey.
- Given, J. W. and G. R. Mellman (1985). Source parameters of Shagan River East Kazakh, USSR events using surface wave observations, in *The VELA Program. A Twenty-Five Year Review of Basic Research*, DARPA, Arlington, Virginia, 705-710.
- Given, J. W. and G. R. Mellman (1986). Estimating explosion and tectonic release source parameters of underground nuclear explosions from Rayleigh and Love wave observations, Final Report—Part I, SGI-R-86-126, Sierra Geophysics, Kirkland, Washington.
- Grand, S. P. and D. V. Helmberger (1984). Upper mantle shear structure of North America, *Geophys. J. R. Astr. Soc.* **76**, 399-438.
- Helmberger, D. V. (1985). Long-period S waves and yield estimation, Papers presented at the 7th Annual DARPA/AFGL Seismic Research Symposium Colorado Springs, Colorado.
- Helmberger, D. V. and D. M. Hadley (1981). Seismic source functions and attenuation from local and teleseismic observations of the NTS events JORUM and HANDLEY, *Bull. Seism. Soc. Am.* **71**, 51-67.
- Hirasawa, T. (1971). Radiation patterns of S waves from underground nuclear explosions, *J. Geophys. Res.* **76**, 6440-6454.
- Jordan, T. H. and L. N. Frazer (1975). Crustal and upper mantle from Sp phases, *J. Geophys. Res.* **80**, 1504-1518.
- Kind, R. (1978). The reflectivity method for a buried source, *J. Geophys.* **44**, 603-612.

- Lambert, D. G., E. A. Flinn, and C. B. Archambeau (1972). A comparative study of the elastic wave radiation from earthquakes and underground explosions, *Geophys. J. R. Astr. Soc.* **29**, 403–432.
- Langston, C. A. and C.-E. Baag (1985). The validity of ray theory approximations for the computation of teleseismic SV waves, *Bull. Seism. Soc. Am.* **75**, 1719–1727.
- Langston, C. A. and D. V. Helmberger (1975). A procedure for modelling shallow dislocation sources, *Geophys. J. R. Astr. Soc.* **42**, 117–130.
- Lay, T., T. C. Wallace, and D. V. Helmberger (1984a). The effects of tectonic release on short-period P waves from NTS explosions, *Bull. Seism. Soc. Am.* **74**, 819–842.
- Lay, T., D. V. Helmberger, and D. G. Harkrider (1984b). Source models and yield-scaling relations for underground nuclear explosions at Amchitka Island, *Bull. Seism. Soc. Am.* **74**, 843–862.
- Lerner-Lam, A. L. and T. H. Jordan (1987). How thick are the continents?, *J. Geophys. Res.* **92**, 14007–14026.
- Müller, G. (1977). Earth-flattening approximation for body waves derived from geometric ray theory—Improvement, corrections, and range of applicability, *J. Geophys.* **42**, 429–436.
- Oliver, J. (1961). On the long period character of shear waves, *Bull. Seism. Soc. Am.* **51**, 1–12.
- Patton, H. J. (1988). Source models of the Harzer explosion from regional observations of fundamental-mode and higher mode surface waves, *Bull. Seism. Soc. Am.* **78**, 1133–1157.
- Press, F. and C. B. Archambeau (1962). Release of tectonic strain by underground nuclear explosions, *J. Geophys. Res.* **67**, 337–343.
- Rial, J. A., S. Grand, and D. V. Helmberger (1984). A note on lateral variation in upper mantle shear-wave velocity across the Alpine front, *Geophys. J. R. Astr. Soc.* **77**, 639–654.
- Sykes, L. R. and G. C. Wiggins (1986). Yields of Soviet underground nuclear explosions at Novaya Zemlya, 1964–1976, from seismic body and surface waves, *Proc. Natl. Acad. Sci. U.S.A.* **83**, 201–205.
- Toksoz, M. N. and H. H. Kehrner (1972). Tectonic strain release by underground nuclear explosions and its effect on seismic discrimination, *Geophys. J. R. Astr. Soc.* **31**, 141–161.
- Toksoz, M. N., D. G. Harkrider, and A. Ben-Menahem (1965). Determination of source parameters by amplitude equalization of seismic surface waves. Part 2. Release of tectonic strain by underground nuclear explosions and mechanisms of earthquakes, *J. Geophys. Res.* **70**, 907–922.
- Wallace, T. C., D. V. Helmberger, and G. R. Engen (1983). Evidence of tectonic release from underground nuclear explosions in long-period P waves, *Bull. Seism. Soc. Am.* **73**, 593–613.
- Wallace, T. C., D. V. Helmberger, and G. R. Engen (1985). Evidence of tectonic release from underground nuclear explosions in long-period S waves, *Bull. Seism. Soc. Am.* **75**, 157–174.
- Watson, T. H. (1970). Fast computation of Rayleigh wave dispersion in a layered half-space, *Bull. Seism. Soc. Am.* **60**, 161–166.

DEPARTMENT OF GEOLOGICAL SCIENCES
UNIVERSITY OF MICHIGAN
ANN ARBOR, MICHIGAN 48109

Manuscript received 23 November 1987

Section 2

Observations of Teleseismic P Wave Coda For Underground Explosions

Observations of Teleseismic *P* Wave Coda for Underground Explosions

CHRISTOPHER S. LYNNE¹ and THORNE LAY¹

Abstract—The early *P* wave coda (5–15 sec after the first arrival) of underground explosions at the Nevada Test Site is studied in the time domain using 2082 teleseismic short-period recordings, with the intent of identifying near-source contributions to the signals in the frequency range 0.2–2.0 Hz. Smaller magnitude events tend to have relatively high coda levels in the 0.4–0.8 Hz frequency band for both Yucca Flat and Pahute Mesa explosions. Coda complexity in this low-frequency passband is negatively correlated with burial depth for Pahute Mesa events but is only weakly correlated with depth for Yucca Flat events. Enhanced excitation of relatively long-period scattered waves for smaller, less deeply buried events is required to explain this behavior. Coda complexity in the 0.8–1.1 Hz band is positively correlated with magnitude and depth for Pahute Mesa events, but has no such dependence for Yucca Flat events. This may result from systematic variations between the spectra of direct signals and coda arrivals caused by *pP* interference for the largest events, all of which were detonated at Pahute Mesa. Another possible explanation is a frequency-dependent propagation effect on the direct signals of the larger events, most of which were located in the center of the mesa overlying strong lateral velocity gradients in the crust and upper mantle. Event average complexity varies spatially for both test sites, particularly in the 0.8–1.1 Hz band, providing evidence for frequency-dependent focussing or scattering by near-source structure. Both the direct arrivals and the early coda have strong azimuthal amplitude patterns that are produced by defocussing by mantle heterogeneity. The direct arrivals have stronger coherent azimuthal patterns than the early coda for Pahute Mesa events, indicating more pronounced deep crustal and shallow mantle defocussing for the direct signals. However, for Yucca Flat events the direct arrivals have less coherent azimuthal patterns than the coda, suggesting that a highly variable component of near-source scattering preferentially affecting the downgoing energy is superimposed on a pattern produced by mantle heterogeneity that affects the entire signal. This complicated behavior of the direct arrivals may be the result of triplications and caustics produced by the complex basement structure known to underlie the Yucca Flat test site. The presence of strong azimuthal patterns in the early coda indicates that source strength estimates based on early coda are subject to biases similar to those affecting estimates based on direct arrivals.

Key words: Scattering, coda, underground explosions, yield estimation, wave propagation.

Introduction

Reliable determination of the energy released by seismic sources is a fundamental problem in earthquake and explosion seismology. For relatively small energy sources, it is necessary to utilize short-period seismic waves to determine the source strengths,

¹ Department of Geological Sciences, University of Michigan, Ann Arbor, MI 48109, U.S.A.

although it is well-known that the scale lengths of heterogeneity within the earth are such that propagational effects are particularly pronounced for the short-period waves of interest. Thus, there has been a concentrated effort to achieve a better theoretical and empirical understanding of short-period wave propagation processes in the earth. The primary objective in the field of explosion seismology is to develop a procedure for seismic yield estimation using short-period waves that is both precise (i.e., consistent) and accurate.

The currently preferred methods of yield estimation employ seismic magnitude measurements, which can be divided into two classes: those that rely on a direct phase, such as m_b^{ab} , (based on the first cycle of the short-period P waveform); and those that are based on a scattered phase, such as Lg or P coda. The advantage of direct phases is that they can be treated to a large degree as deterministic signals, which are generally expected to be rather simple for underground explosions. This allows quantitative application of corrections for predictable biases arising from source function scaling, free-surface interaction, attenuation variations and propagation effects due to known large-scale three-dimensional structure (LAY *et al.*, 1984; LAY, 1985; CORMIER, 1987). However, the earth is heterogeneous to such a degree that there appears to be a limit to the precision that can be obtained in yield estimation using direct phases (BACHE, 1982). On the other hand, scattered phases must usually be treated stochastically, but they do have the attribute that the scattered arrivals sample many raypaths, presumably averaging out to a large extent the various heterogeneities sampled (AKI, 1982; CORMIER, 1987). Several authors have examined the relative performance of magnitudes based on teleseismic P coda and direct P as relative size estimators, concluding that P coda generally yields more precise size estimates (BULLITT and CORMIER, 1984; BAUMGARDT, 1985; GUPTA *et al.*, 1985; LAY and WELC, 1987).

In addition, approximately half of the energy in teleseismic P coda from shallow sources appears to result from near-source scattering (DAINTY, 1985). Thus, the P coda may provide information about the source region, either through use as a reference for examining direct signal behavior (GUPTA and BLANDFORD, 1987), or by analysis of the coda itself (LAY and WELC, 1987; LAY, 1987a,b). While some empirical progress has been made in using P coda for both size estimates and determining source properties, the exact origins of P coda remain somewhat enigmatic. It presumably is generated by scattering from small-scale heterogeneities and may therefore be useful for characterizing crust and mantle velocity variations. However, the relative importance of processes such as mode conversions, forward scattering or back scattering is not well established. Improving our knowledge of the processes involved in the generation of P coda is essential to a basic understanding of short-period wave propagation in the earth.

In this paper, we will examine the properties of the early P coda (defined here as the first 5–15 sec after the first arrival of the P wave) from underground explosions at the Nevada Test Site. The early coda is particularly interesting since there is some

possibility of treating it deterministically as well as statistically, because the near-source contributions must be generated within a restricted volume around the source. Deterministic treatments that attempt to explain particular arrivals in the coda are presented by BOUCHER (1973), who analyzed the first 3 sec of near-source recordings, and by LAY (1987b) who inverted for isotropic scatterers using the first 15 sec of the *P* wavetrain. However, inversions of the latter type are still very difficult and poorly posed due to our lack of knowledge of the predominant scattering mechanisms producing the coda; accordingly, in this study, we will examine the statistical properties of the early *P* coda empirically, to motivate and help design future inversions for scatterers. These properties will also provide an observational basis for evaluating the size estimation capabilities of the early coda.

The statistical properties of early *P* coda have already been extensively studied for explosions at the Pahute Mesa test site, as well as for the two Novaya Zemlya test sites and the Amchitka test site by LAY and WELC (1987) and LAY (1987a). One of the interesting results obtained in these data-intensive studies was the detection of a negative correlation of coda "complexity" (power in the coda relative to the direct arrival) with both magnitude and depth of burial in the 0.4–0.8 Hz frequency band for all sites studied. Similar correlations were noted for Novaya Zemlya and Amchitka for the 0.8–1.1 Hz, 1.1–1.5 Hz and 0.2–2.0 Hz bands, while Pahute Mesa explosions exhibit a positive correlation of complexity with magnitude/depth in the 0.8–1.1 Hz band. Spatial correlations of coda complexity were also noted for the Pahute Mesa test site, with complexity increasing toward the center of the test site. No correlation with tectonic release *F*-factor was found; thus, it appears that aftershocks do not contribute significant high frequency energy to the coda, as had been suggested by DOUGLAS (1984) on the basis of analysis of the Pahute Mesa explosion GREELEY.

Another interesting result from the study of Pahute Mesa coda was the detection of systematic azimuthal patterns in the early coda amplitudes that mirror the patterns in the direct arrivals, albeit with a somewhat smaller range of variation. In a detailed analysis of the direct signals, LYNNEs and LAY (1988) demonstrated a correlation between low $m_{\text{sh}}^{\text{ab}}$ and fast travel times for Pahute Mesa explosions, which they attributed to strong focussing/defocussing effects in the lithosphere and in the deep mantle. Thus, it appears that the near-source component of the early coda is affected by the same deep mantle heterogeneity, rather than having effectively averaged out all of the propagational effects. Similar correlations between coda and direct arrival amplitudes have been observed by BULLITT and CORMIER (1984) and BAUMGARDT (1985).

In this study, we have digitized 1063 WWSSN and Canadian Seismic Network seismograms from 32 Yucca Flat explosions to complement the 1019 seismograms from 25 Pahute Mesa tests analyzed by LAY and WELC (1987) and LAY (1987a,b). As in these earlier studies, we identify the near-source contribution to the early *P* coda by using a large, well-distributed station set. The dependence of coda

complexity on various event parameters such as depth and magnitude is determined for the two test sites. We also examine the individual event average complexity values in order to look for coherent spatial variations within the test sites. Such variations provide prime motivations for future attempts to identify particular scattering structures. Finally, the azimuthal patterns of the direct arrivals and coda for the two nearby test sites will be compared to determine the relative importance of near-source and deep mantle effects.

Data Analysis

The seismograms for Yucca Flat events were processed in a nearly identical manner to those for Pahute Mesa events, as described in LAY and WELCH (1987) and LAY (1987a). At least 15 sec of noise and 15 sec of signal were digitized and interpolated at a 0.1 sec sample interval. The seismograms were filtered using three-pole Butterworth bandpass filters with four different passbands: 0.2–2.0 Hz ("broadband"), 0.4–0.8 Hz (low-frequency), 0.8–1.1 Hz (mid-frequency), and 1.1–1.5 Hz (high-frequency). The individual instrument responses were deconvolved from the low-frequency, mid-frequency and high-frequency data sets before filtering; however, deconvolutions of the "broadband" seismograms were unstable at the long period end, so the instrument response was not removed from this data set. Since most of the stations are from the WWSSN, this results only in a slight increase of the variance in the broadband results.

In order to characterize the complexity of the coda, the normalized energy temporal centroid (McLAUGHLIN and ANDERSON, 1985) of the first 15 sec of the squared analytic envelope (Figure 1) was computed. The energy temporal centroid (C_{hp}) is defined for each bandpass filtered (bp) seismogram by:

$$C_{hp} = \frac{\int_0^{15} s^2(t)t \, dt}{\int_0^{15} s^2(t) \, dt},$$

where $s^2(t)$ is the square of the filtered signal envelope. Larger centroid values indicate a higher proportion of energy later in the signal. A correction for noise level was applied by subtracting the root-mean-square (RMS) of the noise window from the envelope before computing C_{hp} ; this generally reduced all the event average centroids by comparable amounts. Station/path corrections were determined by averaging the centroids for all events from a given test site recorded at a given station. When computing an event average value of C_{hp} , the station corrections were applied, and the corrected centroids were azimuthally averaged in 7.5° windows to reduce bias from uneven azimuthal distribution. The event centroids for each test site were then demeaned, so that the values reported below are deviations from the average.

The RMS of the direct arrival (0–5 sec) and the coda (5–15 sec) were also computed for each seismogram. The logarithm of the ratio $\text{RMS}^{5-15}/\text{RMS}^{0-5}$ provides

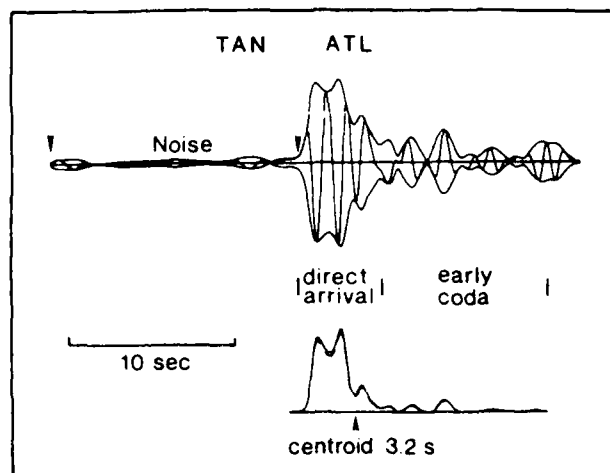


Figure 1

Example of the data analysis procedure. The top trace is the *P* wavetrain with its analytic envelope, filtered from 0.2-2.0 Hz for the Yucca Flat event TAN at station ATL. RMS amplitudes are calculated for the first 5 sec (direct arrival) and the 5-15 sec window (early coda). The bottom trace shows the squared envelope, before the noise correction (solid line) and after the noise correction (dashed line), and the effect of the noise correction on the energy temporal centroid.

another measure of the complexity of the coda, with higher values indicating relatively enhanced coda levels. Event averages for $\log(\text{RMS}^{5-15}/\text{RMS}^{0-5})$ were calculated in the same manner as for the centroids. The $\log(\text{RMS}^{5-15}/\text{RMS}^{0-5})$ measure was used to compare with the behavior of the direct arrival ($\log(\text{RMS}^{0-5})$) and early coda ($\log(\text{RMS}^{5-15})$); however the centroids will be preferred in this study when considering event average complexity, since it proved difficult to apply a stable noise correction to the $\log(\text{RMS}^{5-15}/\text{RMS}^{0-5})$ measurements. The correlation coefficients, r , of the event average centroids (without noise correction) vs. $\log(\text{RMS}^{5-15}/\text{RMS}^{0-5})$ are $r = 0.94$ in the low-frequency band, $r = 0.84$ in the mid-frequency band, and $r = 0.94$ in the high-frequency band for Yucca Flat events. The broadband correlation coefficient is only $r = 0.72$, which may be due to the fact that the seismograms were not deconvolved in this case. In general, however, these two quite different types of coda complexity measures gave very similar results, as was the case for the Pahute Mesa date (LAY and WELC, 1987; LAY, 1987a).

Event Average Complexity

Correlation with mb and depth. The event average centroids in each frequency band for Yucca Flat were correlated with magnitude, burial depth and depth below the water table. However, the only parameter that gave a correlation coefficient above 0.5 in any of the frequency bands was magnitude. The correlations of coda

complexity with magnitude and with burial depth in each frequency band for both Yucca Flat and Pahute Mesa events are listed in Table 1. Variance-weighted linear regressions of coda complexity vs. magnitude and depth for both test sites are shown in Figure 2 for the low-frequency and mid-frequency bands.

Both test sites have little magnitude dependence in the broadband and high-frequency band cases. In the mid-frequency band, however, the Pahute Mesa events show a positive correlation of complexity with magnitude ($r = 0.62$) and depth ($r = 0.71$). There is no correlation with magnitude for Yucca Flat, but a similar trend with burial depth, although several outliers lead to a poor correlation coefficient ($r = 0.27$). These correlations may result from variation of the spectrum of the direct arrival in this band due to pP interference. For larger, more deeply buried events, the increase in pP delay time would shift the spectral scalloping from pP interference toward the middle of the passband. This effect can be predicted by computing synthetic spectra for a large, deep event and a small, shallow event. Two Pahute Mesa explosions were used for these computations (Figure 3), because the teleseismic P waveforms for tests at this site have been extensively studied (LAY, 1985). The spectrum of the coda should not have such pronounced scalloping due to pP (GUPTA and BLANDFORD, 1987) and thus the coda amplitudes in this passband would appear relatively enriched.

In order to demonstrate this with actual data, we compared the spectral amplitudes of a 15 s noise window to two 15 s windows in the P wavetrain, one including the direct arrival (0–12.8 s) and one without the direct arrival (5–17.8 s). This method of presentation (Figure 4) mitigates the possible effects of noise bias between a large and small explosion. COMMODORE is a large, deeply buried Yucca Flat test, while PIRANHA is a relatively small, shallow event, with an average centroid that is 0.7 s less than that of COMMODORE in the mid-frequency band. The spectral null related to pP interference is clearly visible in the 0–12.8 s window, which is dominated by the direct phase, for both events. As in the synthetic case (Figure 3) the null is shifted into the mid-frequency band for the deeper test. This depletes the direct arrival relative to the coda, in which the spectral null is much subdued as seen in the pure coda spectra (5.0–17.8 s). Nevertheless, the null does exert a small effect on the spectral amplitudes, suggesting that the coda has some component of P - P scattering.

Table 1
Correlation coefficients of $C_{\nu p}$ with magnitude and depth of burial

Test Site	Parameter	0.4–0.8 Hz	0.8–1.1 Hz	1.1–1.5 Hz	0.2–2.0 Hz
Yucca Flat	$m_{\nu p}^{ch}$	-0.61	0.06	-0.19	-0.35
Pahute Mesa	$m_{\nu p}^{ch}$	-0.94	0.62	-0.27	-0.34
Yucca Flat	depth	-0.33	0.27	-0.09	-0.06
Pahute Mesa	depth	-0.80	0.71	-0.38	-0.00

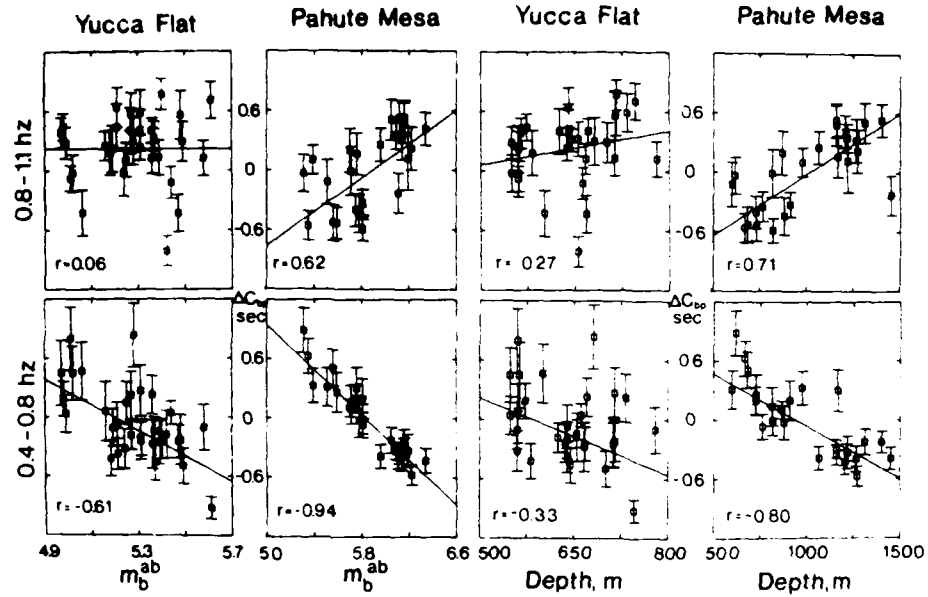


Figure 2

Correlations of relative event average centroids (ΔC_p) with magnitude and burial depth in the low-frequency and mid-frequency bands for Yucca Flat events and Pahute Mesa events.

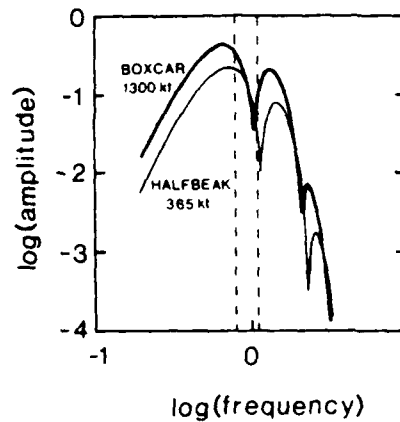


Figure 3

Synthetic amplitude spectra, calculated using $t^* = 0.75$ sec and a short-period WWSSN instrument for a large, deeply buried event (BOXCAR: yield = 1300 kt, depth = 1.158 km) and a smaller, less deeply buried event (HALFBEAK: yield = 365 kt, depth = 0.819 km) at Pahute Mesa. The increase in *pP* delay time for the large event shifts the scalloping effect of *pP* interference into the mid-frequency band.

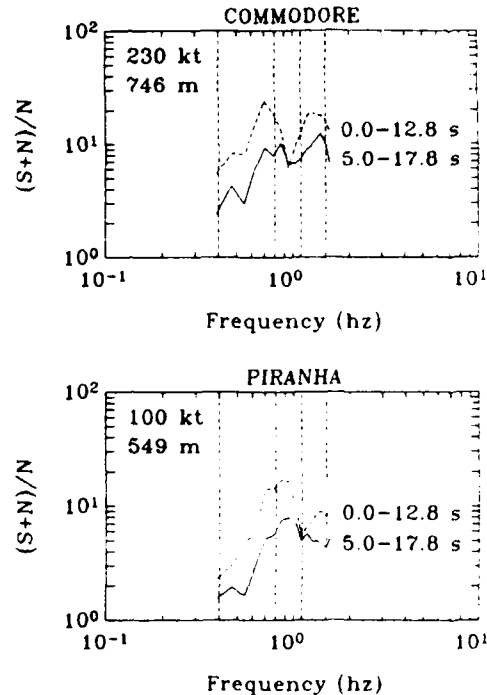


Figure 4

Ratio of seismogram spectral amplitude to noise for a large, deep event (COMMODORE) and a small, shallow event (PIRANHA) at Yucca Flat. The dashed line indicates the 0–12.8 s window, which is dominated by the direct phase, and the 5–17.8 s window, which does not include the direct phase.

Another possibility is frequency dependent defocussing of the direct arrival for events in the center of the mesa, where most of the larger events were located. This second possibility will be tested later by comparing spatial variations of complexity and azimuthal patterns in the different frequency bands.

In the low-frequency band, both test sites show a negative correlation with magnitude ($r = -0.94$ for Pahute Mesa and $r = -0.61$ for Yucca Flat), with smaller magnitude events having relatively high coda levels. For Pahute Mesa, the low-frequency band has a similar dependence on depth of burial ($r = -0.80$). For Yucca Flat events, the dependence of complexity on depth is fairly weak ($r = -0.33$), suggesting that the correlation of complexity with magnitude cannot be ascribed to depth of burial effects alone, but it is important to note that the Pahute Mesa events span a much greater range in burial depth.

One possibility for these correlations is the effect of pP interference. However, the parallel spectral curves in the 0.4–0.8 Hz band for both explosions in Figure 4 indicate that this band is relatively free of such interference. Furthermore, the effect of interference should be to decrease the direct arrivals of the larger explosions, as in the mid-frequency band, which would result in a trend opposite of that which is observed.

Another possibility is that the negative correlation of complexity with size is due to greater noise contamination in this band for smaller explosions. The signal/noise ratio is indeed smaller for PIRANHA than for COMMODORE (Figure 4), but it is still on average fairly high within this band for both tests, dipping below 2 only for the coda of PIRANHA. The effect of noise is further reduced by application of the noise correction to the centroids. Also, although noise will in general increase the centroids, noise that is in phase with the direct arrival decreases the centroids, further mitigating the overall effects of noise. These effects are also reduced by the inclusion of low-noise stations, for which the effects of noise are negligible. Thus, it seems unlikely that noise contamination alone could account for the substantial variation in centroid with magnitude in the low-frequency band.

Spatial variations of complexity. The spatial variation of event average complexity in all four passbands for Yucca Flat is shown in Figure 5. The coherent variations in

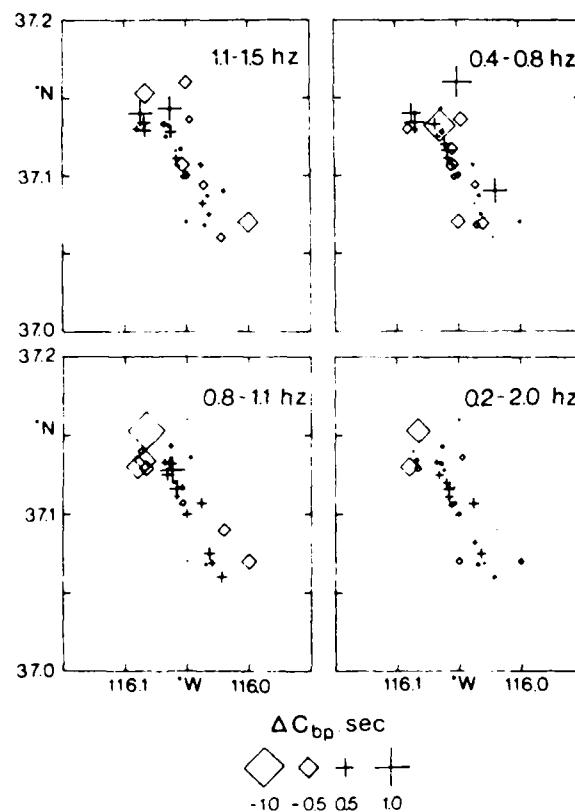


Figure 5

Spatial variation of event average complexity (ΔC_{bp}) for the Yucca Flat test site in the four frequency bands. Diamonds indicate smaller than average coda complexity, and crosses larger than average coda complexity.

complexity with location are quite striking. The least coherent variations occur in the low-frequency band; thus, the complexity in this band appears to be influenced more by magnitude than by the source environment. The most coherent variations occur in the mid-frequency band. This result is consistent with the frequency dependence of spatial variations for Pahute Mesa, where the mid-frequency band had the highest correlation with distance from the center of the mesa ($r = -0.72$ vs. $r = 0.24$ for the low-frequency band and $r = -0.16$ for the high-frequency band). The actual spatial patterns are also somewhat different among the different frequency bands: events in the northwest part of the test array have very low complexity in the mid-frequency band, but relatively high complexity in the high-frequency band; events in the north-central part, on the other hand, have high complexity in the mid-frequency band, but average complexity in the high-frequency band. The broadband map resembles a subdued version of the mid-frequency band map, due to the predominance of mid-frequency band energy in the undeconvolved broadband signals and the compensating trends in the different frequency bands. The difference in patterns among frequency bands suggests a frequency dependence in focussing of the direct arrival or in scattering contributions to the coda.

The spatial variations of coda complexity imply a correlation with some property of the source region. FERGUSON'S (1982) model for Yucca Flat basin, based on

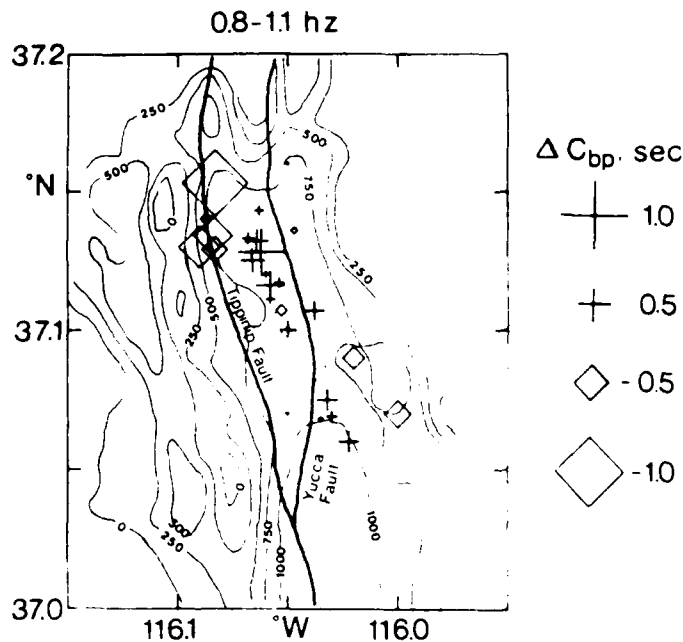


Figure 6
Depth in meters to Tertiary-Paleozoic contact (from FERGUSON, 1982), with event average complexity for the mid-frequency band.

borehole data and gravity modeling, is shown in Figure 6 with the event average complexity values for the mid-frequency band superimposed. The contours indicate the depth to the Tertiary-Paleozoic contact. The events with the highest complexity lie above the basin axis at the north end, just to the west of the Yucca Fault. The events with the simplest coda levels are situated above the east flank of a horst in the basement. This suggests that either the basin shape or the thickness of Tertiary tuffs controls coda complexity in this passband.

Azimuthal Patterns of Amplitudes and Complexity

Slowly varying azimuthal patterns of m_h^{ab} and travel time residuals have been observed for events at both the Pahute Mesa and Yucca Flat test sites (LYNNES and LAY, 1988). Correlations between the travel time and amplitude variations indicate that a significant component is due to focussing and defocussing by velocity heterogeneities in the mantle. MINSTER *et al.* (1981) and TAYLOR (1983) found localized high velocity regions in the upper mantle to the northeast of Pahute Mesa, which can produce defocussing that accounts for much of the difference between the Pahute Mesa and Yucca Flat amplitude patterns (LYNNES and LAY, 1988; CORMIER, 1987). However, the patterns for the two test sites share a large common component, which LYNNES and LAY (1988) inferred to be due to defocussing and focussing by deep (> 200 km) heterogeneity. It is thus of interest to determine the relative influence of such heterogeneities on the direct arrival and the early coda.

In order to determine the average azimuthal patterns for the direct arrivals ($\log(\text{RMS}^{0-5})$), early coda ($\log(\text{RMS}^{5-15})$) and complexity ($\log(\text{RMS}^{5-15}/\text{RMS}^{0-5})$), the station averages for each site were calculated using a least-squares technique that inverts for the best relative source sizes to simultaneously minimize the variance about the station means (Larry Ruff, personal communication). In order to bring out the slowly varying component of the azimuthal patterns, curves of the form $A \cdot \sin[2(\theta - \theta_0)]$ were regressed through the resultant station averages as a function of azimuth (θ). The particular form of the regression curve is not physically motivated, but is intended to parameterize the long-wavelength variations to facilitate comparisons between events and test sites. The *F*-ratio is also calculated as described in LAY *et al.* (1984) to provide an indicator of the coherence and significance of the long-wavelength component. The results for the broadband set are shown for Pahute Mesa and Yucca Flat in Figure 7.

The direct arrivals ($\log(\text{RMS}^{0-5})$) show azimuthal patterns for both Pahute Mesa and Yucca Flat, with a somewhat stronger and more coherent pattern for Pahute Mesa. The correlation in the $\log(\text{RMS}^{0-5})$ station averages between the test sites is $r = 0.83$, while it is $r = 0.73$ for the $\log(\text{RMS}^{5-15})$ values. Thus, a significant component of the variation is common to the two test sites. LYNNES and LAY (1988) obtained a similar result for m_h^{ab} and interpreted the higher amplitude of variation for Pahute Mesa as a result of focussing and defocussing by lateral velocity gradients in

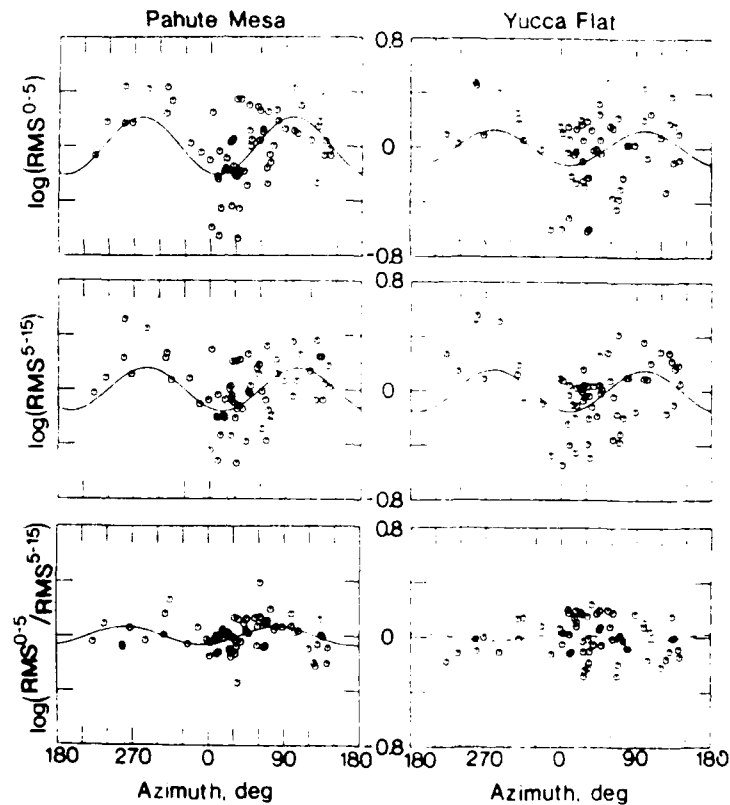


Figure 7

Sin 2θ regressions for Yucca Flat and Pahute Mesa station averaged $\log(\text{RMS}^{0.5})$, $\log(\text{RMS}^{5-15})$ and $\log(\text{RMS}^{0.5}/\text{RMS}^{5-15})$ in the 0.2-2.0 Hz passband. The sine curves are dashed where not statistically significant at the 95% level.

the crust and shallow mantle under the mesa. The $\log(\text{RMS}^{0.5})$ pattern for Pahute Mesa is stronger than the $\log(\text{RMS}^{5-15})$ pattern for the same site, indicating that the focussing/defocussing in the Pahute Mesa direct signals is less pronounced for the early coda due to the averaging characteristics of the scattered wavefield. The $\log(\text{RMS}^{5-15})$ pattern for Yucca Flat, however, has a stronger long-wavelength component (F -ratio = 7.6) with a slightly larger range than the pattern for the direct arrivals (F -ratio = 3.9) from that site, although the orientation of the patterns are quite similar. This behavior is present in many sine curve regressions of $\log(\text{RMS}^{0.5})$ and $\log(\text{RMS}^{5-15})$ of the individual events as well. Thus, it seems that both the direct arrivals and the coda are affected, more or less equally, by deep mantle heterogeneity, while the decreased significance of the direct arrival sine curves appears to be due to increased scatter in the associated station averages. This might result from very-near-source or near-receiver heterogeneity. The Yucca Flat events were detonated close to large basement offsets on the Yucca Fault (Figure 6), which may cause triplications and

caustics affecting the direct arrivals and early coda (STEAD and HELMBERGER, 1986). In any case, the homogenization of the early coda seems to have little effect on subduing the predominant amplitude variations induced by earth structure at both sites.

Sine curves were also regressed through the inverse complexity measure $\log(\text{RMS}^{0.5}/\text{RMS}^{5.15})$ for Pahute Mesa and Yucca Flat (Figure 7). As might be expected, the Pahute Mesa sine curve is significant (F -ratio = 5.2), due to the larger range of variations for $\log(\text{RMS}^{0.5})$ than for $(\text{RMS}^{5.15})$. The Yucca Flat pattern, on the other hand, does not have any long-wavelength variation, indicating that the direct arrival and the phases making up the coda are affected similarly by deep mantle structure.

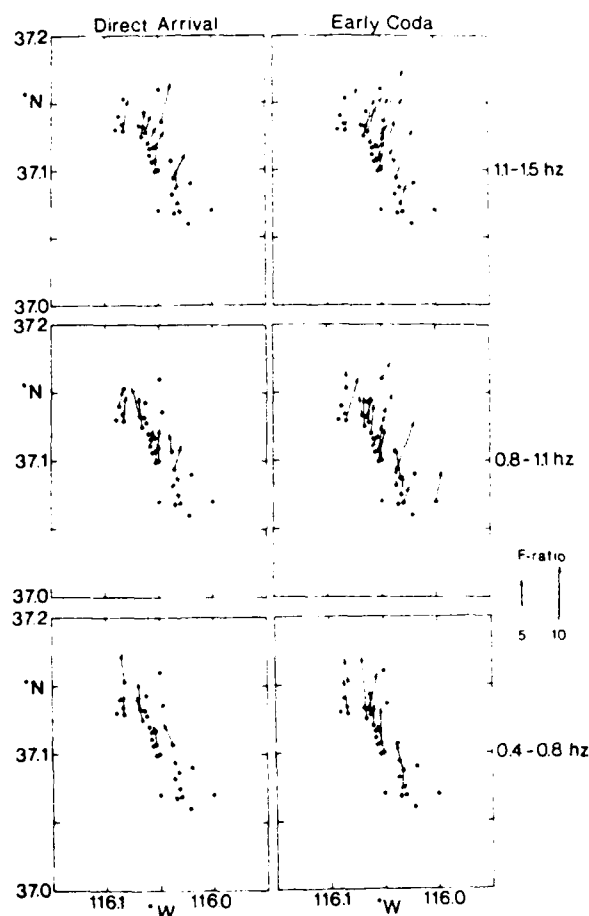


Figure 8

Map of Yucca Flat showing the F -ratios and azimuths of the negative lobes of $\sin 2\theta$ regressions for individual events in the low-frequency, mid-frequency and high-frequency bands. The first column shows results for $\log(\text{RMS}^{0.5})$, the second shows $\log(\text{RMS}^{5.15})$. The length of the arrow is proportional to the F -ratio. Arrows for events with an F -ratio lower than 3 are not shown.

In order to further explore the frequency dependence of the focussing and/or scattering effects, sine curves were regressed through $\log(\text{RMS}^{0-5})$, $\log(\text{RMS}^{5-15})$ and $\log(\text{RMS}^{0-5}/\text{RMS}^{5-15})$ measures of individual events from both test sites in all four frequency bands. The F -ratios and the directions of the negative lobes of the direct arrival and early coda patterns in the low-frequency, mid-frequency and high-frequency bands for Yucca Flat are shown in Figure 8. As with the broadband results, the regressions of $\log(\text{RMS}^{0-5})$ values have systematically smaller F -ratios than the $\log(\text{RMS}^{5-15})$ measurements; however, the amplitudes and azimuths are quite similar for a given frequency band. In addition, there is a systematic clockwise rotation in the long-wavelength patterns with frequency from $2-4^\circ$ (azimuth of the negative lobe) in the low-frequency band to $11-13^\circ$ in the mid-frequency band to $17-20^\circ$ in the high-frequency band.

The F -ratios and azimuths of individual event patterns in the inverse complexity for all four frequency bands are shown in Figure 9 for both test sites. There were too few significant sine curves to deduce any frequency dependence in azimuthal patterns of complexity for Yucca Flat, but a spatial dependence does appear in that those few sine curves that are significant tend to be for events at the southern end of the test

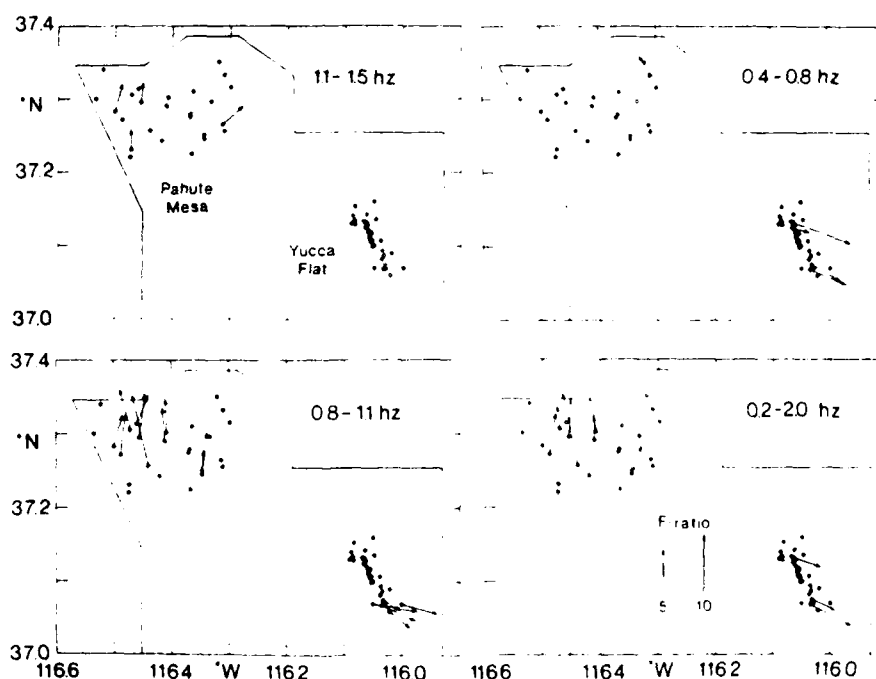


Figure 9

Map of the Nevada Test Site showing the F -ratios and azimuths of the negative lobes of $\sin 2\theta$ regressions through $\log(\text{RMS}^{0-5}/\text{RMS}^{5-15})$ (inverse complexity) for individual events in the broadband, low-frequency, mid-frequency and high-frequency ranges.

array. On the other hand, Pahute Mesa, events clearly exhibit a frequency dependence, as there are more events with coherent patterns in the mid-frequency band than in any other band. Thus, it appears that it is the signal in this passband that produces the significant azimuthal patterns for Pahute Mesa complexity observed by LAY and WELC (1987) for events in the middle of the mesa. Furthermore, almost all of the events with significant patterns in this passband are in the central part of the mesa, supporting the hypothesis that frequency dependence of focussing/defocussing or scattering of the direct arrival plays a role in producing these patterns. Because the large events tend to be located in the center of the mesa, frequency-dependent focussing may also help to explain the positive correlation of complexity with magnitude in the mid-frequency band, rather than simply *pP* variations.

Discussion

One of the most difficult observations to explain from this paper and LAY (1987a) is the dependence of complexity on magnitude. All sites studied so far have exhibited enriched long period (0.4–0.8 Hz) energy in the coda, relative to the direct arrival for smaller events. At Pahute Mesa, this effect could in fact be a dependence on depth of burial. LAY (1987a) suggests that a negative correlation of long period complexity with depth could ensue from increased Rayleigh-to-*P* scattering for the shallower events. However, the depth dependence is slightly weaker than the magnitude dependence at Pahute Mesa, and is quite a bit weaker than the magnitude dependence at Yucca Flat, suggesting that some variable more directly related to source size controls long-period complexity. Such an effect would seem to be intrinsically nonlinear, and as yet there does not seem to be an adequate explanation for this phenomenon. One possibility is that the cavity size influences the excitation of near-field Rayleigh waves, which scatter into the teleseismic wavefield, or that asymmetry exists in the spectrum of energy radiated horizontally relative to that radiated vertically. Numerical simulations are needed to explore these possibilities.

The spatial variations in complexity found for both Pahute Mesa and Yucca Flat strongly suggest that information about the source region structure is contained in the teleseismic *P* wave coda. These variations are slightly dependent on the frequency band, being particularly coherent in the mid-frequency band at both test sites. The spatial dependence of event complexity at Pahute Mesa is difficult to separate from the size dependence since the largest events are located near the center of the mesa. However, the strong azimuthal patterns of complexity and $\log(\text{RMS}^{0.5})$ for events near the center of the mesa suggest that defocussing of the direct arrivals is part of the cause of the enhanced complexity of the coda in the mid-frequency band. The spatial dependence in the mid-frequency band for Yucca Flat is slightly easier to interpret since event complexity in this band is not complicated by depth or magnitude dependence. Clearly, some near-source factor affects complexity. Possible

candidates are the thickness of the Tertiary tuffs, which may give rise to larger Rayleigh waves in the center of the basin (Figure 6), or the basin shape itself, which may defocus the direct arrivals to the north for events in the center of the basin. However, it is difficult to determine what effect these two factors would have without sophisticated finite-difference modeling (e.g., STEAD and HELMBERGER, 1986).

While the event average complexity results point to near-source information in the ratio of the coda to the direct arrival, the azimuthal patterns of the early coda for Yucca Flat emphasize the sizable contribution of a deep mantle effect. The most surprising result is the high significance of the long wavelength component for the coda relative to the direct arrival. This behavior contrasts with that for Pahute Mesa, where the direct arrivals seem to be more strongly defocussed to the north by relatively shallow structure than the coda. The increased scatter in the Yucca Flat direct signals suggests that the direct arrivals from the individual events pass through very shallow structure that has little influence on the scattered phases making up the coda (Figure 10). Thus, the coda comprises arrivals that leave the source region with a

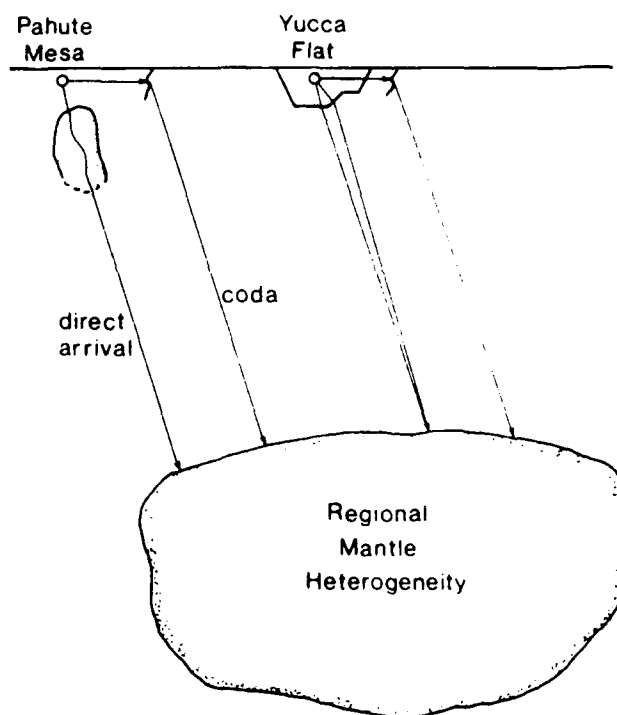


Figure 10

Schematic diagram showing the effects of near-source and deep mantle heterogeneity at the Nevada Test Site. Direct arrivals from Pahute Mesa are defocussed by a high-velocity structure that does not affect the scattered phase. Direct arrivals from Yucca Flat are complicated by triplications and caustics resulting from the basin structure. All of the arrivals are then affected similarly by a deep, regional mantle heterogeneity, which imparts a common azimuthal pattern to direct arrivals and coda from both test sites.

smaller amplitude variability than the direct downgoing energy. Then the entire signal encounters the deep mantle heterogeneity inferred by LYNNEs and LAY (1988), which imparts a common azimuthal pattern. The direct arrivals have the same superimposed variation, but the significance of the long wavelength component is reduced by the additional scatter from very near-source or near-receiver heterogeneity.

The presence of strong azimuthal patterns in the early *P* coda for Yucca Flat events raises the question of whether the early *P* coda is a more precise estimator of source size than the direct arrival for Yucca Flat events. To answer this question, the event standard deviations were averaged for the three measures m_h^{ub} , $\log(\text{RMS}^{0-5})$, and $\log(\text{RMS}^{5-15})$; the average standard deviations are $0.14 \pm .02$ for m_h^{ub} , $0.15 \pm .02$ for $\log(\text{RMS}^{0-5})$, and $0.18 \pm .02$ for $\log(\text{RMS}^{5-15})$. Thus, the early *P* coda actually has somewhat higher variance than the direct arrival for Yucca Flat events. While this difference may be partially due to the increased effect of noise, most of the variance in the early coda would seem to result from the long wavelength component produced by deep mantle heterogeneity.

Although the network-averaged coda measurements from Yucca Flat events are less precise than the m_h measurements, BAUMGARDT (1985) found that the standard deviation of *P* coda across NORSAR for Semipalitinsk events was even less than that of the noise across the array. This suggests that array-averaged coda measurements are more precise than network-averaged *P* or *P* coda. Indeed, azimuthal patterns in the coda such as those from NTS would produce a large degree of scatter in network-averaged measurements, but very little additional scatter at a single array, leading to a comparable or higher precision at the latter.

Even more important than the precision of the different measures, however, is their accuracy. Clearly, measurements of the coda from NTS at a single station or array have a high probability of falling on one of the lobes of the azimuthal pattern from NTS. (NORSAR, for instance, occurs near the minimum of the Pahute Mesa and Yucca Flat azimuthal amplitude patterns.) Consequently, single arrays may record coda magnitudes with very high precision by averaging out the near-receiver effects, but cannot average out effects imparted by mantle heterogeneity near the source region, resulting in an absolute bias.

Conclusions

Data-intensive analysis of teleseismic *P* wave signals has been used to isolate near-source contributions to the early coda from NTS events. The 0.4–0.8 Hz frequency band has a strong negative correlation between coda complexity and magnitude at both the Pahute Mesa and Yucca Flat test sites, with smaller events having higher coda levels. Effects related to depth of burial alone do not seem sufficient to explain this correlation, since the correlation of complexity with depth for Yucca Flat is fairly low.

smaller amplitude variability than the direct downgoing energy. Then the entire signal encounters the deep mantle heterogeneity inferred by LYNNEs and LAY (1988), which imparts a common azimuthal pattern. The direct arrivals have the same superimposed variation, but the significance of the long wavelength component is reduced by the additional scatter from very near-source or near-receiver heterogeneity.

The presence of strong azimuthal patterns in the early *P* coda for Yucca Flat events raises the question of whether the early *P* coda is a more precise estimator of source size than the direct arrival for Yucca Flat events. To answer this question, the event standard deviations were averaged for the three measures m_h^{ub} , $\log(\text{RMS}^{0.5})$, and $\log(\text{RMS}^{1.5})$; the average standard deviations are $0.14 \pm .02$ for m_h^{ub} , $0.15 \pm .02$ for $\log(\text{RMS}^{0.5})$, and $0.18 \pm .02$ for $\log(\text{RMS}^{1.5})$. Thus, the early *P* coda actually has somewhat higher variance than the direct arrival for Yucca Flat events. While this difference may be partially due to the increased effect of noise, most of the variance in the early coda would seem to result from the long wavelength component produced by deep mantle heterogeneity.

Although the network-averaged coda measurements from Yucca Flat events are less precise than the m_h measurements, BAUMGARDT (1985) found that the standard deviation of *P* coda across NORSAR for Semipalitinsk events was even less than that of the noise across the array. This suggests that array-averaged coda measurements are more precise than network-averaged *P* or *P* coda. Indeed, azimuthal patterns in the coda such as those from NTS would produce a large degree of scatter in network-averaged measurements, but very little additional scatter at a single array, leading to a comparable or higher precision at the latter.

Even more important than the precision of the different measures, however, is their accuracy. Clearly, measurements of the coda from NTS at a single station or array have a high probability of falling on one of the lobes of the azimuthal pattern from NTS. (NORSAR, for instance, occurs near the minimum of the Pahute Mesa and Yucca Flat azimuthal amplitude patterns.) Consequently, single arrays may record coda magnitudes with very high precision by averaging out the near-receiver effects, but cannot average out effects imparted by mantle heterogeneity near the source region, resulting in an absolute bias.

Conclusions

Data-intensive analysis of teleseismic *P* wave signals has been used to isolate near-source contributions to the early coda from NTS events. The 0.4–0.8 Hz frequency band has a strong negative correlation between coda complexity and magnitude at both the Pahute Mesa and Yucca Flat test sites, with smaller events having higher coda levels. Effects related to depth of burial alone do not seem sufficient to explain this correlation, since the correlation of complexity with depth for Yucca Flat is fairly low.

- DAINTY, A. M. (1985), *Coda observed at NORSAR and NORESS*. Final Technical Report. AFGL-TR-85-0199. Hanscom AFB, MA. 73 p.
- DOUGLAS, A. (1984), *Teleseismic observations of aftershocks immediately following an underground explosion*, *Geophys. J. Roy. Astr. Soc.* 77, 503-515.
- FERGUSON, J. F. (1982), *Geophysical investigations of Yucca Flat, Nevada*, in *Final Technical Report to the AFOSR*, Contract no. F49620-81-C-0010.
- GUPTA, I. N. and BLANDFORD, R. R. (1987), *A study of *P* waves from NTS explosions—near-source information from teleseismic observations?* *Bull. Seism. Soc. Am.* 77, 1041-1056.
- GUPTA, I. N., BLANDFORD, R. R., WAGNER, R. A., BURNETTI, J. A., and McELFRESH, T. W. (1985), *Use of *P* coda for determination of yield of nuclear explosions*, *Geophys. J. Roy. Astr. Soc.* 83, 541-553.
- LAY, T. (1985), *Estimating explosion yield by analytical waveform comparison*, *Geophys. J. Roy. Astr. Soc.* 82, 1-31.
- LAY, T. (1987a), *Analysis of near-source contributions to early *P* wave coda for underground explosions: 2. Frequency dependence*, *Bull. Seism. Soc. Am.* 77, 1252-1273.
- LAY, T. (1987b), *Analysis of near-source contributions to early *P* wave coda for underground explosions: 3. Inversion for isotropic scatterers*, *Bull. Seism. Soc. Am.* 77, 1767-1783.
- LAY, T., BURDICK, L. J., and HELMBERGER, D. V. (1984), *Estimating the yields of the Amchutka tests by waveform intercorrelation*, *Geophys. J. Roy. Astr. Soc.* 78, 181-208.
- LAY, T. and WELC, J. (1987), *Analysis of near-source contributions to early *P* wave coda for underground explosions: 1. Waveform complexity*, *Bull. Seism. Soc. Am.* 77, 1017-1040.
- LYNNES, C. S. and LAY, T. (1988), *Analysis of amplitude and travel time anomalies for short-period *P* waves from NTS explosions*, *Geophys. J.* 92, 431-443.
- McLAUGHLIN, K. F. and ANDERSON, L. M. (1985), **P* wave dispersion due to scattering and the effects on attenuation and magnitude determination*, in *The Vela Program* (ed. A. U. Kerr) pp. 433-422.
- MINSTER, J. B., SAVINO, J. M., RODI, W. L., JORDAN, T. H. and MASSO, J. F. (1981), *Three-dimensional velocity structure of the crust and upper mantle beneath the Nevada test site*, Final Technical Report SSS R 81-5318, Science, Systems and Software, La Jolla, California.
- STEAD, R. J. and HELMBERGER, D. V. (1986), *Progress in modeling strong motions of NTS* (abstract), *EOS, Transactions of the American Geophysical Union* 67, 1093.
- TAYLOR, S. R. (1983), *Three-dimensional crust and upper mantle structure at the Nevada Test Site*, *J. Geophys. Res.* 88, 2220-2232.

Received March 15, 1987, revised August 11, 1987, accepted August 15, 1987)

Section 3

Inversion of P Coda for Isotropic Scatterers at the Yucca Flat Test Site

(Accepted for Publication in Bulletin of the Seismological Society of
America; Authors Christopher S. Lynnes and Thorne Lay)

Abstract

Although many studies have addressed the statistical properties of *P* coda, there have been few attempts to analyze coda in a deterministic framework. In this analysis, 1050 teleseismic *P* wave seismograms from 32 Yucca Flat explosions are inverted for the locations of any isotropic point scatterers in the source region that contribute coherent arrivals to the coda. A rectangular grid of potential scattering locations is constructed around the source array and the semblance (a measure of waveform ensemble coherence) for each point is computed by slant-stacking the full set of seismograms at various moveout velocities. The potential "resolution", or sensitivity, of the method for this data set is tested by constructing a corresponding suite of synthetic seismograms with direct arrivals plus arrivals from various point scatterers and calculating the semblance at each point on the grid. The particular source-station geometry produces better sensitivity near the array. Sensitivity is enhanced parallel to the trend of the elongated source array and diminished in the orthogonal direction. Stacking the data for a velocity of 2.5 km/s yields relatively high semblance values in the central portion as well as about 10 km to the ENE, and moderately high semblance values about 10 km to the WNW. The latter two regions are associated with topographic highs. Simulations using synthetics with random arrivals in the coda indicate that incomplete suppression of random noise may explain the high semblance values in the central region, but probably not in the outlying regions. However, simulations of a circular distribution of random scatterers within 10 km of the test site produce high semblance about 10 km to the ENE, similar to that seen for the data, due to variable

sensitivity. Thus, two possible explanations for the high semblance values are scattering of higher mode surface waves to *P* waves off topographical irregularities, or random scattering due to heterogeneity in the area of the test site.

Introduction

P coda, the complex waveform that follows the direct *P* arrival, has been studied from many different perspectives. Coda duration has been used for many years to determine the size of local earthquakes (e.g. Aki, 1969). *P* coda amplitudes have also been used for teleseismic source size estimation, because it is generally believed that coda consists of scattered waves, and therefore averages out the effects of lateral heterogeneity on wave amplitudes by sampling a large volume (Aki, 1982). The scattering models have led to widespread use of coda decay as a method for determining attenuation (e.g. Aki and Chouet, 1975). Several workers have applied random media theory (Chernov, 1960) to coda in order to define the strength and scale length of inhomogeneities under seismic arrays (Aki, 1973; Capon, 1974; Berteussen *et al.*, 1975). Herraiz and Espinosa (1987) present a comprehensive review of coda research, and their terminology will be followed in this paper.

While there has been substantial success in explaining various properties of coda using statistically based methods, there have been only a few attempts to treat coda in a deterministic framework by identifying actual scattering structures. Key (1967) was able to distinguish discrete arrivals in the *P* coda recorded at the Eskdalemuir array and attributed them to scattering from specific topographic features near the array. Lay (1987) stacked *P* coda from underground explosions at the Pahute Mesa test site in Nevada in an attempt to identify contributions from isotropic scatterers in the source region. However, most potential scattering locations that produced any waveform coherence also produced enhanced coherence in simulations using random noise, lead-

ing to some ambiguity in the final result. In this study, we apply the basic methodology introduced by Lay (1987) to explosions at the nearby Yucca Flat test site (Figure 1), in an attempt to identify near-source isotropic scatterers.

There is some reason to anticipate that the Yucca Flat source array might be a more favorable site than the Pahute Mesa array for seeking scattering origins. The Yucca Flat source array is significantly denser, and there is less variation in explosion size. Also, a study by Lynnes and Lay (1988) demonstrated a strong correlation of coda excitation with position in the Yucca Flat source array, indicating significant near-source contributions to the P coda.

Methodology

The methodology of the inversion for isotropic scatterers is summarized briefly below. A more complete development is given in Lay (1987). The technique essentially consists of: assuming an x - y location where primary waves traveling at horizontal phase velocity v_s are scattered isotropically to teleseismic P waves; computing the appropriate time lags for each source-station pair; stacking the seismograms using these time lags; and computing the semblance for a specified time gate. A high semblance value for a given x - y location and assumed moveout velocity (v_s) indicates that a coherent arrival can be identified, suggesting the presence of a structure that can be approximated as an isotropic point scatterer. If forward or back scattering dominate rather than isotropic scattering, the coherence will diminish but should not be eliminated so long as many seismograms are used.

The scattered arrival time lags (τ_{ij}), relative to the direct P arrival, are given by:

$$\tau_{ij} = [(x_s - x_i)^2 + (y_s - y_i)^2]^{1/2} [v_s^{-1} - p_j \cos(\theta_i - \phi_j)] \quad (1)$$

where x_i, y_i are the coordinates of the source, x_s, y_s are the coordinates of the hypothetical scatterer, p_j is the horizontal ray parameter for the secondary teleseismic P waves traveling to the j^{th} station, θ_i is the azimuth from the source to the hypothetical scatterer, and ϕ_j is the azimuth from the scatterer to the j^{th} station (Figure 2). The seismograms are then stacked after applying the appropriate time lags, and the semblance (Neidell and Taner, 1971) of the stack is computed in order to assess whether any waveform coherence can be associated with the given x - y location and scattering velocity. The semblance for N_e events and N_r stations is:

$$S(x_s, y_s, v_s) = \frac{\sum_t \left\{ \sum_{i=1}^{N_e} \sum_{j=1}^{N_r} \delta_{ij} s_{ij}[t + \tau_{ij}(x_s, y_s, v_s)] \right\}^2}{M \left\{ \sum_t \sum_{i=1}^{N_e} \sum_{j=1}^{N_r} \delta_{ij} s_{ij}^2(t) \right\}} \quad (2)$$

where T_g is the time gate over which the semblance is computed, M is the total number of seismograms, $s_{ij}(t)$ is the seismogram from the i^{th} source at the j^{th} receiver, and δ_{ij} is 1 if there is an observation for the i^{th} source at the j^{th} receiver and 0 if there is not. The semblance can be viewed as the power of the stack normalized by the total power in the seismograms, and it varies between 0 and 1, unity being perfect waveform coherence. Semblance is also closely related to the energy-normalized cross-correlation (Neidell and Taner, 1971). The time gate (T_g) used in the semblance computations in this study is 2 s, corresponding to the characteristic pulse duration in the short-period recordings. Tests on synthetic data using a longer time gate of 3 s did

not significantly change the semblances.

The F -test can be applied to a given semblance value to determine whether it is statistically significant. The F value for a non-central distribution (F') is related to the semblance by the expression (Douze and Laster, 1979):

$$F'(N_1, N_2, k) = \frac{S(M-1)}{(1-S)} \quad (3)$$

N_1 and N_2 are the degrees of freedom, and k is the non-centrality parameter, defined as (Blandford, 1974):

$$\begin{aligned} N_1 &= 2BT_g \\ N_2 &= N_1(M-1) \\ k &= N_1 \frac{P_S}{P_N}, \end{aligned} \quad (4)$$

where B is the bandwidth of the signal, P_S is the mean power of the signal and P_N is the mean power of the noise in the frequency band under consideration. The F statistic for a non-central distribution (F') can be approximated by the F statistic for a central distribution (Zelen and Severo, 1965):

$$\begin{aligned} P(F' | N_1, N_2, k) &\approx P(F | N_1^*, N_2) \\ F &= F' \frac{N_1}{N_1 + k} = \frac{F'}{1 + P_S/P_N} \\ N_1^* &= \frac{(N_1 + k)^2}{(N_1 + 2k)} = N_1 \left[1 + \frac{(P_S/P_N)^2}{(1 + 2P_S/P_N)} \right] \end{aligned} \quad (5)$$

The statistical significance can then be assessed from standard tables using the F value with N_1^* and N_2 degrees of freedom. The validity of the statistical measure requires

assumptions about the noise properties, which are not generally satisfied by the raw data. However, weighting functions, such as those described in the data analysis section below, can be used to suppress correlated noise, allowing the use of the F -test.

Data Analysis.

The P waves that we analyze here were recorded on short-period instruments at 65 teleseismic (25° – 95°) WWSSN and Canadian Seismic Network (CSN) stations. Records from 32 underground explosions at the Yucca Flat test site were used, yielding a total of 1050 recordings. The first 25 s of the P wavetrain were digitized on all of the seismograms. In order to obtain a uniform database, the CSN records were multiplied in the frequency domain by the ratio of the standard WWSSN instrument response to the individual CSN instrument responses, thus equalizing the CSN seismograms to WWSSN-type recordings. A zero-phase three-pole Butterworth bandpass filter from 0.2 to 2.0 Hz was applied to minimize digitization, instrument, and earth noise. The seismograms were also normalized to the peak amplitude in order to suppress the amplitude effects of variable explosion yield, attenuation and focusing/defocusing. In order to obtain more uniform azimuthal coverage, the seismograms within 7.5° azimuth windows were averaged, reducing the number of independent observations from 1050 to 816.

The semblance procedure relies on correlating similar features occurring at different times in the full set of seismograms due to the directivity of the scatterer. Consequently, it is helpful to remove features that occur at the same time in a large subset of seismograms. The most obvious such feature is the direct arrival itself,

which normally has distinctive characteristics due to both source and receiver effects. Other coherent arrivals might be produced by slapdown or aftershocks, which would be common to all seismograms for a given source, and scattered arrivals from the vicinity of a given station, which would be similar for all seismograms at that receiver. In an attempt to minimize the effects of these features, time-dependent weighting filters were applied to the seismograms ($s_{ij}(t)$) before stacking:

$$s'_{ij}(t) = s_{ij}(t)[1 - w_e e_i(t)][1 - w_r r_j(t)] \quad (6)$$

where w_e and w_r are constants between 0 and 1, $e_i(t)$ is the normalized envelope of the stacked traces for the i^{th} event, and $r_j(t)$ is the normalized envelope of the stacked traces for the j^{th} station. These filters downweight receiver effects and the direct arrival, which would otherwise dominate the semblance computations and result in high semblances centered on the sources. A wide range of values and combinations of the weighting constants w_e and w_r was explored, with a value of 0.75 for both constants producing good results in simulations using synthetic data sets. This choice of w_e and w_r is kept fixed below.

Tests Using Synthetic Data

In order to assess the intrinsic ability of our particular source-station geometry to resolve the locations and scattering velocities of isotropic point scatterers, we conducted several synthetic experiments. Synthetic seismograms were computed comprising a direct arrival and a P wave scattered at a specified moveout velocity and location, with a prescribed amplitude relative to the direct arrival. The seismograms were

formed using a modified Haskell source (Helmberger and Hadley, 1981), a short-period WWSSN instrument response and a Futterman Q operator with t^* of 0.4 s. A seismogram was constructed for each source-station pair contributing to the actual data set. The semblance was then calculated at each point on a square 19×19 grid centered on the Yucca Flat test site, with a grid spacing of 2 km. The x coordinate increases to the east, and the y coordinate increases to the north. The results of a simulation for a point scatterer with a horizontal phase velocity (v_s) of 2.5 km/s are shown in Figure 3. The figure on the left (Figure 3a) shows the grid points at which semblances were computed, with the closed circle indicating the position of the scatterer producing the "coda" arrival in the synthetic seismograms. A perspective plot of the semblance at each grid point computed for this seismogram suite, assuming a scattering velocity of 2.5 km/s, is shown in Figure 3b. The highest semblance (1.0) is found at the correct location for the scatterer, although several neighboring locations also produce high semblance values due to spurious coherence, resulting in limited spatial sensitivity, or "resolution". (Note that this is not a standard mathematical inversion in that the semblance at a given point is independent of the semblance at other points, and model parameters are not obtained directly. Hence, the resolution is not strictly defined, and behaves differently than for a linear inversion.)

We also attempted to assess the effect of noise on the semblance calculations by adding arrivals with random delay times and amplitudes to the synthetic seismograms for a single point scatterer. The effect of adding 50 random arrivals to each waveform in the previous synthetic seismogram set is shown in Figure 3c. The random arrivals have uniform distributions of amplitude relative to the direct arrival (with ratios

between -0.5 and 0.5), and of arrival times within the window of the seismogram. The peak semblance is significantly reduced, as might be expected due to the addition of noise. However, the noise reduces the semblance values of the surrounding grid points even more, resulting in increased spatial sensitivity for the synthetic data set.

At first sight, the apparent enhancement of "resolution" with the addition of noise is somewhat paradoxical. The explanation lies in the nature of the semblance statistic. Since semblance is formed by summing lagged traces rather than multiplying them, small misalignments can still produce high semblance values if the waveforms are sufficiently similar. When random arrivals are added to the waveforms, they degrade the semblance at all of the locations. However, the large number of waveforms still produces a significant semblance at the precise location for which the waveforms are correctly aligned.

Another apparent paradox in the high resolution is that the time differences associated with nearby grid points are quite small, about 0.1 – 0.2 s. Thus the resolution is better than might be expected from the high frequency corner of the filter (2 Hz). This is due to the influence of phase information in the semblance technique, which can be recovered even from the lower frequencies.

The ability of the technique to resolve the horizontal phase velocity of the waves scattered by a point scatterer was tested by computing the semblances for several different assumed moveout velocities, using the same suite of synthetics as the above simulation of a point scatterer plus random noise (Figure 4). The highest peak semblance value occurs for the semblances calculated for a velocity of 2.5 km/s, the correct velocity (Figure 4b). The low semblances for the other scattering velocities

(Figure 4a, c) indicate that the velocity can be resolved well for a single point scatterer in this source-station geometry. This is important for identifying what type of scattering is occurring.

Since the variation of delay times of scattered arrivals depends strongly on the source-station geometry, the peak semblance and spatial resolution may vary in different parts of the source region. To characterize these variations, we computed 81 suites of synthetic seismograms, assuming single point scatterers at x, y (E, N) = 0 km, ± 4 km, ± 8 km, ± 12 km, and ± 16 km (Figure 5), scattering waves with a scattering velocity (v_s) of 2.5 km/s. The point scatterers radiated waves with half the amplitude of the direct arrival, and 50 random noise arrivals were also added to each seismogram. The semblances for the full 19×19 grid ($x = -18 \rightarrow +18$ km, $y = -18 \rightarrow +18$ km) were then calculated for each set of seismograms at the correct stacking velocity (2.5 km/s). The semblance surfaces for four of the simulations are shown in Figure 6. In each case, the actual location of the scatterer can be identified as the point with the highest semblance. Interestingly, the peak semblance for a point scatterer in the middle of the array (Figure 6d) is smaller than for scatterers in other locations. This is due to contamination from the direct arrivals and the effects of the weighting functions. Another interesting feature is the anisotropic nature of the resolution for points outside the array (Figure 6a-c), with the semblances dropping off from the peak semblance less rapidly in the NE-SW direction than in the NW-SE direction.

The peak semblances for all 81 simulations are shown in Figure 7. As mentioned above, point scatterers near the middle of the source array actually produce relatively low semblance values. Excluding these locations, the peak semblances are roughly

equal for different positions in the source region.

We chose to characterize the variable spatial resolution by a two-dimensional "spread function". The spread function was computed by comparing the semblance at an actual scatterer location (S_{\max}) with the semblances calculated at each of the eight adjacent points. For each azimuth (ϕ) from the actual location to the adjacent point, the spread ($\sigma(\phi)$) is defined in terms of S_{\max} and the semblance at the adjacent point in that direction, S , as:

$$\sigma(\phi) = 1 - \frac{\Delta S}{S_{\max}},$$

$$\Delta S = S_{\max} - S \quad \text{for } \phi = 0^\circ, 90^\circ, 180^\circ, \text{ and } 270^\circ, \quad (7)$$

$$\Delta S = \frac{(S_{\max} - S)}{\sqrt{2}} \quad \text{for } \phi = 45^\circ, 135^\circ, 225^\circ, \text{ and } 315^\circ.$$

The spread in a given direction is equal to 1 for negligible spatial resolution over the given grid spacing ($S_{\max} = S$) and is equal to zero for perfect resolution, ($S = 0$). Thus, the spread function is essentially reciprocal to the resolution. The results are presented as octagons, with the distance from the center to each vertex proportional to the spread function in that direction. A large octagon represents a large spread function in all directions, implying poor spatial resolution of a scatterer at that point, while a small octagon indicates a small spread function and good resolution. An equidimensional octagon would indicate equal resolution in each direction. However, most of the spread functions show a pronounced elongation in the NE-SW direction, indicating poorer resolution in this direction than in other directions. This is probably due to the roughly linear NW-SE trend of the source array. The best resolution (smallest spread

function) appears to be immediately to the ENE and WSW of the array. These characteristics can be compared with the analogous variations for the Pahute Mesa array geometry examined by Lay (1987) to gain an appreciation for the effects of source distribution.

Inversion of Real Data

The actual data set was inverted for isotropic point scatterers using the same grid as in the synthetic cases (Figures 4–7), for moveout velocities of 1.5 km/s, 2.5 km/s and 3.5 km/s (Figure 8). All of the semblance surfaces have relatively high values in the center. The two higher moveout velocities also appear to have a high semblance area about 10 km to the ENE of the Yucca Flat source array, and a ridge of moderate values 10 km WNW of the array. Both of these areas are regions of fairly good resolution, according to the simulations (Figure 7). However, the high semblance area in the data does seem to be somewhat elongated in the direction orthogonal to the trend of the source array (i.e., NE-SW), as predicted by the resolution experiment (Figure 7). Semblances were also computed for moveout velocities of 1.0 km/s, 2.0 km/s, 3.0 km/s, and 4.0 km/s. The high semblance feature to the ENE appears for all velocities higher than 2.0 km/s. All stacking velocities produce high semblances in the central region.

In order to test the stability of the results, the semblance was computed for three subsets of the data: the 16 most northerly events, the 16 most southerly events, and the 16 largest events. In each case, the overall semblance values for all of the moveout velocities were higher by a factor of 2–3 for the subsets than for the full set of data.

Qualitatively, the semblance surfaces for the subsets were quite similar to those for the full set, except that the semblances for the subsets were disproportionately high in the center of the region. This is probably due to spurious waveform coherence associated with the direct arrivals.

Unlike the simulations, the peak semblances for the full set of real data are extremely low, on the order of 0.02–0.03 (Figure 8). However, these values are actually somewhat higher than those obtained for Pahute Mesa by Lay (1987) when station and event weighting were applied. In fact, a semblance of 0.02 yields an F' value of 16.6, with degrees of freedom $N_1=7.2$ and $N_2=5868$. Of course, the statistical significance depends on the signal to noise ratio, which is unknown. If we assume a signal/noise ratio of 0, then $F=F'$, and a semblance of 0.02 is significant at the 99% level. On the other hand, if we assume that the signal/noise power ratio is equal to 2, $F=F'/3=5.5$, and $N_1^* = 1.8N_1 = 13.0$, which is still significant at the 99% level.

In any case, even the highest semblances in the real data are low enough to cause concern that they might be due simply to incomplete suppression of noise caused by the source-station geometry. To test this possibility, semblances were computed for a suite of synthetic seismograms comprising the direct arrival and 50 random arrivals, varying in amplitude between -0.5 and 0.5 relative to the direct arrival. The synthetic seismograms were computed for the same source-station pairs as the data. The semblances were computed assuming a stacking velocity of 2.5 km/s (Figure 9a). The moveout velocity of 2.5 km/s was chosen because it appears to produce more stable semblance surfaces for the data than the higher moveout velocities. A velocity of 2.5 km/s is probably too fast for short-period fundamental mode Rayleigh waves, since the

S wave velocities of the basin sediments are about 1 km/s and the Paleozoic basement is about 2.6 km/s (Ferguson, 1982). However, this is a reasonable velocity for higher mode surface waves.

The peak semblance in the random simulation is surprisingly high (0.11), suggesting that many of the higher semblances in the data stacks may be artifacts. However, the high semblances are mostly confined to the center of the grid, in proximity to the source array. This is likely due to the residual coherence of the direct arrivals, which is not completely removed by the station and event weighting filters. The lack of appreciable semblance in the random simulations at outlying locations suggests that random noise can not explain high semblance in the data (Figure 9b) away from the central region of the source array. The random noise simulations produce simpler semblance surfaces than do similar simulations for Pahute Mesa (Lay, 1987), probably due to the closer spacing of the Yucca Flat events.

Since the highest semblance values occur in a region where the spatial resolution is greatest, it is also possible that the distribution of scatterers is random, but high semblances are found only for points where the spatial resolution is favorable. In order to test this hypothesis, we computed synthetic seismograms for a set of 70 scatterers with random amplitudes up to 0.2 the amplitude of direct arrival, stacking velocity of 2.5 km/s, and positions within 10 km of the center of the grid. No random noise arrivals were added to the seismograms. The locations and amplitudes of these scatterers are shown in Figure 9c. The semblance was then computed for each grid point assuming a scattering velocity of 2.5 km/s (Figure 9d). The semblances are again quite high (up to 0.24). In contrast to the random noise case, however, the

random scatterer simulation produces relatively low semblance values in the central region, but higher semblances in the area to the northeast where the high semblances were located in the data inversions. Thus, while the technique finds high semblance in some areas where scatterers are located, it fails in this case to locate other scatterers, apparently due to the sensitivity characteristics imposed by the array geometry.

Discussion

Several studies have indicated that topography is a major contributor to *P* wave coda. Using a statistical approach, Greenfield (1971) was able to model the energy flux of coda from Novaya Zemlya explosions by hypothesizing Rayleigh→*P* scattering by the island coastline, river valleys and other topography. Key (1967) used standard array analysis to determine the location and phase velocity of coherent arrivals in the *P* coda at the Eskdalemuir array. The locations were generally associated with topographic highs. Key (1967) found one particularly strong arrival to be associated with a river valley, with a phase velocity of 2.5 km/s, suggesting *P*→Rayleigh scattering near the receiver. Synthetic calculations also indicate a scattering role for topographical highs. McLaughlin and Jih (1988) computed 2-D finite difference synthetics for Rayleigh waves incident on a mesa. The resulting wavefield includes both forward and back scattered *P* waves. In order to see if topography can explain the high semblance regions located in this study, the semblances computed from the data with a stacking velocity of 2.5 km/s are superimposed on a topographic map of the region in Figure 10. Indeed, the isolated high-semblance area to the east is associated with a similarly isolated topographic high in the Halfpint Range. The ridge to the west also correlates

with moderately high semblance values. Thus, waves scattered from topographical irregularities seem to be a plausible explanation for some of the early *P* coda for Yucca Flat explosions. However, the semblances in the northwest area of the grid, where the topography is the highest, are rather low. If the topography does produce the majority of the coda, the low semblances might be due to the shape of the topographic high. On the other hand, the random scatterer simulation indicates that an equally valid explanation of the semblances derived from the data would be a random distribution of scatterers in the central region of the test site, which is quite flat.

In summary, the semblance technique has yielded somewhat ambiguous results in terms of identifying deterministic scatterers. Indeed, the simulations seem to indicate that random scatterers explain the data equally well. The main problem seems to be that the source array geometry exercises strong control on the sensitivity of the technique. This has been the case both for the two-dimensional Pahute Mesa source array (Lay, 1987) as well as the linear Yucca Flat array.

However, an additional factor may be the limitations of the data set, which may obscure more significant features that would yield high semblance in areas of the test site that are not favored by the array geometry. For instance, the use of analog, rather than digital, data places a severe constraint on the frequency range that can be reliably used. Digital data bases of substantial size are now accumulating for more recent events. Another factor that probably decreases the semblance of the waveforms is the influence of lateral heterogeneity on the travel time from the source to the scatterer. Accounting for this effect could result in improved alignment of the waveforms. Also, isotropic scattering was assumed, a condition that could be relaxed to allow for

radiation patterns. For NTS, this assumption is not particularly unrealistic: due to the low velocities near the surface, the teleseismic *P* waves leave the source area in a very narrow cone of rays. Furthermore, the synthetic results of McLaughlin and Jih (1988) indicate that Rayleigh→*P* scattering from topography is roughly isotropic for wavelengths that are significantly greater than the height of the irregularity. One modification of the technique that might produce some improvement in the results would be an inversion of the coda envelopes, rather than the seismograms themselves. This would mitigate the effects of phase incoherence and receiver and source characteristics that influence the dominant frequencies in the seismograms. However, the use of envelopes would dramatically decrease the bandwidth; also, the statistics of cross-correlation of such one-sided functions are not so well-developed as for oscillatory waveforms.

Conclusion

P wave seismograms from 32 Yucca Flat explosions were inverted for isotropic point scatterers in the source region by computing the semblance for hypothetical scatterers at a series of locations. Synthetic experiments show the ability of the semblance analysis to identify strong point scatterers, with the attainable resolution varying with position and direction in the source region. The resolution is generally best within a few kilometers of the source array, and is better in the NW-SE direction than in the NE-SW direction due to the trend of the source array.

The semblances of the real data, while indicating much lower waveform coherence than for the simulations, are relatively high about 10 km ENE of the source array,

and moderately high about 10 km WNW of the array, as well as in the immediate vicinity of the array, for a moveout velocity of 2.5 km/s. Analysis of signals with random noise yields high semblances in the center as well, suggesting that semblances in this area may be artifacts of the source-station geometry and contamination by the direct arrivals. However, random noise does not appear to explain the high semblance values to the ENE and WNW. The high semblance area to the ENE is associated with an isolated topographic high, suggesting that topographic irregularities may play an important role in coda generation. However, a simulation of random scatterers produced high semblances in the same area ENE of the array as the data, indicating that a random distribution of scatterers in the vicinity of the test site might also explain the results.

Acknowledgments

Judi Sheridan and Martha Ballard digitized the majority of the seismograms used in this study. The use of the film chip library at the Lamont-Doherty Geological Observatory is also gratefully acknowledged. We thank Christopher Young, Howard Patton, David Harris and an anonymous reviewer for useful comments on this work. This research was supported by the Sloan Foundation, a Shell Faculty Career Initiation Grant, and the Defense Advanced Research Projects Agency, and was monitored by the Air Force Geophysics Laboratory under Contract F19268-87-K-0010.

References

- Aki, K., 1969. Analysis of the seismic coda of local earthquakes as scattered waves, *J. Geophys. Res.*, **74**, 615-631.
- Aki, K., 1973. Scattering of *P* waves under the Montana LASA, *J. Geophys. Res.*, **78**, 1334-1346.
- Aki, K., 1982. Scattering and attenuation, *Pull. Seism. Soc. Am.*, **72**, S319-S330.
- Aki, K., and Chouet, B., 1975. Origin of coda waves: source, attenuation and scattering effects, *J. Geophys. Res.*, **80**, 3322-3342.
- Berteussen, K. A., Christoffersson, A., Husebye, E. S., and Dahle, A., 1975. Wave scattering theory in analyses of *P* wave anomalies at NORSAR and LASA, *Geophys. J. Roy. Astr. Soc.*, **42**, 403-417.
- Blandford, R. R., 1974. An automatic event detector at the Tonto Forest seismic observatory, *Geophysics*, **39**, 633-643.
- Capon, J., 1974. Characterization of the crust and upper mantle structure under LASA as a random medium, *Bull. Seism. Soc. Am.*, **64**, 235-266.
- Chernov, L. A., 1960. *Wave Propagation in a Random Medium*, McGraw-Hill, New York.
- Douze, E. J., and Laster, S. J., 1979. Statistics of semblance, *Geophysics*, **44**, 1999-

2003.

- Ferguson, J. F., 1982. Geophysical investigations of Yucca Flat, Nevada, in *Final Technical Report to the AFOSR*, Contract no. F49620-81-C-0010.
- Greenfield, R. J., 1971. Short-period P-wave generation by Rayleigh-wave scattering at Novaya Zemlya, *J. Geophys. Res.*, **76**, 7988-8002.
- Healey, D. L., 1968. Application of gravity data to geologic problems at Nevada Test Site, in *Nevada Test Site*, ed. E. B. Eckel, GSA Memoir No. 110, 147-156.
- Helmberger, D. V. and Hadley, D. M., 1981. Seismic source functions and attenuation from local and teleseismic observations of the NTS events JORUM and HANDLEY, *Bull. Seism. Soc. Am.*, **71**, 51-67.
- Herraiz, M., and Espinosa, A. F., 1987. Coda waves: a review, *PAGEOPH.*, **125**, 499-577.
- Hinrichs, E. N., 1968. Geologic structure of the Yucca Flats Area, Nevada, in *Nevada Test Site*, ed. E. B. Eckel, GSA Memoir No. 110, 239-246.
- Key, F. A., 1967. Signal-generated noise recorded at the Eskdalemuir seismometer array station, *Bull. Seism. Soc. Am.*, **57**, 27-37.
- Lay, T., 1987. Analysis of near-source contributions to early *P* wave coda for underground explosions: 3. Inversion for isotropic scatterers, *Bull. Seism. Soc. Am.*, **77**, 1767-1783.

- McLaughlin, K. L. and Jih, R. S., 1988. Scattering from near-source topography: teleseismic observations and numerical simulations, *Bull. Seism. Soc. Am.*, 78, 1399-1414.
- Neidell, N. S., and Taner, M. T., 1971. Semblance and other coherency measurements for multichannel data, *Geophysics*, 36, 482-497.
- Zelen, M, and Severo, N. C., 1964. Probability functions, in *Handbook of Mathematical Functions*, fourth edition, ed. Abramowitz, M. and Stegun, I. A., U. S. Government Printing Office, 925-995.

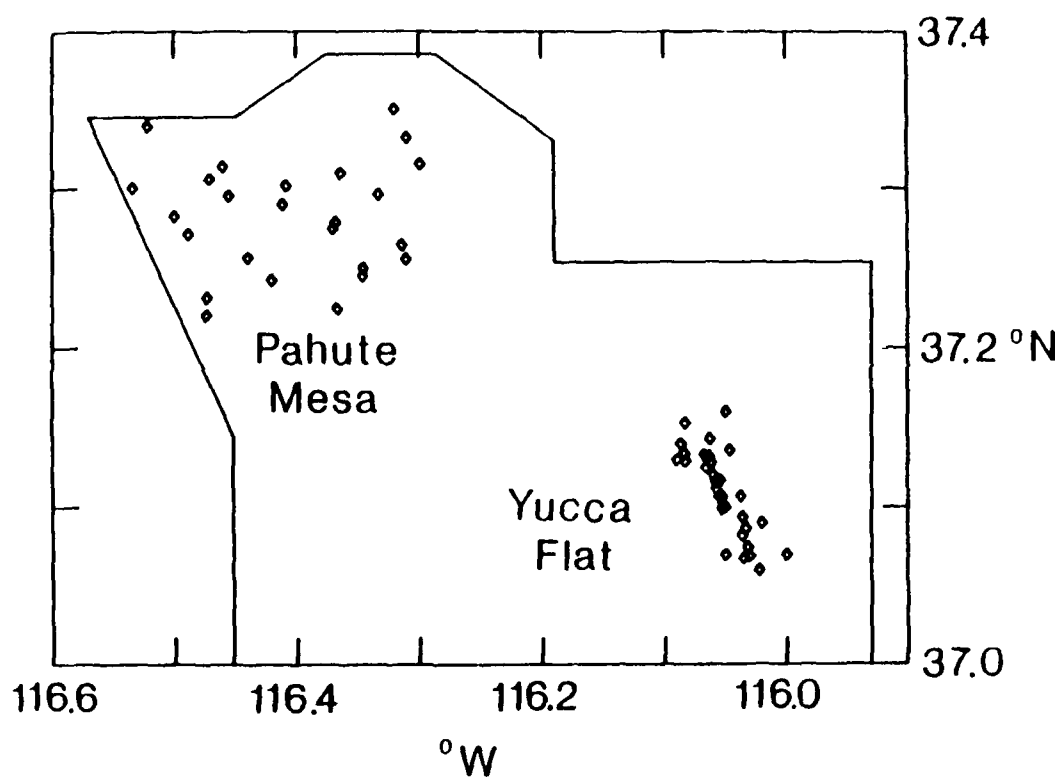


Figure 1. Map of the Nevada Test Site, showing the locations of the Pahute Mesa explosions used by Lay (1987) and the Yucca Flat explosions used in this study.

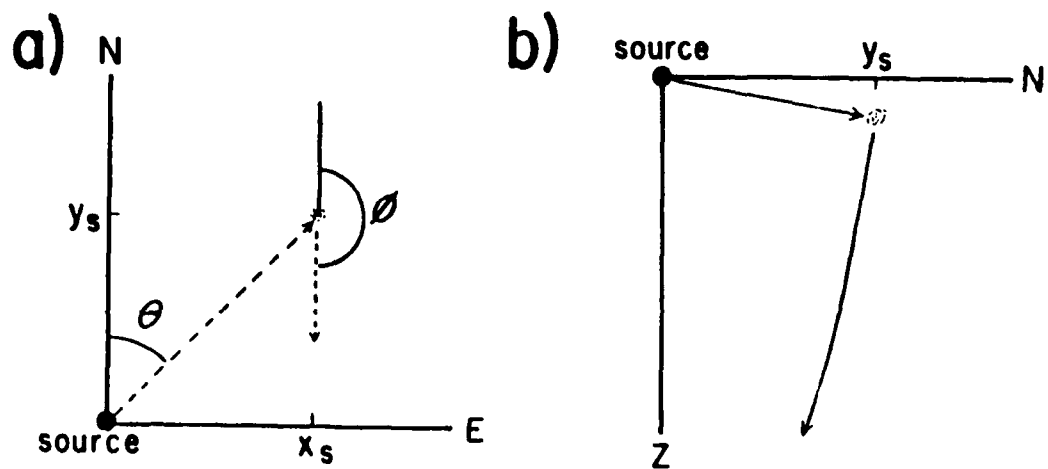


Figure 2. Geometry of the scattering problem, shown in horizontal (a) and vertical (b) projections.

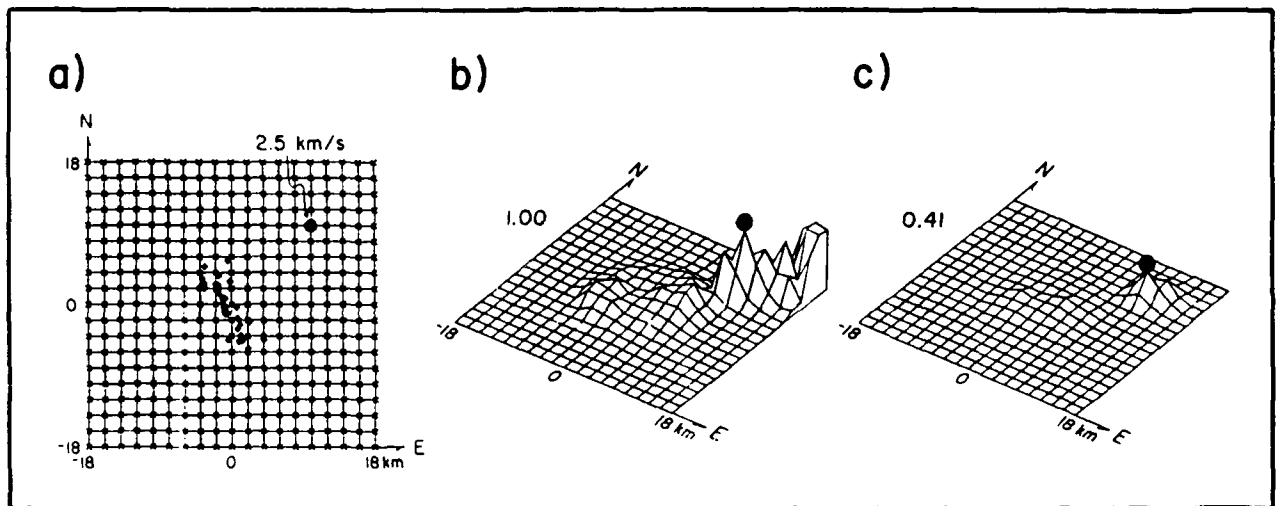


Figure 3. (a) Locations for which semblance was calculated. The diamonds show the locations of the Yucca Flat underground explosions used in this study. The closed circle is the location of the point scatterer contributing to the suite of synthetic seismograms. (b) Perspective plot of semblances for the corresponding suite of synthetic seismograms. The peak semblance value is shown in the upper left. (c) Perspective plot of semblances for a suite of seismograms comprising arrivals from the scatterer in (a), plus 50 random arrivals in each seismogram.

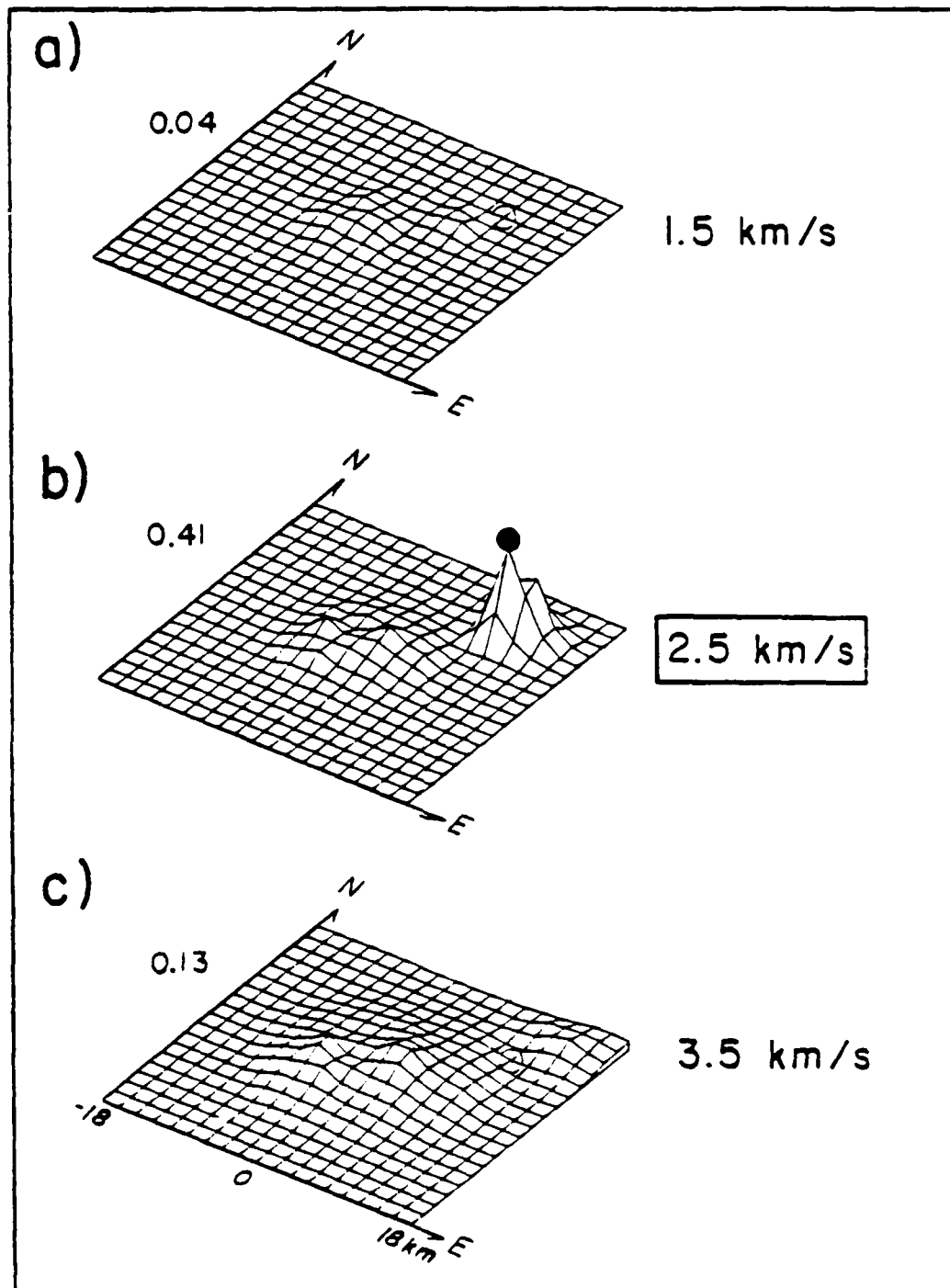


Figure 4. Semblances computed for the suite of synthetic seismograms for the scatterer in Figure 3a, plus random noise. Three different stacking velocities are shown, with the actual one in the middle. The true position of the scatterer is shown by the circle, which is closed for the correct velocity and open for the incorrect velocities.

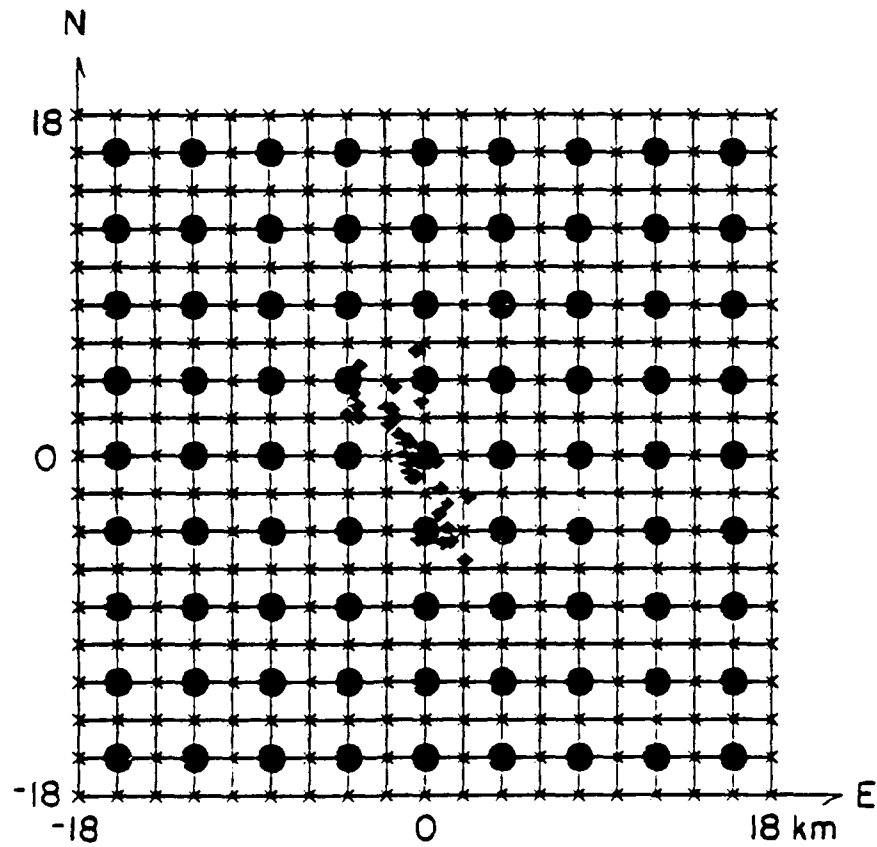


Figure 5. Locations of the point scatterers used in 81 single point scatterer simulations, together with the grid of locations used in the semblance analysis of the synthetic data sets.

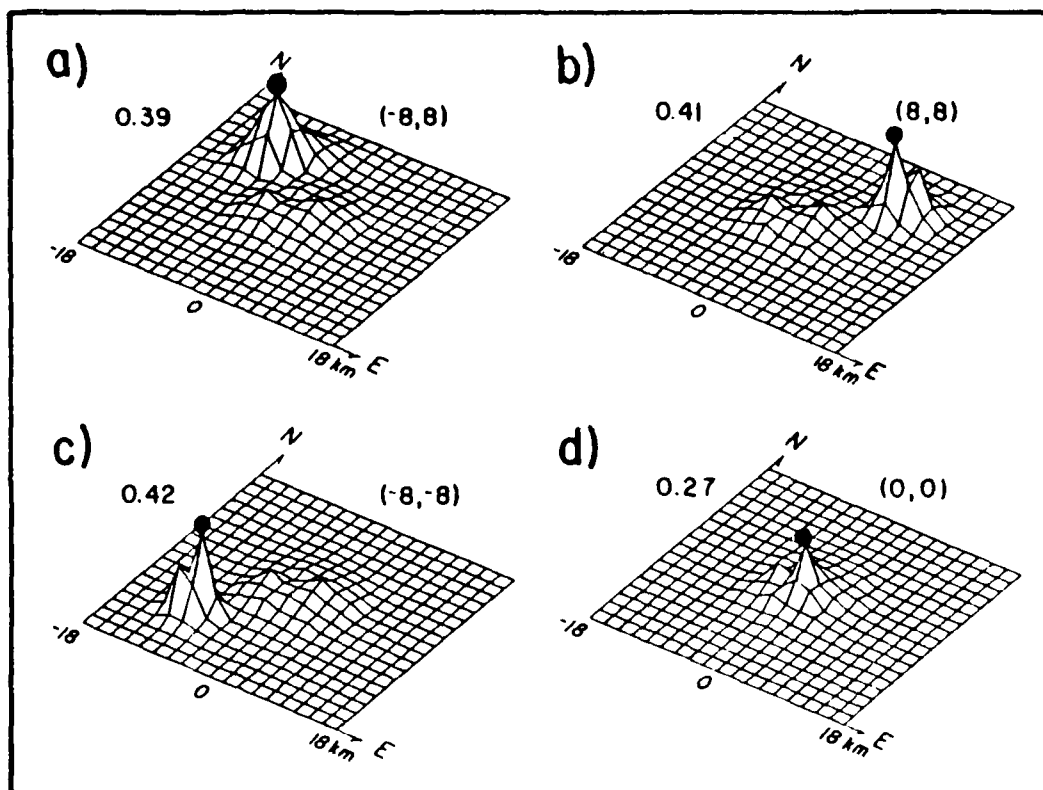


Figure 6. Semblances computed for point scatterers at four of the locations in Figure 5. The numbers in the upper left are the peak semblances for each simulation, and the numbers in the upper right are the x-y coordinates of the point scatterer (located at the closed circle).

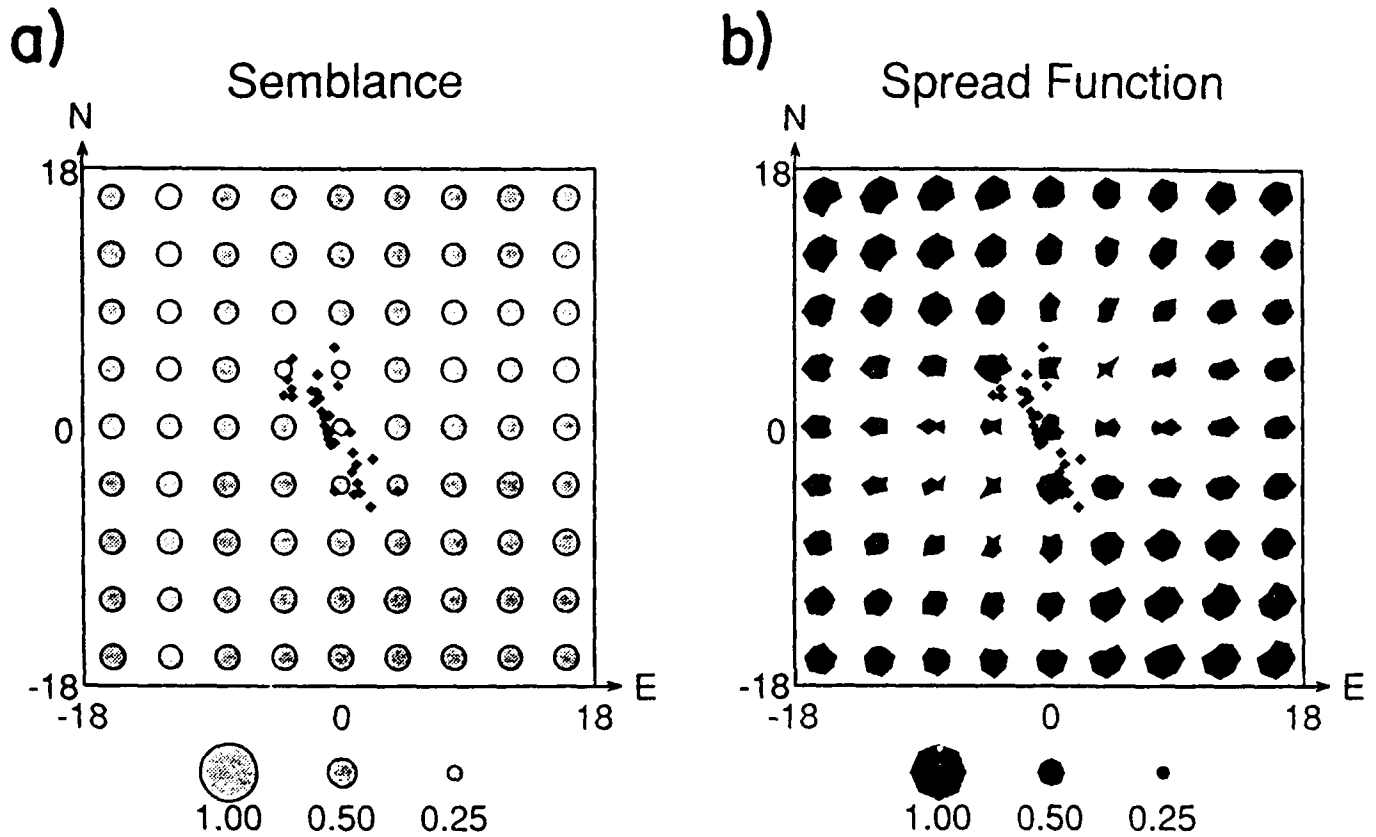


Figure 7. (a) Semblance values (S_{\max}) at the actual scatterer locations for the 81 single point scatterer simulations (see Figure 5). (b) Octagons showing spread functions in eight directions (N, S, E, W, NE, NW, SE and SW) for the same 81 simulations, indicated by the radius to each vertex of the octagon. The spread function varies between 0 (perfect spatial resolution near the peak semblance) and 1 (poor spatial resolution). An equidimensional octagon indicates equal spatial resolution in all directions, and the best overall resolution is for the smaller symbols. See text for a more comprehensive explanation.

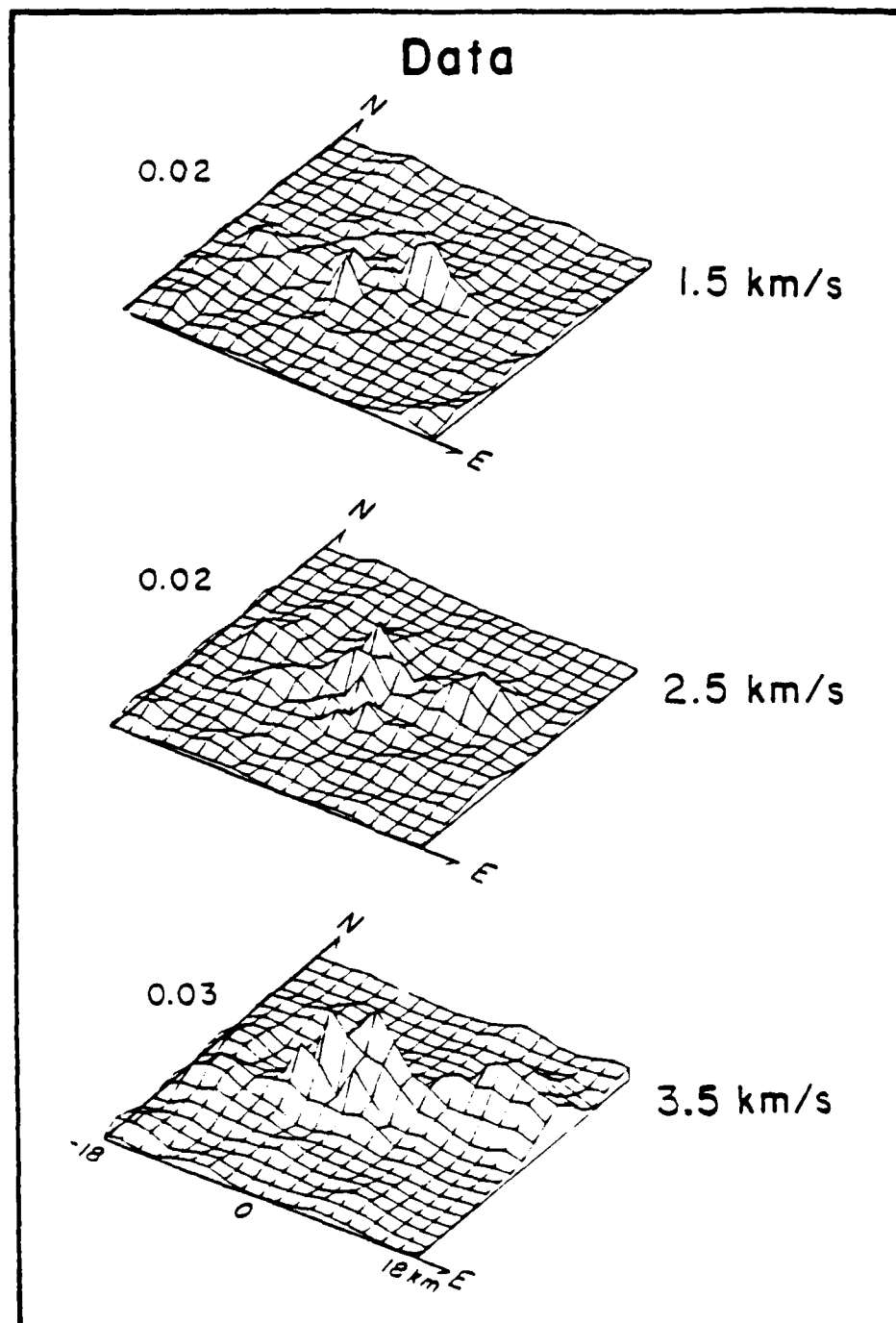
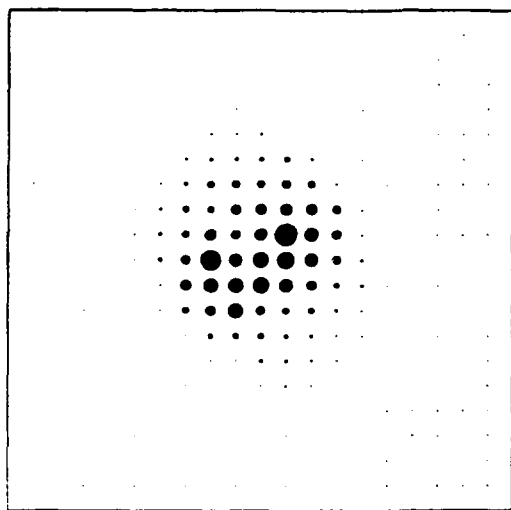


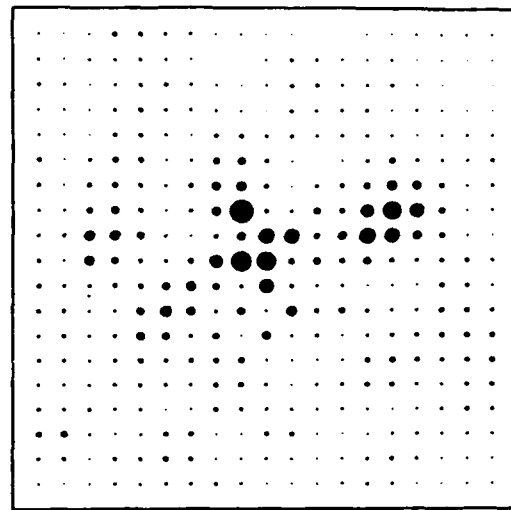
Figure 8. Semblances calculated for the Yucca Flat data set, assuming three different scattering velocities. The peak semblance for each surface is shown in the upper left.

a)



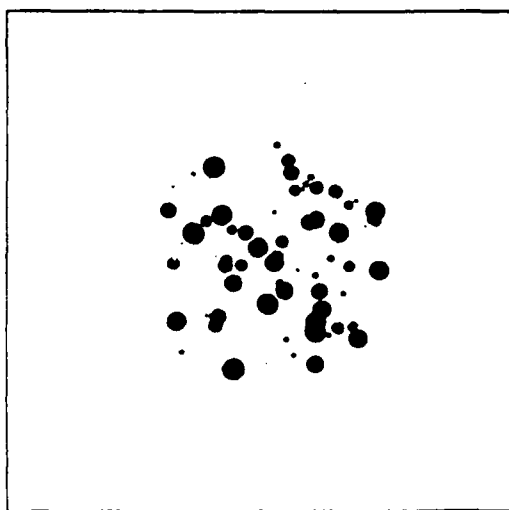
max. semblance=0.11

b)



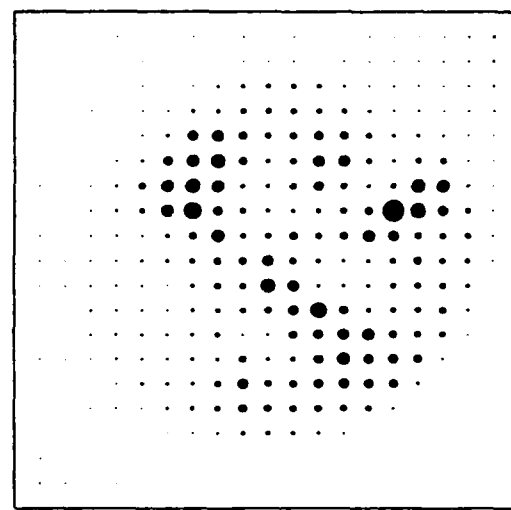
max. semblance=0.04

c)



max. amplitude: 0.2

d)



max. semblance=0.24

Figure 9. (a) Map view of semblances calculated for a random simulation. (b) Map view of semblances from data. (c) Map view of randomly distributed scatterers used in random scatterer simulation. The size of the symbol indicates the amplitude of the scattered arrivals (relative to the direct arrival). (d) Map view of random scatterer simulation. Note the similarity to the map view of the data semblances. The peak value for each surface is shown below each graph, and a stacking velocity of 2.5 km/s was used for all.

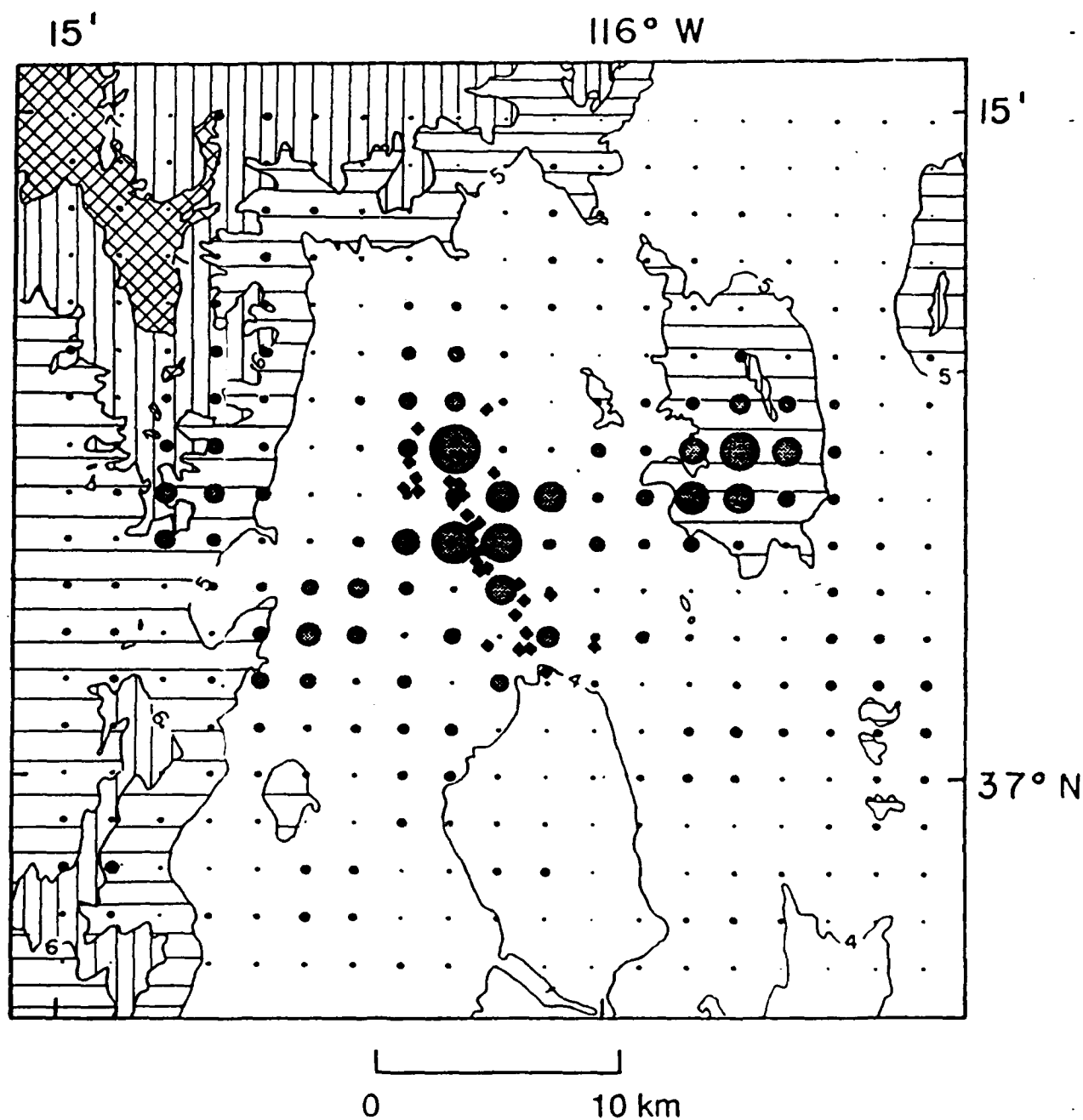


Figure 10. Semblances from Figure 9b, superimposed on a topographic map of the region. The contours are in 1000' intervals.

Section 4

Effects of Lateral Velocity Heterogeneity Under the Nevada Test Site on
Short Period P Wave Amplitudes and Travel Times

(Accepted for publication in Pure and Applied Geophysics; authors Christopher
S. Lynnes and Thorne Lay)

ABSTRACT

Short-period teleseismic *P* waves from the Nevada Test Site (NTS) show systematic variations in amplitudes and travel times, with low amplitudes corresponding to fast travel times, suggesting elastic focussing-defocussing effects. Also, the patterns for events at the Pahute Mesa subsite are systematically different from those at the Yucca Flat subsite, indicating the presence of a near-source component in both the amplitude and travel time variations. This component is isolated by removing the mean station pattern for all of NTS from the observations. A very-near-source component in the Pahute Mesa observations is also isolated by removing subsite station means from the measurements. These anomalies are back-projected through laterally homogeneous structure to form thin lens models at various depths. Travel time delays are predicted from the amplitude variations using the equation for wavefront curvature. The long-wavelength components of the predicted and observed time delays correlate well at depths of 25 km for the very-near-source component under Pahute Mesa and 160 km for the regional component under NTS. The time delay surfaces predicted by the amplitudes at these depths are mapped into warped velocity discontinuities suitable for the calculation of synthetic seismograms using the Kirchhoff-Helmholtz integral formulation. Both the intersite (near-source) and intrasite (very-near-source) differences in amplitudes are qualitatively predicted very well, although the range of variation is somewhat underpredicted. This deficiency is likely due to the destructive interference of anomalies inherent in back-projection to a single layer.

INTRODUCTION

Theoretically, an underground explosion should radiate compressional waves isotropically. However, several studies of short-period *P* waves from explosions (e. g., Lay *et al.*, 1984; Burger *et al.*, 1986) have indicated that amplitudes can have coherent variations with azimuth ranging over factors of 3 to 10. Such variations are important to understand because of the uncertainty they add to underground test size estimation. Furthermore, those variations can be extremely useful in investigating lateral variations in earth structure, particularly when examined in concert with travel time data. Given sufficiently accurate earth models, it may be possible to correct the amplitude variations for propagational effects, thereby improving the accuracy of the size estimates.

In this study, we examine short-period *P* wave amplitudes in conjunction with travel times from underground explosions at the Nevada Test Site (NTS). A previous analysis (Lynnes and Lay, 1987) has established that low amplitudes correlate with fast travel times, implying that variations in velocity, rather than attenuation, are primarily responsible for the amplitude fluctuations. These amplitude variations are used in this study to derive laterally varying velocity structures, parameterized as warped velocity discontinuities that are as compatible as possible with the travel time observations.

Underground explosions at NTS (Fig. 1) provide a dense, well-located array of sources that offers an excellent site for such a study. Also, several travel time studies have already found evidence for significant lateral heterogeneity in the crust and upper mantle beneath NTS (Spence, 1974; Minster *et al.*, 1981; Taylor, 1983), and the geology of the general area is replete with Cenozoic calderas, which might be expected to produce or be related to lateral velocity variations.

A few previous studies have predicted amplitude variations using models derived from travel time data. Thomson and Gubbins (1982) calculated amplitudes for the Norwegian Seismic Array (NORSAR) using a smoothly varying structure obtained by a linear inversion of travel times. Although they found statistically significant correlations

between predicted and observed amplitudes, the predicted amplitude range was much smaller than the observed range. Cormier (1987) traced rays through Taylor's (1983) model of the lithosphere under NTS, producing amplitude variations for a Pahute Mesa explosion that were similar to the observed variations reported in Lay *et al.* (1984). On the other hand, Lay *et al.* (1986) traced rays through the structure derived by Minster *et al.* (1981) from travel times for the same area, finding almost no variation in amplitudes. The two travel time inversions use overlapping data sets of teleseismic travel times, but differ in the parameterization of the model: Taylor's model extends to 100 km depth, and includes information from P_n source terms, while Minster *et al.* invert for perturbations down to 150 km and employ an additional smoothing algorithm in the inversion. The result is that Taylor's (1983) model has velocity perturbations that are larger than in Minster *et al.*'s model by a factor of three and fluctuate more rapidly. The attendant differences in lateral velocity gradients between the two models have a drastic effect on the predicted amplitude variations.

Given the dependence of predicted amplitudes on the parameterization of the travel time models, it would be desirable to obtain a velocity structure from the amplitudes themselves. However, due to the non-linear relationship of amplitudes to velocity structure, such inversions have been few. Haddon and Husebye (1978) projected amplitude variations onto surfaces at depths between 150 and 200 km below the NORSAR array, and used an equation describing wavefront curvature to predict travel time variations due to an infinitely thin lens, obtaining a high correlation with observed travel time residuals. Thomson (1983) inverted amplitudes recorded at NORSAR for a smoothly varying structure using a raytracing formalism, obtaining fairly good amplitude predictions but only moderate correlations of predicted and observed travel times. Thus, amplitudes seem to contain information that is partially complementary to that in the travel times.

Another attempt to produce the amplitude variations at NTS is the forward modeling approach of Scott and Helmberger (1985), who assumed an upwarped Mohorovicic discontinuity. By calculating synthetic seismograms for arbitrary structures using the Kirchhoff-Helmholtz integral technique, they obtained amplitude variations as high as a factor of 2.5. Thus, this type of model shows some promise of explaining the amplitude anomalies from NTS explosions. However, it would be preferable to invert the amplitudes themselves for a candidate structure, rather than using *ad hoc* models.

Our procedure for imaging the velocity structure uses the thin lens projection to construct a model of a warped velocity discontinuity. Travel time delays are computed from the equation of wavefront curvature as in Haddon and Husebye (1978), and are then mapped into topography of a velocity discontinuity. This structure is then tested by computing synthetic seismograms using the Kirchhoff-Helmholtz integral method.

OBSERVED TRAVEL TIME AND AMPLITUDE VARIATIONS

Over 2000 *P* wave *ab* (first-peak-to-first-trough) amplitudes and travel times were measured from waveforms for 57 explosions at the Pahute Mesa and Yucca Flat test sites in Nevada (Fig. 1). The receivers were short-period WWSSN and Canadian Seismic Network seismographs at distances of 25°-95°. A complete statistical analysis of this data set is presented in Lynnes and Lay (1987a). The amplitude data set actually consists of Δm_b values (i.e., deviations from the explosion mean). The station average values for each test site ($_{PM}S_i$ and $_{YF}S_i$) are presented on an equal-area diagram in Fig. 2. The two test sites have similar patterns for both measurements, suggesting that both the amplitude and travel time patterns have a component related to deep path and/or near-receiver effects. However, the deviations from the mean for Pahute Mesa are systematically and coherently larger in each case. These intersite differences indicate a near-source component. In an attempt to minimize the deep path and near-receiver

effects, the mean of the average station anomalies ($[I_{PM}S_i + YF S_i]/2 = NTS S_i$) for the two test sites was removed from the individual travel time and amplitude measurements. This should provide a fairly conservative estimate of the near-source component of amplitude and travel time variation, although there is some potential for effects unique to one subsite to be folded into the data for the other. An independent test of this assumption can be provided in the case of the amplitude data by comparing the root-mean-square of the first five seconds (RMS^{0-5}), which represents the direct arrival, to the root-mean-square of the next ten seconds (RMS^{5-15}), which represents the early coda. The early coda should average out much of the near-source focussing-defocussing effects, thus providing a reference for the direct arrival amplitudes. The station mean values of $\log(RMS^{0-5}/RMS^{5-15})$ are plotted in Fig. 3, along with the individual station mean magnitude anomalies with the regional means removed ($_{PM}S_i - NTS S_i$ and $_{YF}S_i - NTS S_i$). The patterns for Pahute Mesa are strikingly similar in range and sense. The resemblance of the Yucca Flat patterns is somewhat less, probably due to the complex very-near-source structure (Lynnes and Lay, 1987b).

Another important correlation is that between travel times and amplitudes. Fast travel times (negative residuals) generally correspond to low amplitudes, e. g., in the north-northeast of the Pahute Mesa pattern. This type of correlation is generally an indication of focussing-defocussing effects (e. g., Chang and von Seggern, 1980; Butler, 1983). Thermally activated variations in attenuation, on the other hand, would predict a correlation of slow times with low amplitudes (cf., Butler, 1984).

BACK PROJECTIONS OF AMPLITUDES AND TRAVEL TIMES

The procedure for imaging thin lens structures that might produce the observed amplitude and travel time patterns is a simple back-projection of the teleseismic anomalies. The rays are traced through a homogeneous structure, and the appropriate

anomaly is projected to the point below the source area where the ray reaches a given depth (Fig. 4a), in this case 100 km. The structure used is the reference model for NTS used by Taylor (1983) for three-dimensional travel time inversion, on top of the T7 model of Burdick and Helmberger (1978). The projection surface is then gridded, and the values within each grid square are averaged to obtain a bin-averaged projection (Fig. 4b). The bin-averaged projections for depths of 35, 100 and 160 km are shown in Fig. 5 for both the amplitude and travel time data sets. For the shallow depth, the images formed by the travel time and amplitude data are less coherent than the other depths, with mingled negative and positive values. This is due to the strong similarity of patterns for the explosions in a given test site: a structure as shallow as 35 km does not affect all the explosions similarly, leading to destructive interference in the back-projections. At 100 km depth, the images become more coherent, as indicated by the larger groupings of negative values, particularly in the NNE. Both the amplitudes and travel times form a northeast-trending low under the test site. The 160 km projection is fairly similar to the 100 km projection.

A similar procedure can be applied to the deviations from the subsite station mean. In this case, both the event mean and individual station mean for a given test site are subtracted from each measurement. At large depths, the anomalies for a given station will fall in a single bin and average out to zero. Consequently, this component of the data set is most sensitive to very shallow structure.

The back-projections of the individual deviations from the station mean are shown for Pahute Mesa in Fig. 6. The shallowest depth has a relatively incoherent pattern, indicating that no simple structure at this depth can explain much of the magnitude deviations. However, the 25 km deep projection has some very coherent images, particularly the large area of low amplitudes under the north-central part of the mesa. The 50 km deep projection is less coherent and has more bins with zero values, as expected. The corresponding projections for the Yucca Flat test site do not in general

form coherent images. This result is in accord with the hypothesis of Lynnes and Lay (1987b) that the direct arrivals from Yucca Flat are heavily influenced by very shallow structure.

CALCULATION OF TIME DELAYS FROM AMPLITUDE VARIATIONS

The criterion we use for choosing a projection depth is the correspondence of the travel time projection with the travel times predicted by the amplitude projection, calculated using the wavefront curvature equation of Haddon and Husebye (1978). The advance $r(x,y)$ of a plane wavefront at an infinitely thin lens is given as

$$r_{xx} + r_{yy} = [(A/A_0)^2 - 1]/h - h[r_{xx}r_{yy} - (r_{xy})^2], \quad (1)$$

where A/A_0 = relative amplitude,

h = depth of the lens,

and subscripts indicate partial derivatives in cartesian coordinates.

This equation is essentially a non-linear version of Poisson's equation and can be solved for $r(x,y)$ given sufficiently smooth boundary conditions and amplitude variations by calculating the non-linear terms on the right side of the equation from the previous iteration.

Haddon and Husebye (1978) used observed travel time residuals as boundary conditions in their study on the NORSAR array. However, for an irregular geometry such as the NTS explosion array, this choice of boundary conditions risks introducing biases based on a small subset of the travel times. Furthermore, this subset is the most poorly determined since its position on the fringe of the projection leads to a relatively low number of rays per bin and precludes a significant number of crossing rays.

Consequently, we use zero boundary conditions, which are implemented by expanding both the travel time and amplitude grids by a few grid points and smoothly tapering each to zero at the grid edges.

The solution to equation (1) is obtained through a numerical solution to Poisson's equation (Sweet, 1974; Swartztrauber and Sweet, 1975) on a rectangular grid. In order to satisfy this constraint, data-poor rows and columns were trimmed from the edges of the projections and the grid was expanded 2-4 points to implement the zero boundary conditions (Fig. 7a). Values were then interpolated at the grid points corresponding to bins with no data (Fig. 7b).

A spatial filter was applied to both the amplitudes and travel times. The grids were transformed using a 2-dimensional FFT, and the higher wavenumber components were removed (Fig. 7c). The travel time surface was heavily filtered for two reasons. Firstly, the short-wavelength components are less reliable than the long-wavelength components due to station effects and measurement uncertainty, and are less stable with respect to the bin-averaging procedure. Secondly, the double integration of the amplitudes in solving equation (1) produces perforce a very smooth travel time surface, meaning that the amplitudes cannot resolve short-wavelength features. Consequently, the amplitudes were only slightly filtered to remove short-wavelength noise before solving the equation. The spatial filter allows a comparison between features of similar scale length between the travel time and amplitude-derived time delay surfaces. The comparison criterion is a cross-correlation coefficient of the filtered travel time model with the amplitude-derived time delay model at the grid points whose corresponding bins contained data.

Models derived from amplitude variations

The results for the thin lens models which had the best match of amplitude-predicted time delays and observed time delays are shown in Fig. 8a. The depth for

these models is 160 km, and a correlation coefficient of 0.48 was obtained. The models appear most similar in the area of fast travel times trending northeast. This is also the area of the projection surface with the most data, and consequently the most robust features. If the observed and predicted travel time surfaces are filtered more in order to compare the long-wavelength features, the correlation coefficient increases to 0.79 (Fig. 8b). The amplitude of the variation in the two models is also comparable. The high correlation in the long-wavelength components of predicted and observed travel times is a strong indication that most of the robust amplitude variation arises from elastic focussing-defocussing. The correlation coefficient peaks at 160 km, but decreases slowly with increasing depth. This is because the back-projections change slowly as the source array appears more like a point source. However, at depths below 160 km, the amplitudes predict a much larger range in travel time variation than indicated by the observed time delay surface. Therefore, we choose 160 km as the optimal projection depth.

The same procedure can be applied to the results of the deviations from the subsite station means. For Pahute Mesa, the best correlation of predicted to observed travel times is at a depth of 25 km, which also had the most coherent images for the amplitude scatter (Fig. 6). These correlate at a level of 0.43, while the very-long-wavelength component correlates at a 0.71 level (Fig. 9). However, the predicted range in travel times is only 0.05 s for the very-long-wavelength component, whereas the observed range is 0.20 s. This probably indicates that a single thin lens cannot predict both the amplitudes and travel times in this case, but rather a continuous distribution of velocity heterogeneity is needed to accumulate the appropriate travel time anomalies.

Nevertheless, it is instructive to see how far a discontinuity derived from the lens can go in producing the observed trends in amplitudes across the mesa. The same procedure was attempted for Yucca Flat, but the predicted travel time variations were vanishingly small due to the failure of the back-projections to form coherent images.

The three-dimensionally varying velocity model is derived by simply mapping the time delay surface into vertical deflections of a velocity discontinuity, using the equation

$$z(x,y) = \Delta t / (1/\alpha_2 - 1/\alpha_1), \quad (2)$$

where α_1 and α_2 are the P wave velocities above and below the velocity discontinuity, respectively. The velocities used for the 160 km deep case are 7.70 km/s and 8.25 km/s, chosen to correspond to the range of velocities in the low velocity zone of the T7 model. We model the shallow (25 km) case as a Conrad-type discontinuity with velocities of 6.4 km/s and 7 km/s. The resultant surfaces are shown in Fig. 10.

Both surfaces are characterized by broad central highs, engendered by the low amplitudes in the center of the projections, with deep flanking lows. The 160 km deep surface has a range of about 30 km, while the 25 km deep surface has a range of 8 km. The discontinuities hypothesized for the purposes of the model construction are the base of the low-velocity zone and the base of the upper crust. As it is quite plausible that such boundaries would be rather irregular, the topography derived herein seems physically reasonable.

CALCULATION OF KIRCHHOFF-HELMHOLTZ SYNTHETICS

Haddon and Buchen (1981) and Scott and Helmberger (1985) have presented developments of the three-dimensional Kirchhoff-Helmholtz integral formulation for the transmitted case. The equation for a transmitted potential across a velocity discontinuity Σ is:

$$\varphi_2 = 1/(4\pi) \int_{\partial\Sigma} T \quad f'(t-r/\alpha_1+r_0/\alpha_2) (\cos\Theta_2 + \cos\Theta_1)/(r_0 r \alpha_2) \, dS,$$

where T is the acoustic plane wave transmission coefficient,

r_o is the source-surface element distance,

r is the surface element-receiver distance,

θ_1 is the angle between the surface and the refracted wavefront,

θ_2 is the angle between the surface-receiver vector and the normal to the surface,

and dS is an areal element (Fig. 11).

(This is modified from equation 13 in Scott and Helmberger, in which the second cosine term should be divided by α_2 , rather than α_1 .) The transmission coefficient is calculated for the local angle of incidence on the surface. If this angle exceeds the critical angle, the transmission coefficient is set equal to zero. A synthetic ramp response is calculated by simply summing step functions with the appropriate multipliers and time lags for each surface element. In order to obtain a teleseismic displacement seismogram, the resulting ramp response is numerically differentiated (Fig. 12), and convolved with the second derivative of an explosion source potential, a Futterman operator with t^* of 0.75, and a short-period WWSSN instrument response. The source used for these seismograms is a modified Haskell source (Helmberger and Hadley, 1981) with $b=1$ and $K=8$. A pP phase with a time lag of 0.9 s and reflection coefficient of -1 is also added, but does not affect the ab part of the waveform.

The seismograms are calculated for two welded half-spaces, using acoustic transmission coefficients. The receivers are located 20,000 km below the surface, corresponding to the geometric spreading at about 60° in the real earth, and at the appropriate x - y coordinates so that the intersection of the geometric ray with the flat surface coincides with the appropriate site in the back-projections. Synthetic seismograms are also computed for the flat-layer case. The ab amplitudes are calculated for the model synthetics and divided by the ab amplitudes for the flat-layer synthetics. In all, the computation of the synthetics is fairly easy and quick, facilitating the testing of a large number of different models for many source-station pairs.

Synthetic tests of models

For the 160 km deep discontinuity, synthetic seismograms were calculated for 56 teleseismic stations from sources in the center of the Pahute Mesa and Yucca Flat sites. The differences in the Pahute Mesa and Yucca Flat log amplitudes are shown for each station in Fig. 13, along with the differences in the observed Pahute Mesa and Yucca Flat station mean magnitudes ($_{PM}S_i - _{YF}S_i$). The patterns are strikingly similar, differing only in strength. Even fairly subtle details in the observed pattern are matched in the synthetics, such as the trend in the closer stations from relatively low magnitudes to the north for Pahute Mesa relative to Yucca Flat, to high magnitudes in the NNE, low magnitudes in the NE, and high magnitudes in the ENE and east. Thus, the imaging of three-dimensionally varying structure from the amplitude variations appears to be successful in predicting much of the amplitude behavior. Of course, it cannot be expected to match the full range of variation because the back-projection utilizes destructive interference to mask out anomalies that are not identified with that particular projection depth. Thus, the technique is intrinsically conservative.

The patterns of travel time residuals also are strikingly similar for both the synthetic and observed seismograms (Fig. 14). Again, the range of variation is not matched by the model, due to the conservative nature of the procedure. Nevertheless, it is encouraging that the model derived from amplitude variations qualitatively predicts the observed travel time variations as well. This agreement also indicates that the choice of zero boundary conditions in the wavefront curvature equation does not introduce any significant artifacts.

The Kirchhoff-Helmholtz synthetics for the shallow model are somewhat more difficult to construct. Because of the shallow depth and short scale lengths of the model, the local angle of incidence exceeds the critical angle for part of the surface (Fig.

15a) for many of the source-station geometries. In fact, this effect is a primary contributor to the variations in waveform and amplitude for the different structures tested by Scott and Helmberger (1985). For the model tested here, the masking effect is particularly prevalent on the steep transition from the high to the low on the surface. Since such surface elements are assigned a transmission coefficient of zero in the computation of the seismograms, this results in a somewhat artificial truncation effect in the very early part of the waveform (Fig. 15b). These truncation effects can produce large variations in the ab amplitudes. In order to assess the general magnitude of these effects, the synthetics were recomputed by assigning supercritical elements the amplitude factor of adjacent elements. This has the effect of generally smoothing out the effect of the truncation (Fig. 15c). Stations for which the ab amplitudes changed significantly, which were primarily the stations to the west such as MAT, were excluded from the analysis. However, the actual ab amplitudes used herein are those calculated by masking out critical and supercritical elements.

The variation of log amplitude with position in the test site for three stations are shown in Fig. 16. Since the corresponding variations in observed m_b values are highly contaminated by incoherent measurement errors, the deviations from the station means for nearby stations were averaged in for each explosion for the comparison (Fig. 16). As with the deep model, the synthetic log amplitudes have the correct sense of variation, but underpredict the amplitudes. However, this qualitative correlation is quite important, because it implies that the "scatter" about the station means can in fact be partially interpreted in a deterministic framework. This is supported by the coherent variations of observed m_b deviations within the mesa for each group of stations.

DISCUSSION

It is interesting to compare the models derived from amplitudes in this study with those derived from travel times. A vertical cross-section through the Minster *et al.* (1981) and Taylor (1983) structures of NTS is shown in Fig. 17, with cross-sections of the two velocity discontinuity models derived from amplitudes superimposed. The two travel time structures are reasonably similar, although the Taylor (1983) structure terminates more shallowly and has much larger velocity variations. The amplitude-derived structure at 25 km is qualitatively similar to both, with an upwarp in the high-velocity material closely corresponding to fast velocity regions in both travel time models. The deep amplitude model is more difficult to compare since it is located deeper than either of the travel time model parameterizations. However, if the high-velocity regions in the travel time models are extended down along the raypaths to the stations to the NNE, they would intersect an upwarp of the high-velocity material.

The comparison is complicated by the dichotomy of velocity boundary undulation models, which concentrate velocity heterogeneity over a small depth range, and continuous block models, which have a tendency to smear the heterogeneity along the dominant raypaths. The relative ability of each class of model to produce amplitude variations for a given set of travel time perturbations is contingent on whether log amplitudes accumulate linearly along the raypath. Haddon and Husebye (1978) computed amplitude anomalies for a 150 km deep thin lens, and a 100 km thick lens models under NORSAR that produces the same propagation times for vertical incidence. The patterns were nearly identical, suggesting log-linear accumulation of amplitude anomalies. However, as noted above, the model of Taylor (1983) for NTS produces much larger variations than the 152 km thick model of Minster *et al.* (1981), despite the fact that they satisfy similar travel time residual data sets. Thus, it seems that a log-linear accumulation model for amplitudes may be valid at depth, but may break down near the source. Indeed, this may explain why the thin lens amplitude model at 25 km depth grossly underpredicted the range of travel time variation. Specifically, if the

heterogeneity is concentrated over a small depth range near the source, a much smaller heterogeneity is necessary to produce a given amplitude range.

One shortcoming of the procedure used in this study for deriving three-dimensionally varying models from amplitudes appears to be a systematic underprediction of the range in amplitude variations. This is a common problem in attempts to predict amplitudes in an elastic framework. As noted earlier, the structures derived from travel times by Thomson and Gubbins (1982) for NORSAR and by Minster *et al.* (1981) for NTS both underpredict amplitude variations to a varying degree. The structure derived by Taylor (1983) for NTS does predict amplitude variations of the same order as the data (Cormier, 1987), but this is the result of very large velocity differences over short distances, ranging from 16% over 14 km in the shallowest layer to 5% over 20 km in the deepest layer.

In theory, a structure derived from the amplitudes should be better able to predict the range of amplitude variation. Thomson's (1983) models for NORSAR derived using a ray-theoretical amplitude inversion predict the observed amplitude variation better than the travel time model A2 (Thomson and Gubbins, 1982), even though the latter model has stronger velocity variations. For the case of the procedure presented in this paper, the main factor contributing to the underprediction of the amplitudes seems to be the parameterization of only a single surface for a given model. The destructive interference in the back-projections ensures that only part of the available information in the amplitudes is being utilized. We have attempted to circumvent this by examining both the regionally demeaned anomalies (for the deep models) and the deviations from the individual station means (for the shallow models). However, it may be possible to simultaneously back-project anomalies to two or more surfaces, i.e., tomographically image the amplitude data. This should retain more of the amplitude information, resulting in more accurate models.

It should also be noted that we have attempted to explain only the intrasite and intersite differences. However, it is apparent from the similarity of the Yucca Flat and Pahute Mesa azimuthal patterns that the two subsites share a large common component in both amplitude and travel time variations (Fig. 2), with low magnitudes and fast travel times to the northeast. This component is as much as 0.2 units for the magnitudes and 1.0 s for the travel times. The relatively small ratio of amplitude to travel time anomaly indicates very broad scale lengths, and this, coupled with the fact that both subsites must be affected similarly, indicates a deep (>400 km) source for the common patterns.

CONCLUSIONS

We have used a combination of thin lens projections, calculation of time delays from amplitudes using the wavefront curvature equation, and mapping time delays into a warped velocity discontinuity to image three-dimensionally varying structure from amplitude data. Synthetic seismograms can be easily computed for these discontinuities using the Kirchhoff-Helmholtz technique. A comparison of observed and synthetic magnitude anomalies indicates that the coherent intersite and intrasite differences in magnitudes from NTS explosions can be partially explained by warped velocity discontinuities 25 km and 160 km beneath the source array.

ACKNOWLEDGEMENTS

This research was supported by the Sloan Foundation, a Shell Faculty Career Initiation Grant, and the Defense Advanced Research Projects Agency, and was monitored by the Air Force Geophysics Laboratory under Contract F19628-87-K-0010.

- Scott, P. and Helmberger, D. V., 1985. Applications of the transmitted Kirchhoff-Helmholtz method to transmitted body wave and possible structural effects at NTS, *Bull. Seism. Soc. Am.*, **75**, 131-156.
- Spence, W., 1974. *P* wave residual differences and inferences on an upper mantle source for the Silent Canyon volcanic center, Southern Great Basin, Nevada, *Geophys. J. R. Astr. Soc.*, **38**, 505-523.
- Swartztrauber, P. N. and Sweet, R. A., 1975. Efficient FORTRAN subprograms for the solution of elliptic partial differential equations, *NCAR Technical Note NCAR-TN/IA-109*.
- Sweet, R. A., 1974. A generalized cyclic reduction algorithm, *SIAM J. Numer. Anal.*, **11**, 506-520.
- Taylor, S. R., 1983. Three-dimensional crust and upper mantle structure at the Nevada Test Site, *J. Geophys. Res.*, **88**, 2220-2232.
- Thomson, C., 1983. Ray-theoretical amplitude inversion for laterally varying velocity structure below NORSAR, *Geophys. J. R. Astr. Soc.*, **74**, 525-558.
- Thomson, C. J. and Gubbins, D., 1982. Three-dimensional lithospheric modelling at NORSAR: linearity of the method and amplitude variation from the anomalies, *Geophys. J. R. Astr. Soc.*, **71**, 1-36.

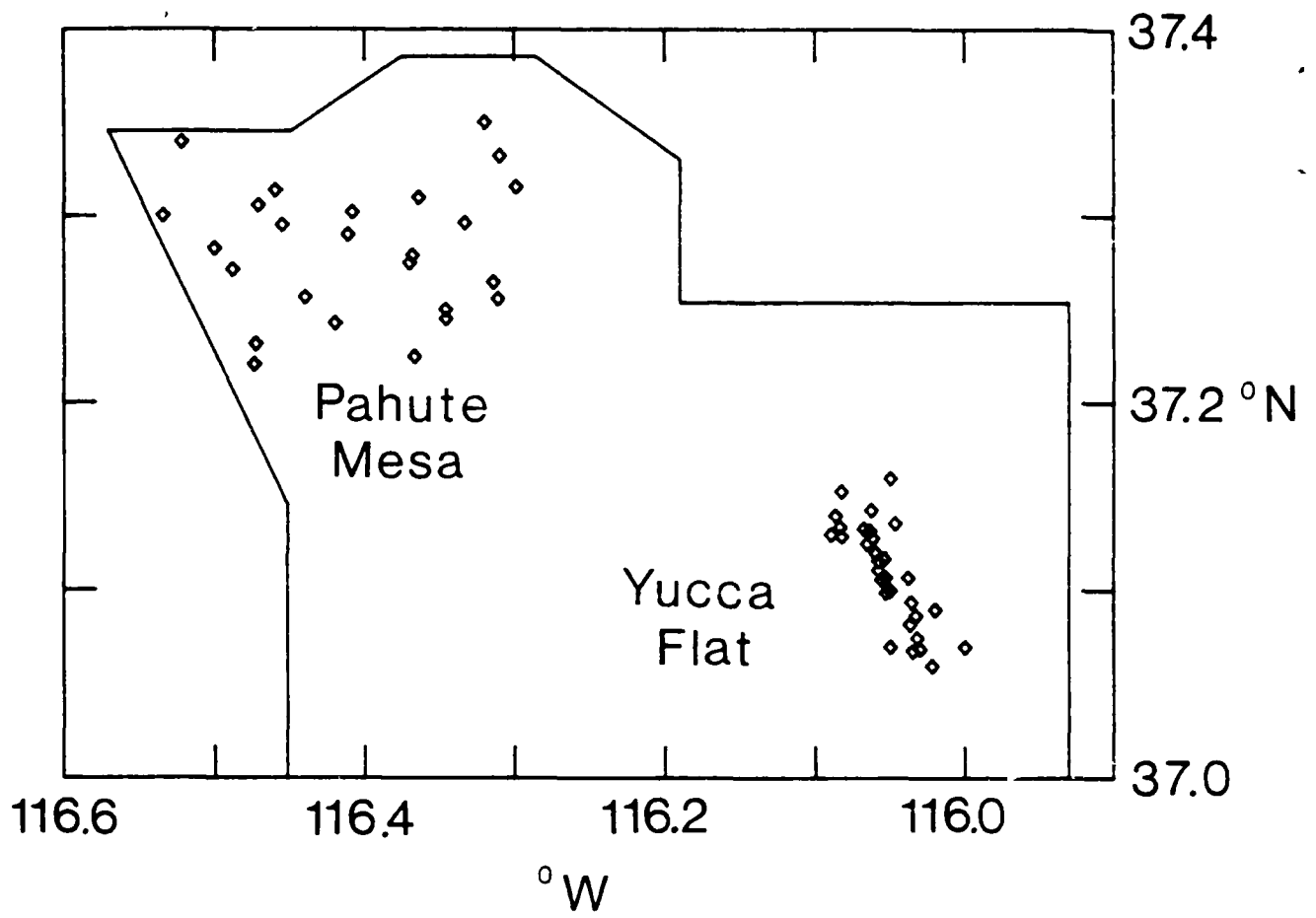


Fig. 1. Map of the Nevada Test Site source array.

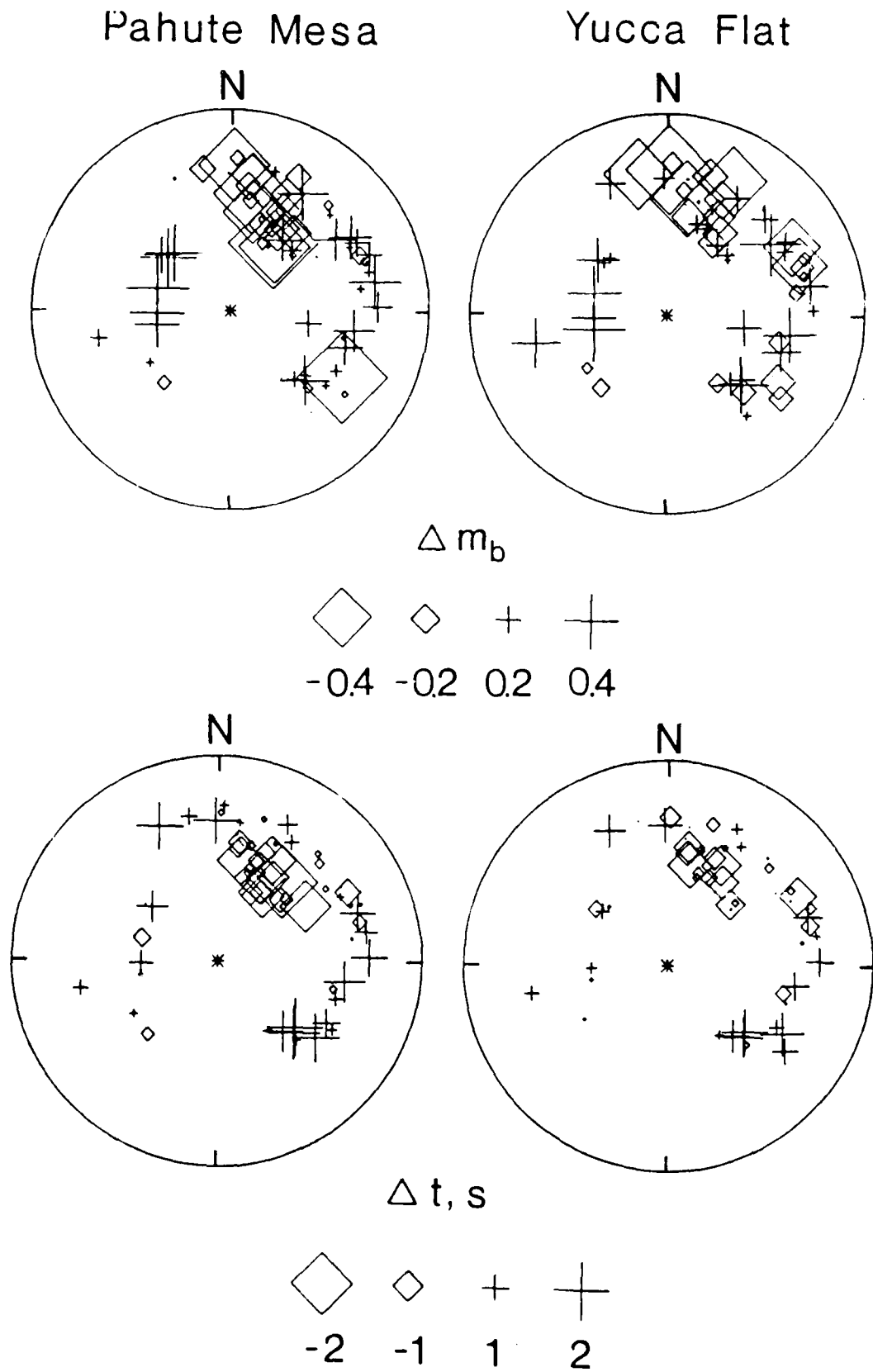


Fig. 2. Equal-area plots of station mean travel time and magnitude anomalies for the Pahute Mesa and Yucca Flat test sites. The rim corresponds to a takeoff angle of 22.5° in a velocity of 3.5 km/s.

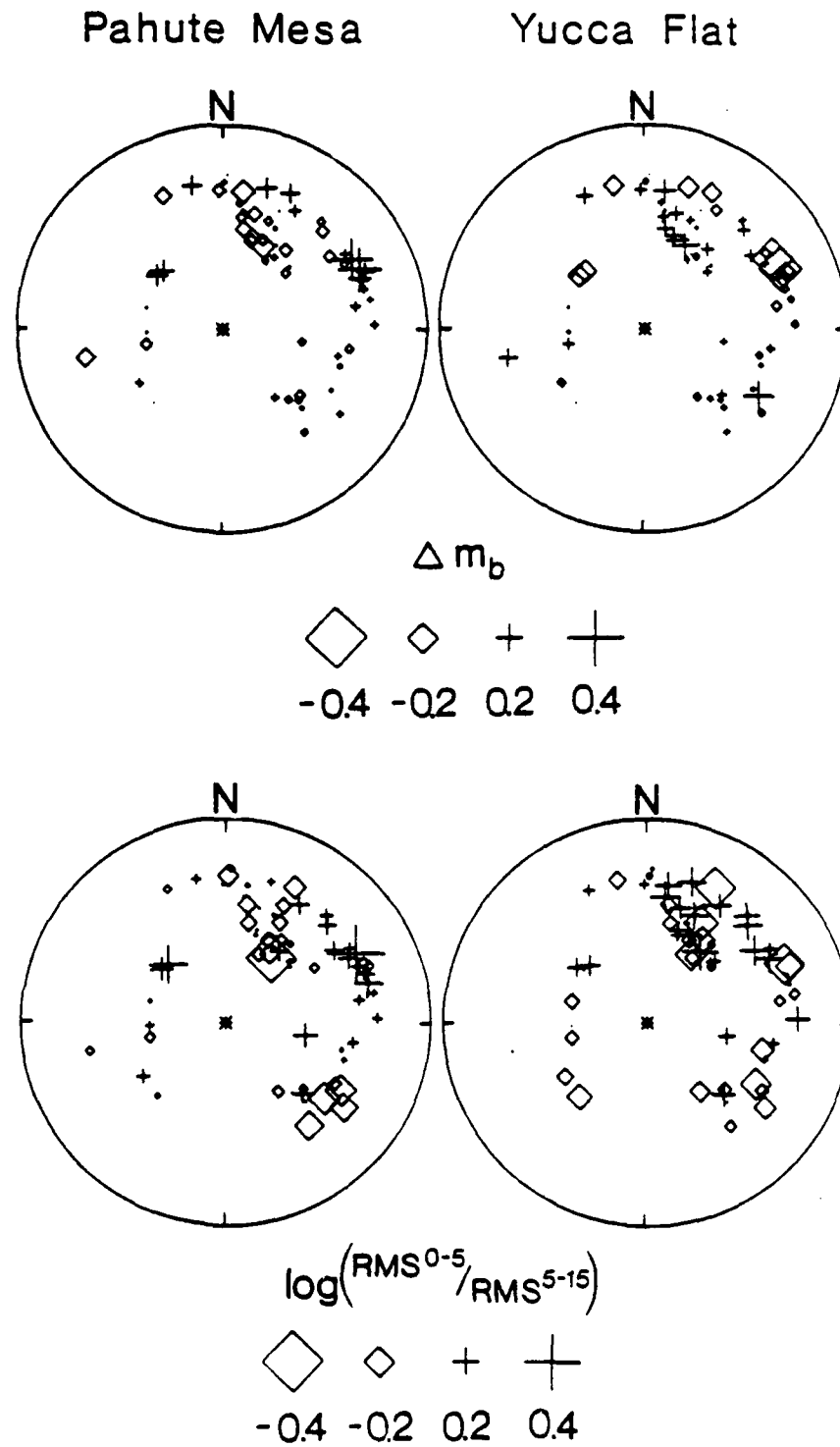


Fig. 3. Equal-area plots of station mean magnitude anomalies, with NTS station means removed, are plotted above station mean values of $\log(RMS^{0-5}/RMS^{5-15})$.

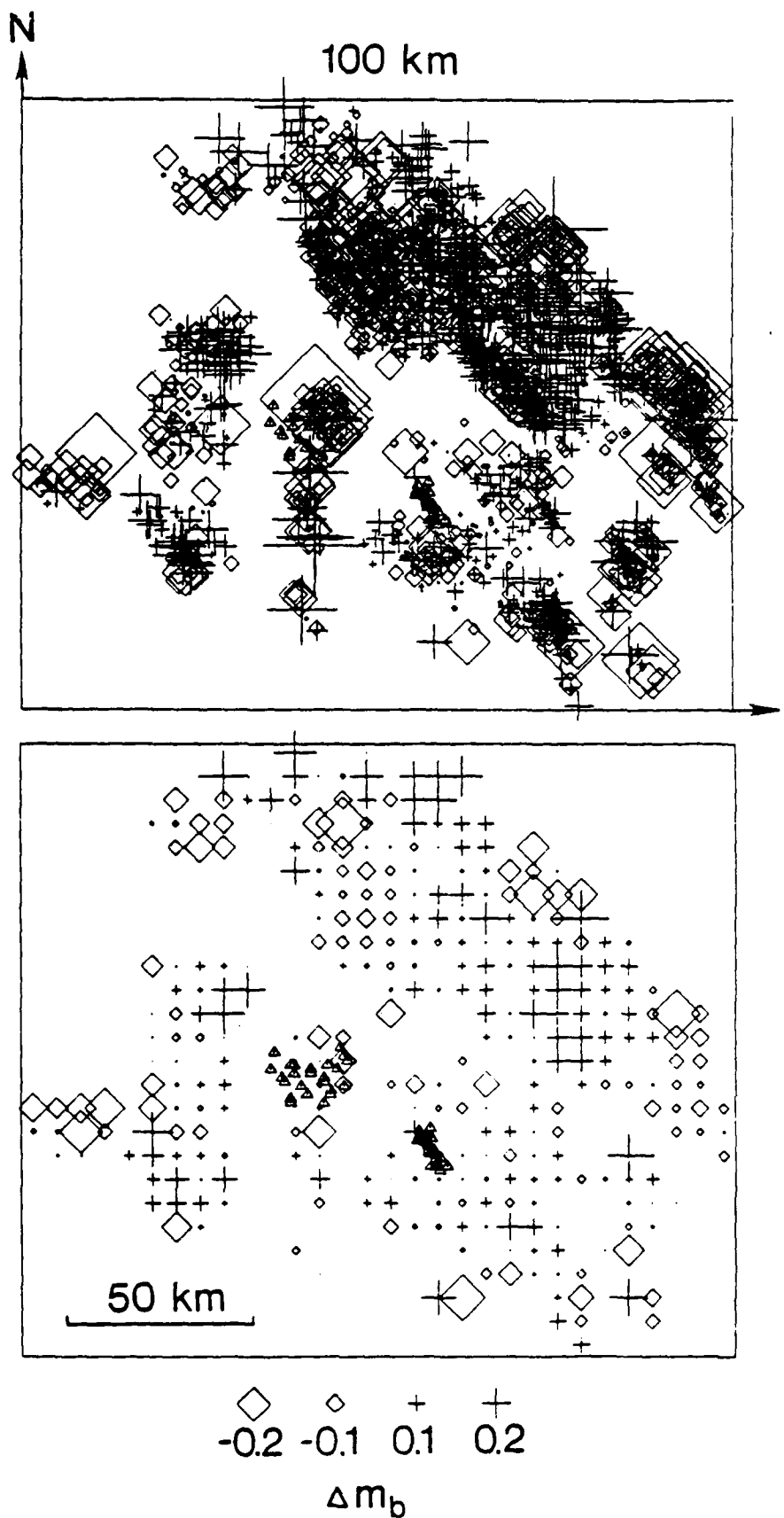


Fig. 4. Example of back-projection procedure. Magnitude anomalies, with NTS station means removed, are projected through laterally homogeneous structure to a depth of 100 km (a). The surface is gridded and the values in each grid square are averaged to provide a bin-averaged projection (b). The triangles indicate the positions of the sources.

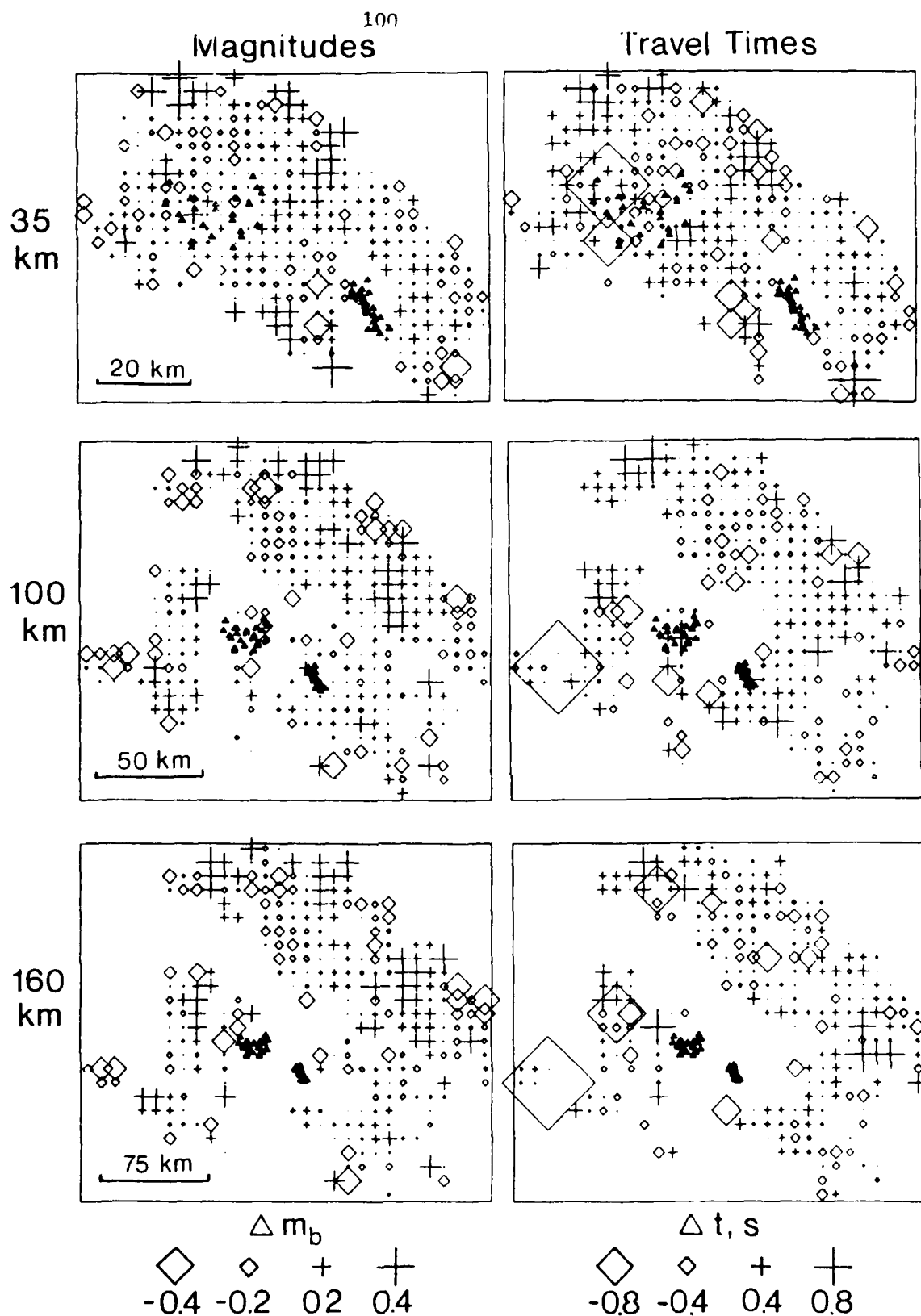


Fig. 5. Bin-averaged back-projections of magnitude and travel time anomalies with NTS station means removed to depths of 35 km, 100 km, and 160 km.

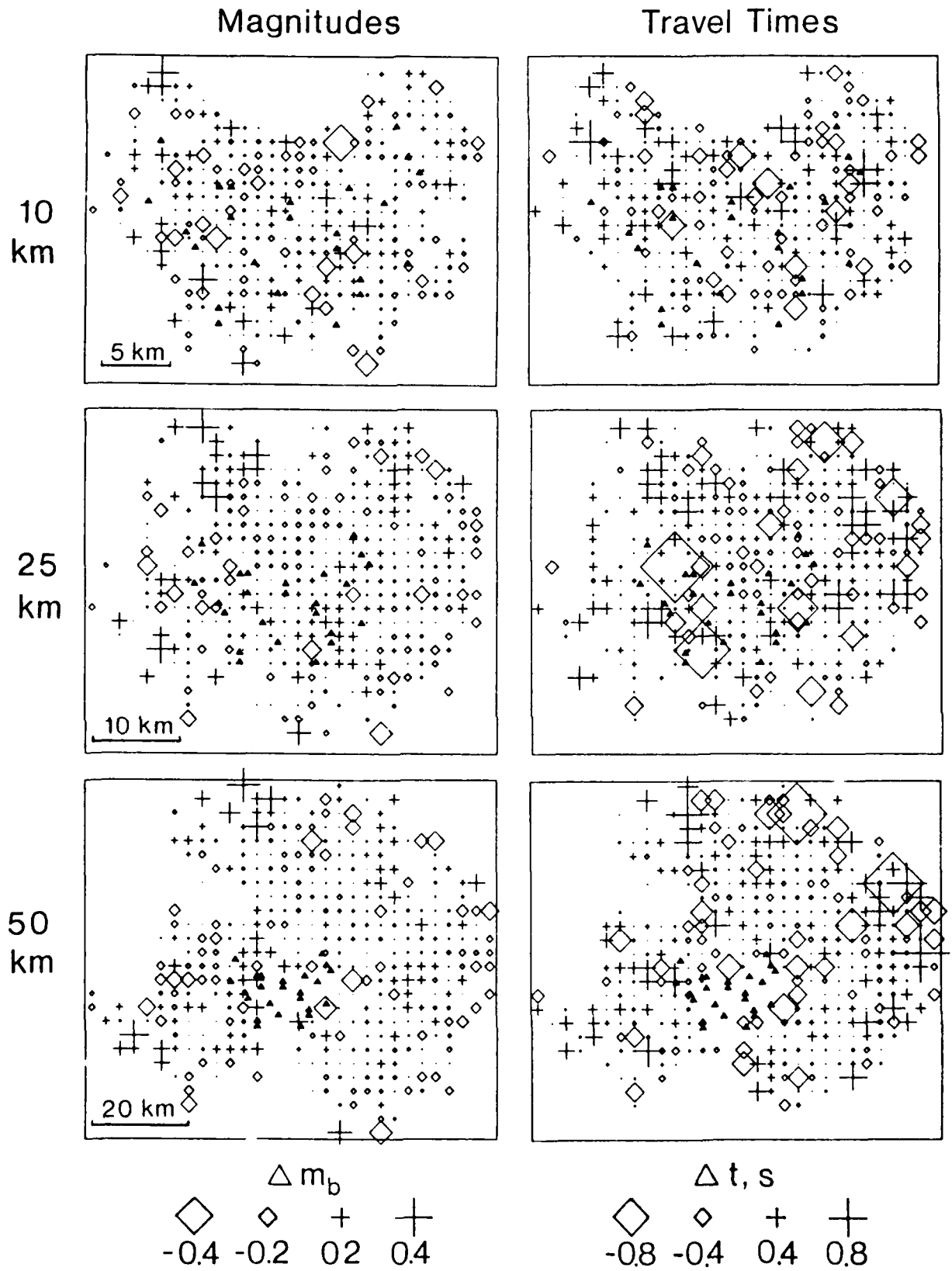


Fig. 6. Bin-averaged back-projections of deviations from individual station means for the Pahute Mesa test site at depths of 10 km, 25 km and 50 km. A coherent image of low values forms in both the magnitude and travel time projections at 25 km depth.

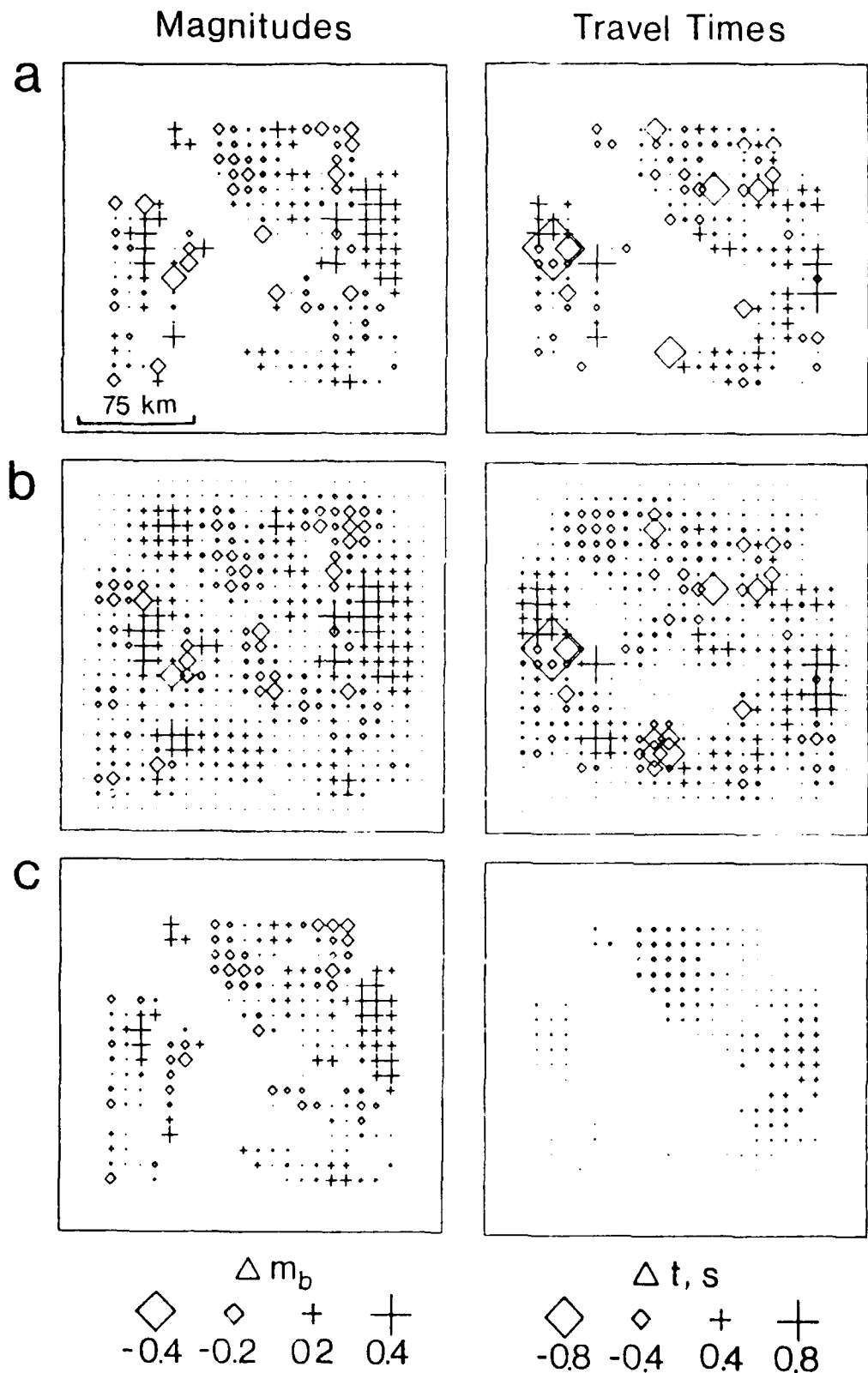


Fig. 7. Example of processing of bin-averaged surface to obtain a continuous, filtered, rectangular grid, for a depth of 160 km. The original grids are shown in Fig. 5 (bottom). The grid is cropped to remove data-poor columns and rows and expanded to allow the implementation of zero boundary conditions (a), interpolated to obtain a continuous rectangular grid (b), and filtered in doubly-transformed domain (c). The travel times are more heavily filtered than the amplitudes (see text). Only points which have data are shown in the last plot.

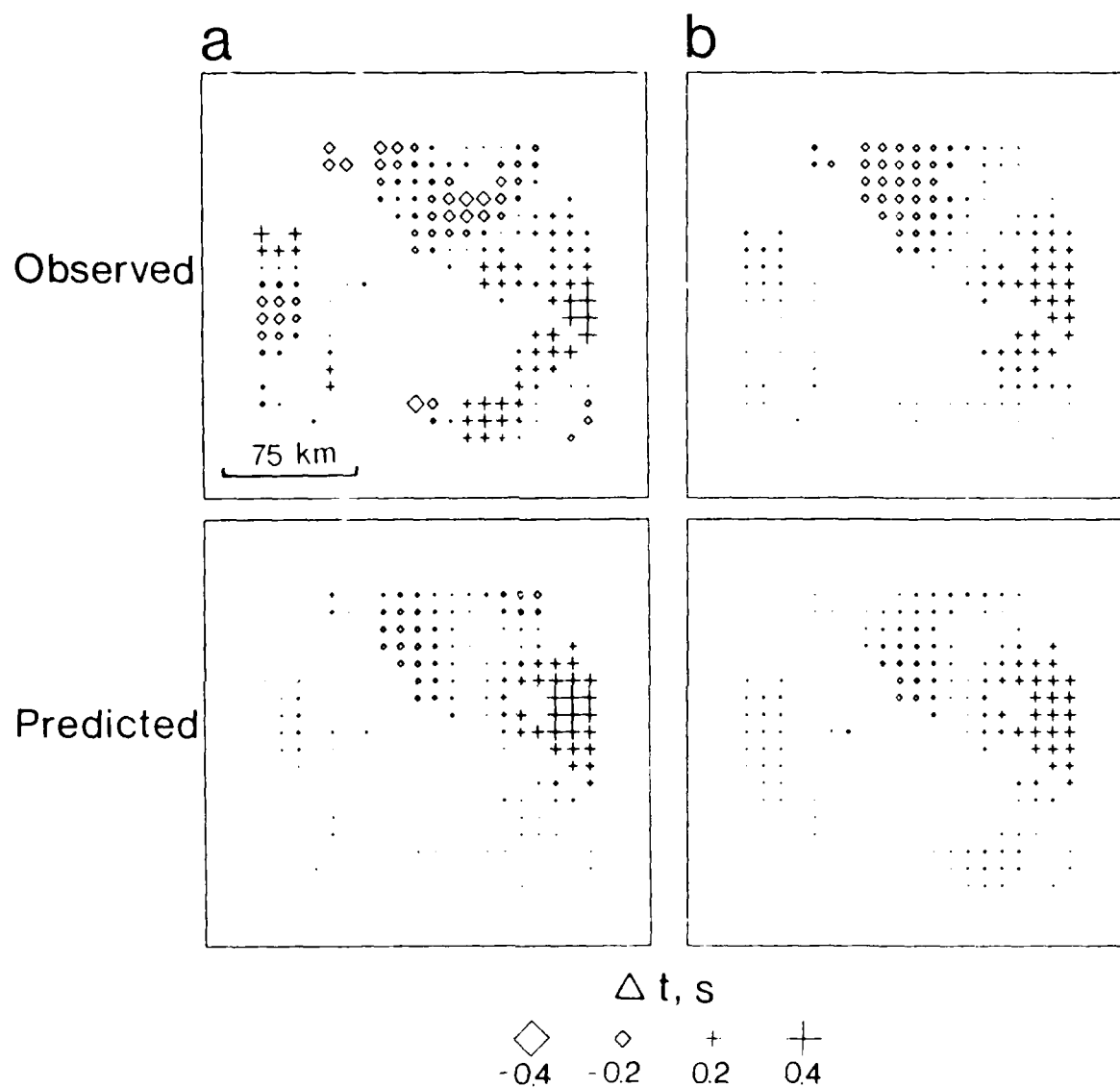


Fig. 8. Thin lens results for 160 km depth, filtered to retain long-wavelength (a) and very-long-wavelength (b) components. The top plot plots are the filtered, observed travel times, and the bottom are the filtered travel times predicted from the magnitude variations.

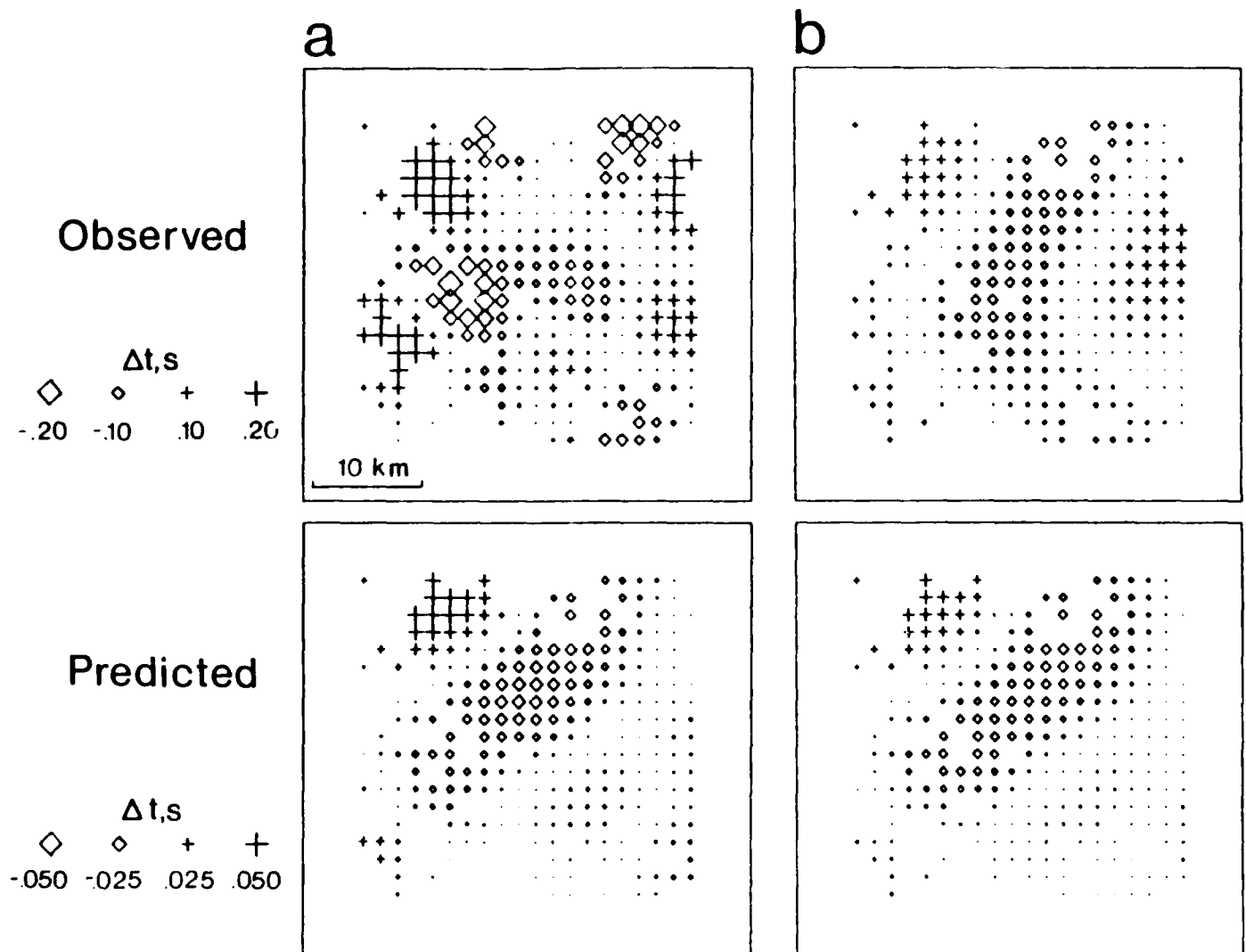


Fig. 9. Same as Fig. 8 for 25 km deep model. Note the difference in symbol scales for the observed and predicted plots.

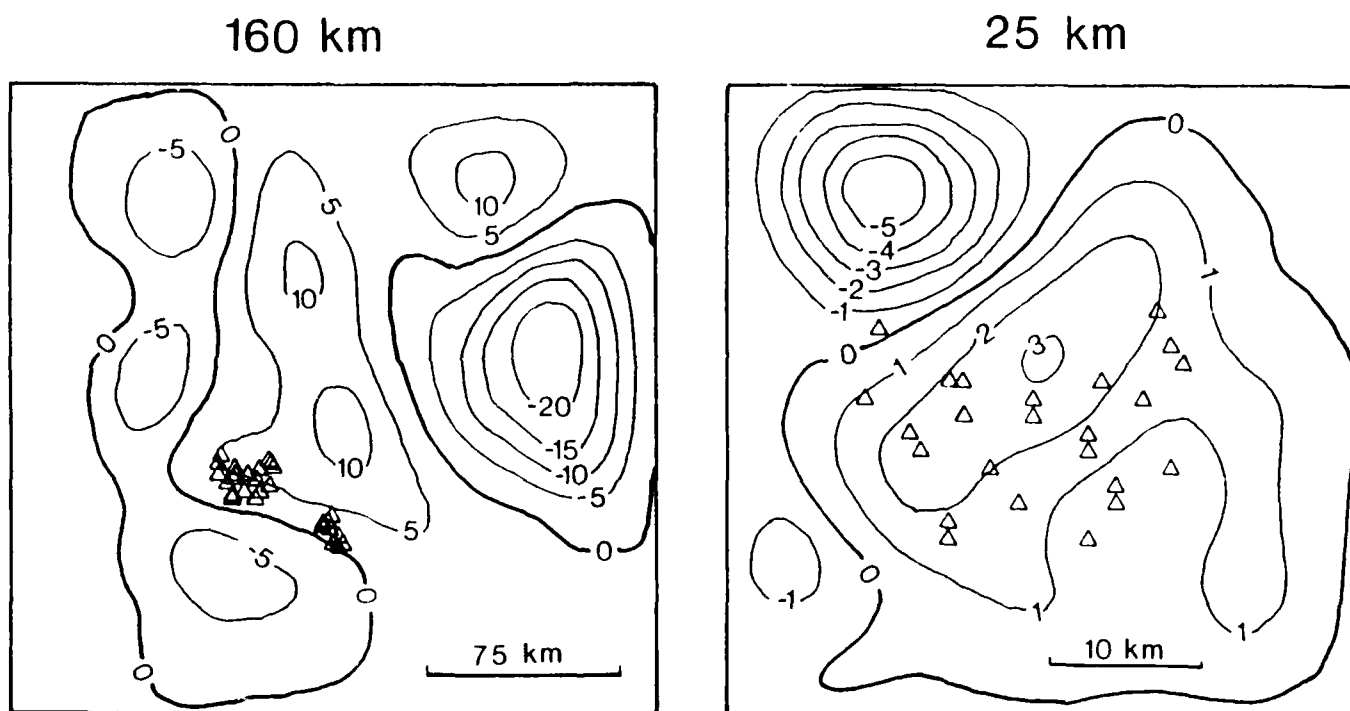


Fig. 10. Contour plots (in km) of the velocity discontinuity surfaces obtained from inversion of amplitudes. The deep (160 km) model obtained from intersite differences in magnitude patterns is shown on the left. The shallow (25 km) surface obtained from intrasite differences is shown on the right.

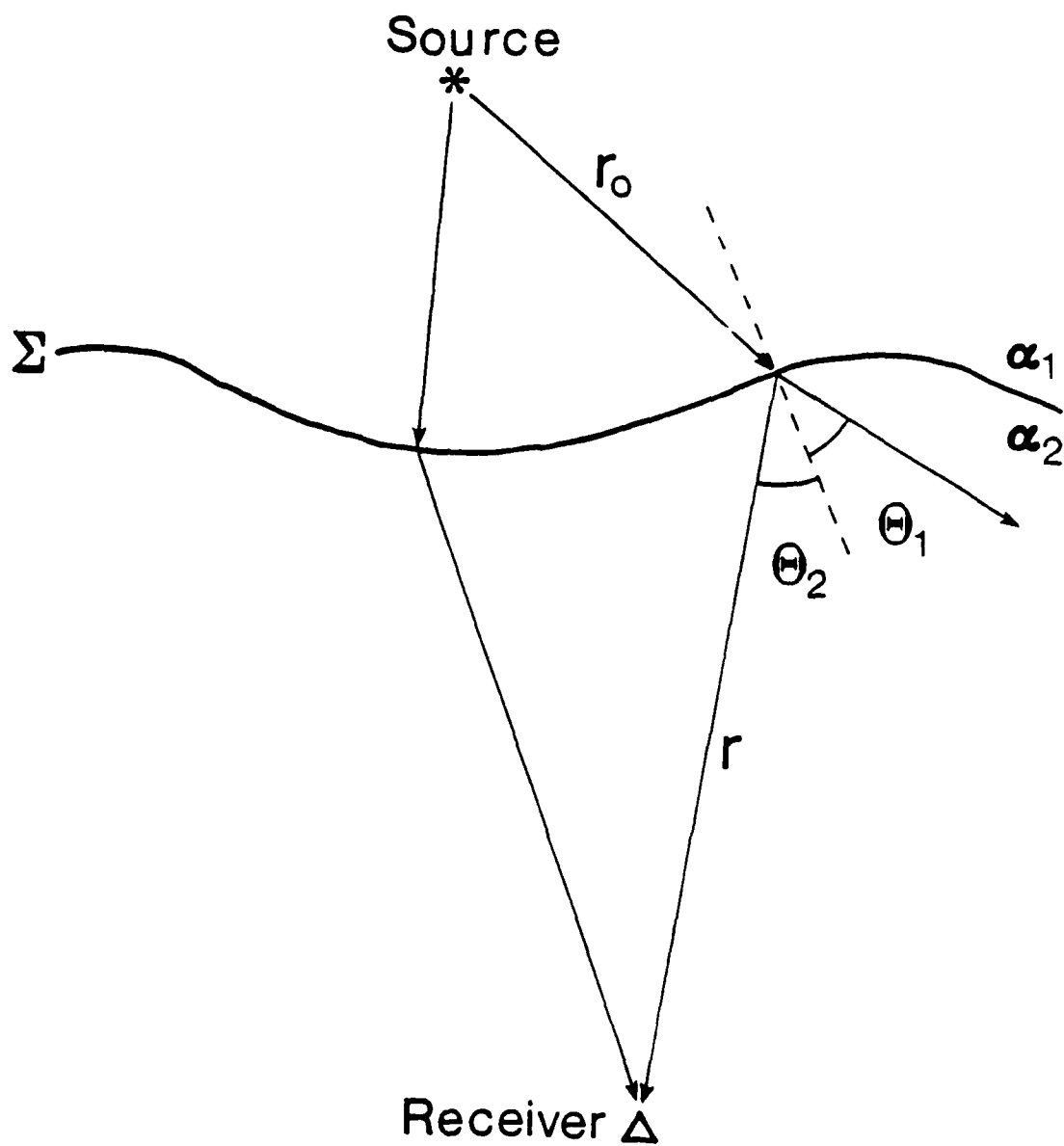


Fig. 11. Geometry of synthetic seismogram computation.

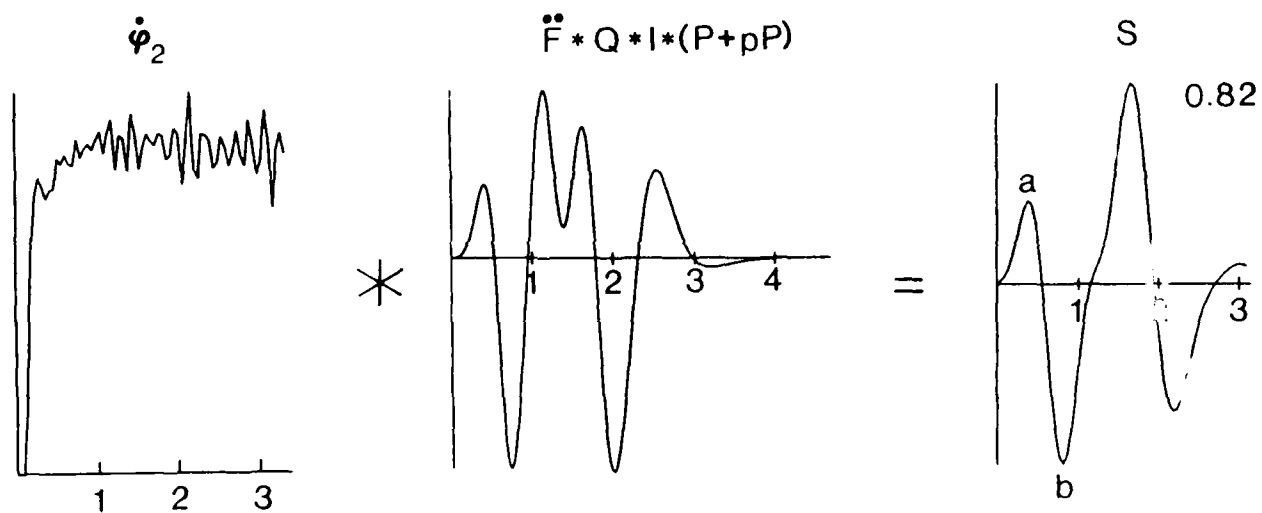


Fig. 12. Example of synthetic seismogram calculation. On the left is a step (differentiated ramp) response for Pahute Mesa to UME for the deep model. This is convolved with a function containing the source, instrument, free-surface and attenuation ($\tau^0=0.75$) responses (center). On the right is the final seismogram with the ab amplitude relative to the flat layer case indicated in the upper right.

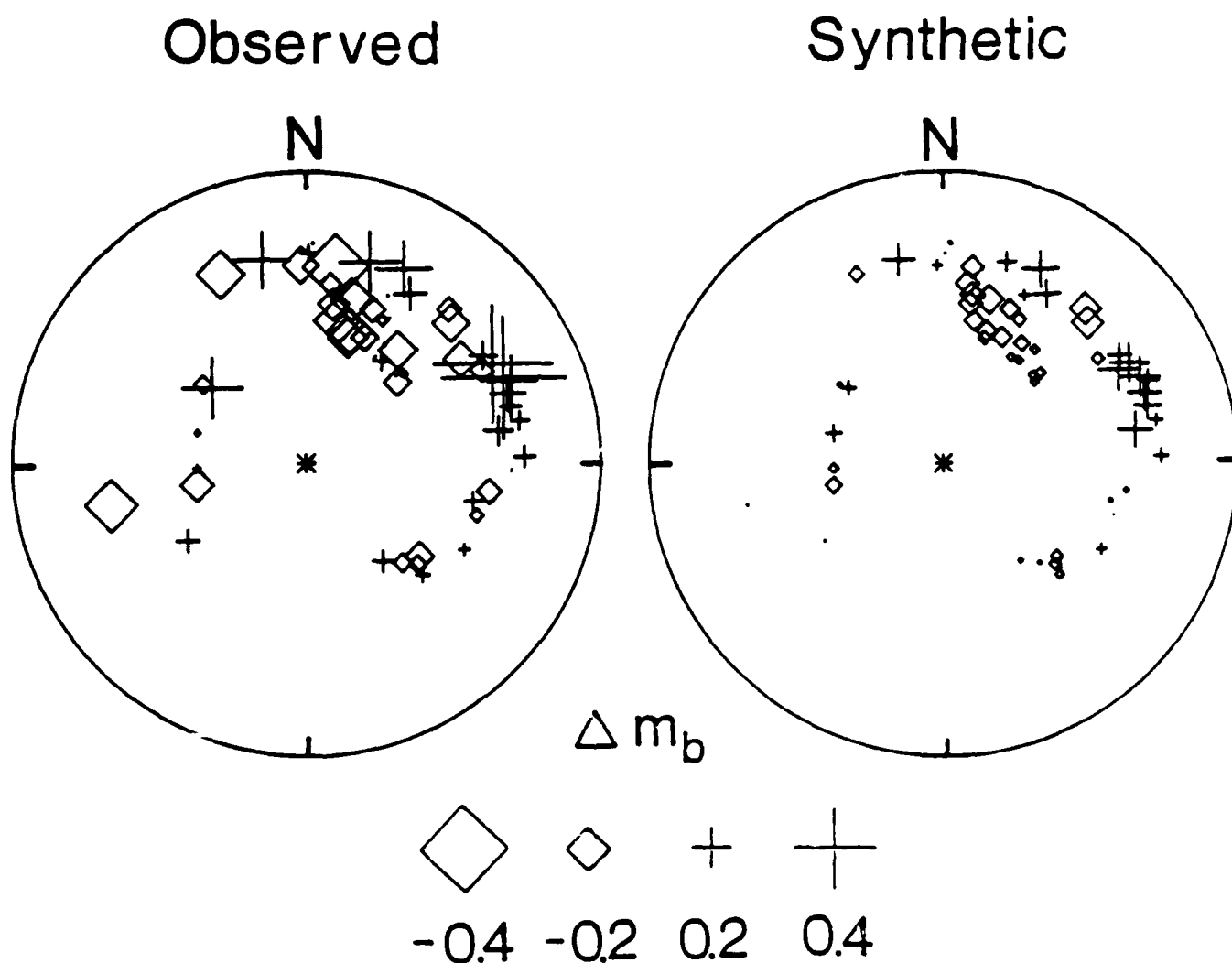


Fig. 13. Comparison of synthetic log amplitude variations with observed variations in m_b . The equal-area plot on the left shows the observed station average m_b values for Yucca Flat differenced from the corresponding station means for Pahute Mesa. The equal-area plot on the right shows synthetic log amplitude variations of Yucca Flat explosions differenced from those of Pahute Mesa.

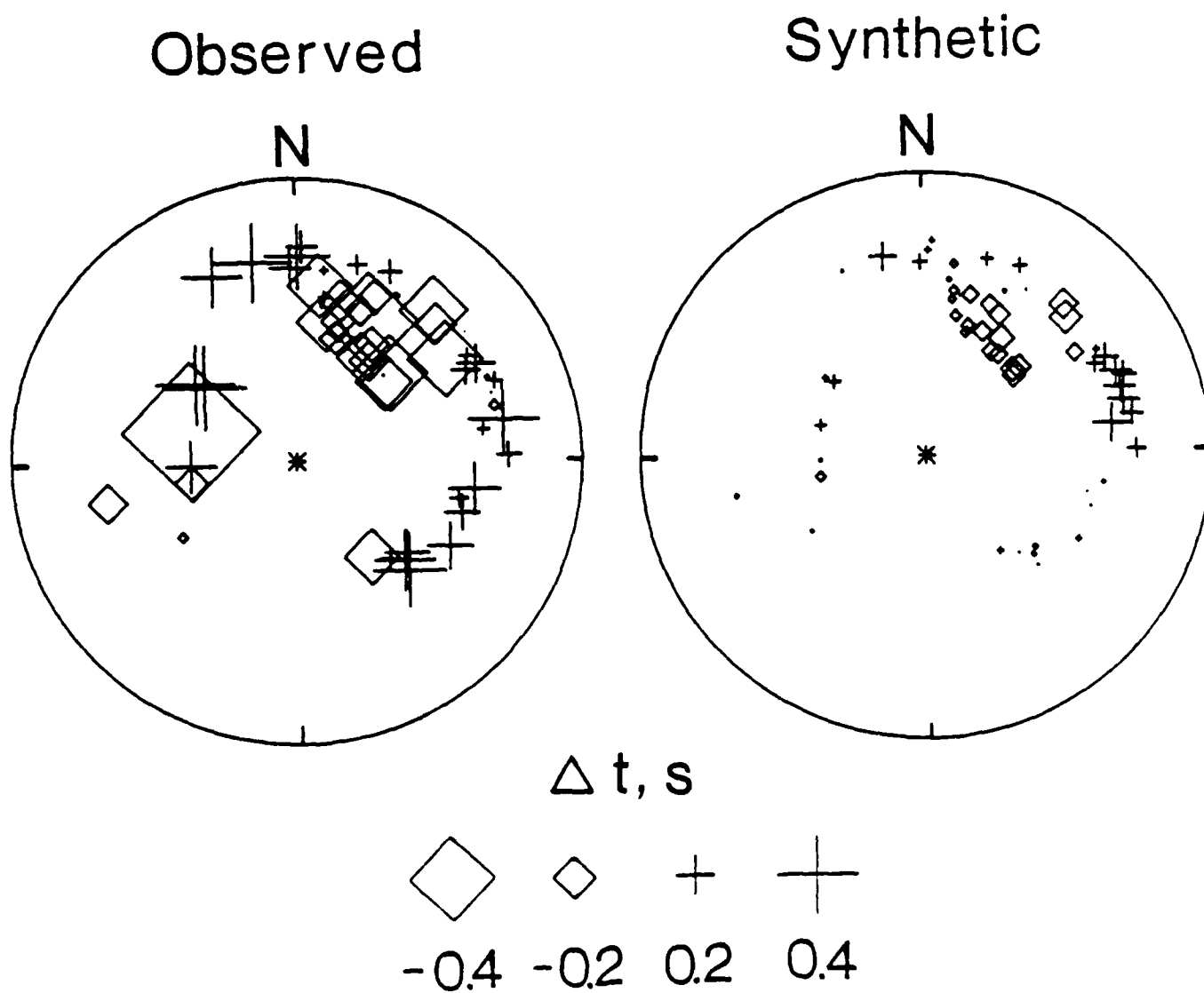


Fig. 14. Same as Fig. 12, for travel times.

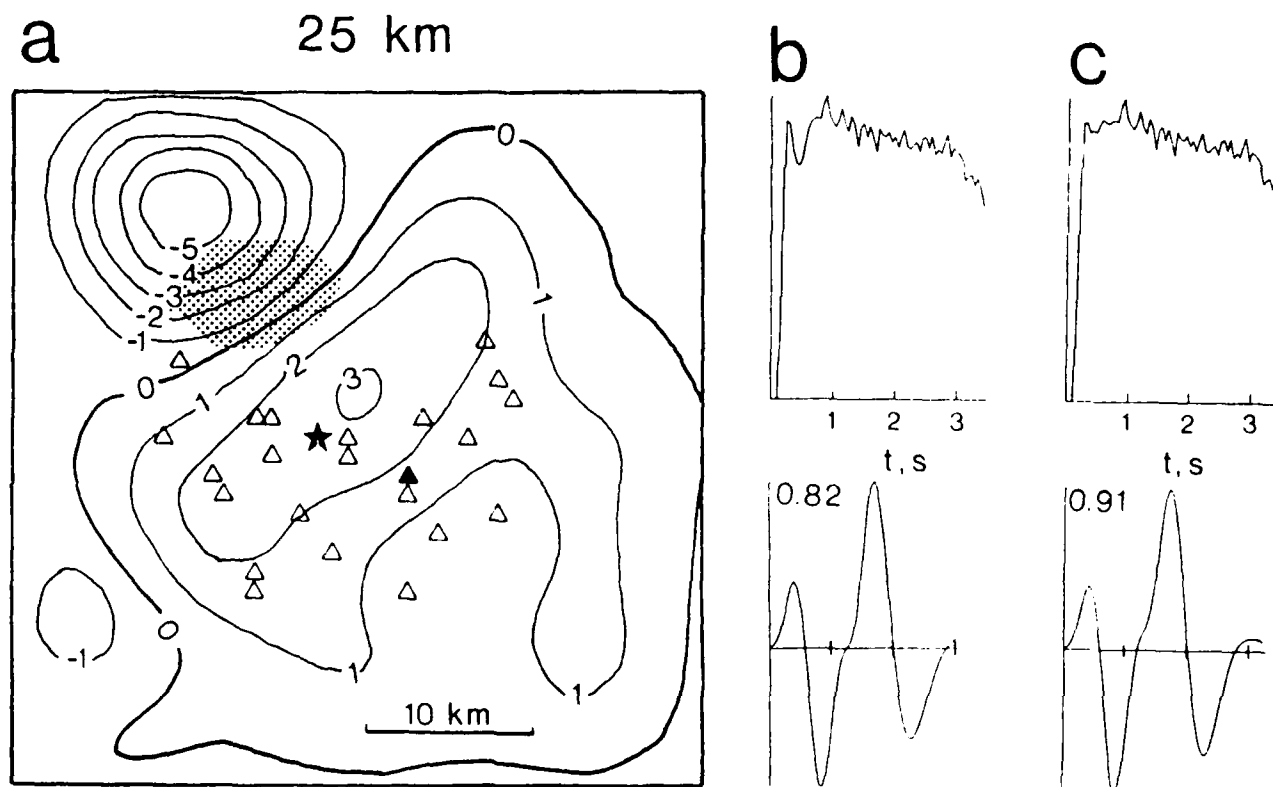


Fig. 15. The 25 km deep model is shown in (a), the stippled area indicating where the local angle of incidence exceeds the critical angle for the event CAMEMBER (filled triangle) to station MAT. The geometric arrival intersects the surface at the star. The "masked" portion of the surface leads to a truncation in the first second of the step response (b). This is smoothed out by assigning the masked elements the amplitude factors of adjacent elements (c) in order to evaluate the magnitude of this effect. The numbers in (b) and (c) indicate ab amplitudes relative to the flat-layer case.

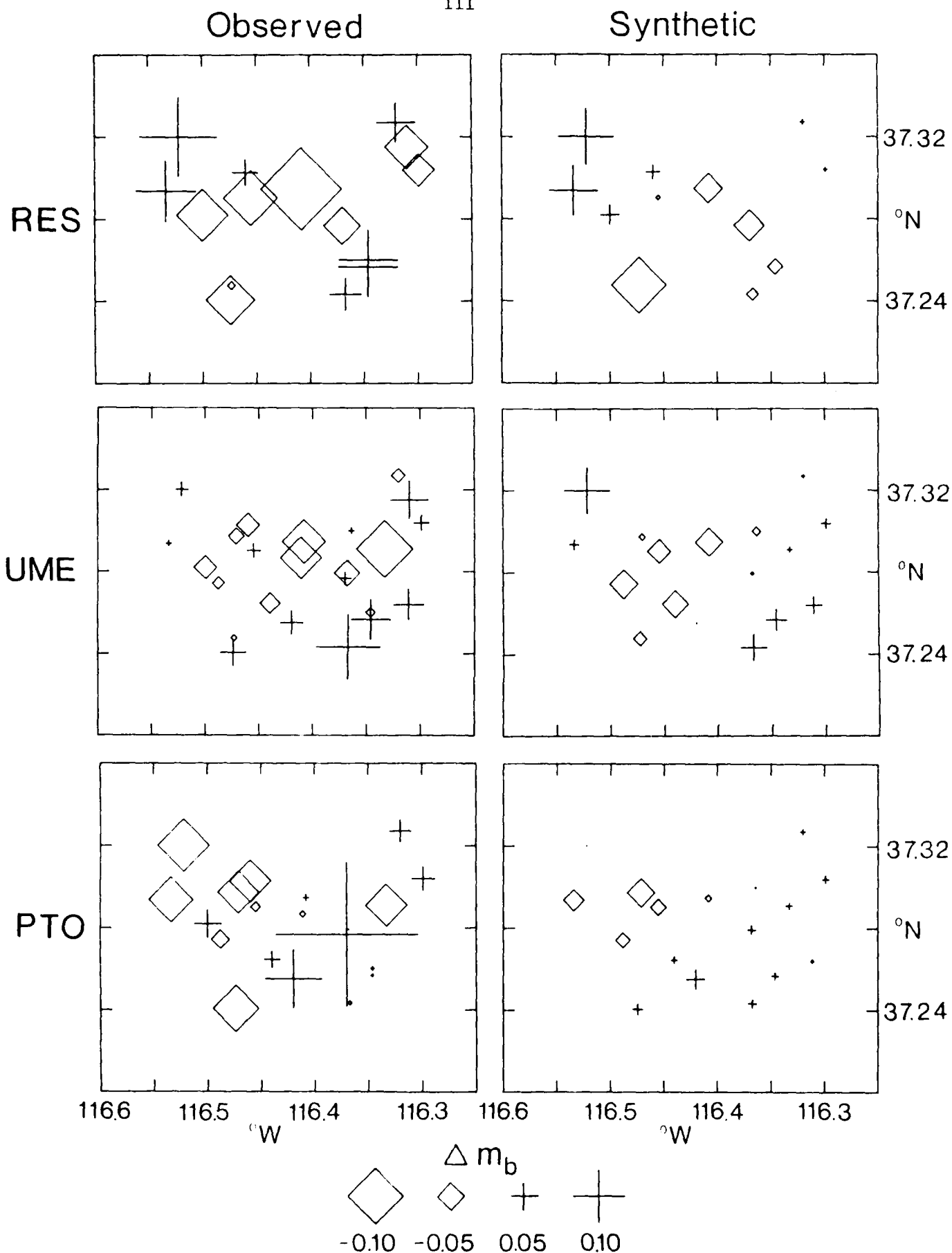


Fig. 16. (a) Variations in synthetic log amplitudes with position in Pahute Mesa, calculated for Resolute Bay, Canada (RES), Umea, Sweden (UME), and Porto, Portugal (PTO). (b) Observed variations in m_b , obtained by averaging nearby stations with those for which the synthetics were calculated.

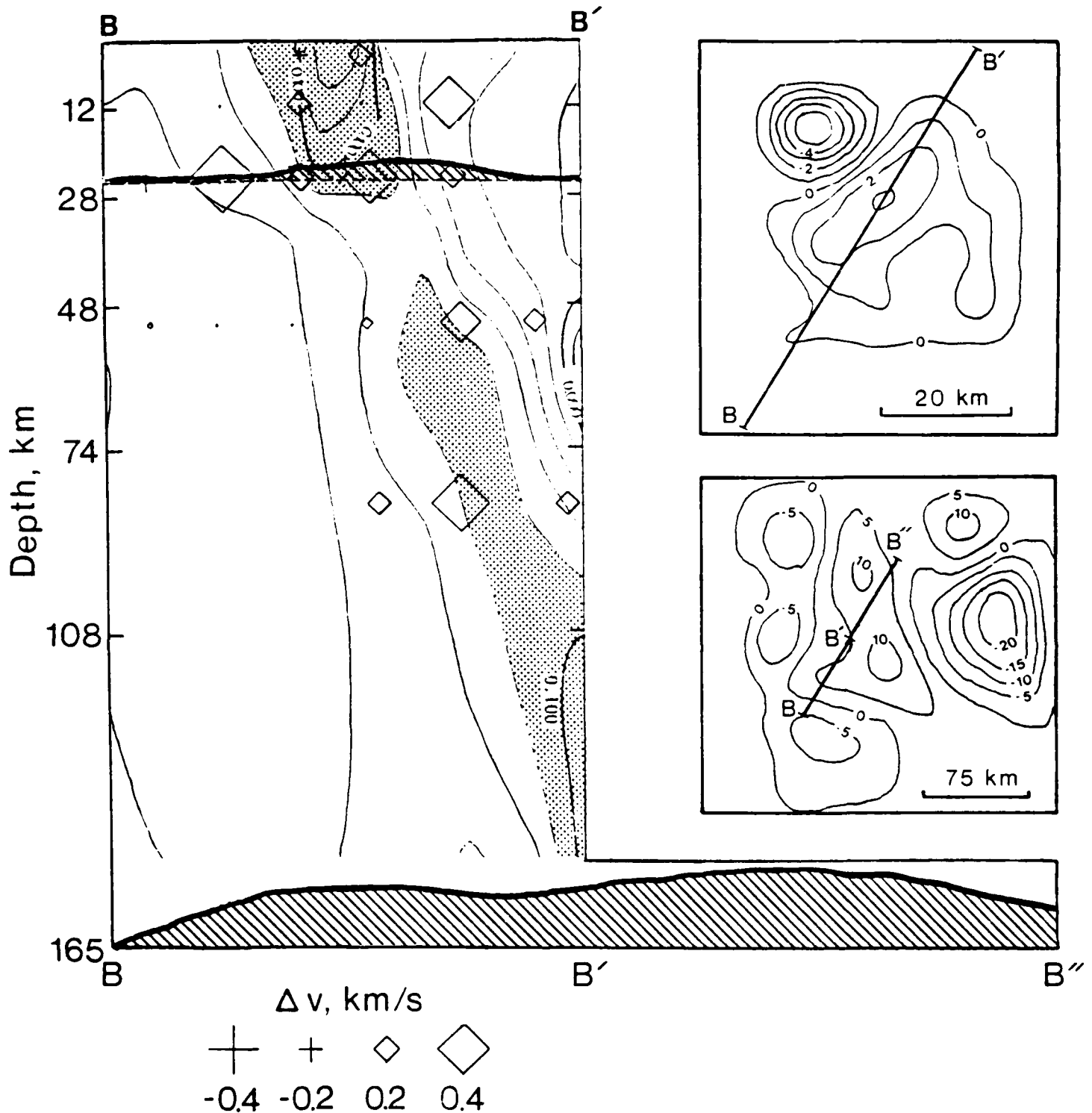


Fig. 17. Comparison of discontinuity models with block inversion models derived from travel times by other authors. The figure on the left is a modification of Fig. 4.13b of Minster *et al.* (1981), which is a vertical cross-section through their model, represented by the velocity contours. Symbols indicate the velocity perturbations in the blocks of Taylor's (1983) model that the cross-section intersects. The thick black lines are the equivalent cross-section through the shallow (25 km) velocity discontinuity model and an extended cross-section through the deep (160 km) model. The locations of the cross-sections are plotted on contour maps of the surfaces on the right. High velocity regions or extensions thereof in the block travel time models correspond to upwarps of high velocity material in the amplitude-derived discontinuity models.

CONTRACTORS (United States)

Professor Keiiti Aki
Center for Earth Sciences
University of Southern California
University Park
Los Angeles, CA 90089-0741

Professor Charles B. Archambeau
Cooperative Institute for Resch
in Environmental Sciences
University of Colorado
Boulder, CO 80309

Dr. Thomas C. Bache Jr.
Science Applications Int'l Corp.
10210 Campus Point Drive
San Diego, CA 92121 (2 copies)

Dr. Douglas R. Baumgardt
Signal Analysis & Systems Div.
ENSCO, Inc.
5400 Port Royal Road
Springfield, VA 22151-2388

Dr. Jonathan Berger
Institute of Geophysics and
Planetary Physics
Scripps Institution of Oceanography
A-025
University of California, San Diego
La Jolla, CA 92093

Dr. S. Bratt
Science Applications Int'l Corp.
10210 Campus Point Drive
San Diego, CA 92121

Dr. Lawrence J. Burdick
Woodward-Clyde Consultants
P.O. Box 93245
Pasadena, CA 91109-3245 (2 copies)

Professor Robert W. Clayton
Seismological Laboratory/Div. of
Geological & Planetary Sciences
California Institute of Technology
Pasadena, CA 91125

Dr Karl Coyner
N. E. Research
P.O. Box 857
Norwich, VT 05055

Dr. Vernon F. Cormier
Department of Geology & Geophysics
U-45, Room 207
The University of Connecticut
Storrs, Connecticut 06268

Dr. Steven Day
Dept. of Geological Sciences
San Diego State U.
San Diego, CA 92182

Dr. Zoltan A. Der
ENSCO, Inc.
5400 Port Royal Road
Springfield, VA 22151-2388

Professor John Ferguson
Center for Lithospheric Studies
The University of Texas at Dallas
P.O. Box 830688
Richardson, TX 75083-0688

Professor Stanley Flatte'
Applied Sciences Building
University of California,
Santa Cruz, CA 95064

Dr. Alexander Florence
SRI International
333 Ravenswood Avenue
Menlo Park, CA 94025-3493

Professor Steven Grand
Department of Geology
245 Natural History Building
1301 West Green Street
Urbana, IL 61801

Dr. Henry L. Gray
Associate Dean of Dedman College
Department of Statistical Sciences
Southern Methodist University
Dallas, TX 75275

Professor Roy Greenfield
Geosciences Department
403 Deike Building
The Pennsylvania State University
University Park, PA 16802

Professor David G. Harkrider
Seismological Laboratory
Div of Geological & Planetary Sciences
California Institute of Technology
Pasadena, CA 91125

Professor Donald V. Helmberger
Seismological Laboratory
Div of Geological & Planetary Sciences
California Institute of Technology
Pasadena, CA 91125

Professor Eugene Herrin
Institute for the Study of Earth
and Man/Geophysical Laboratory
Southern Methodist University
Dallas, TX 75275

Professor Robert B. Herrmann
Department of Earth & Atmospheric
Sciences
Saint Louis University
Saint Louis, MO 63156

Professor Bryan Isacks
Cornell University
Dept of Geological Sciences
SNEE Hall
Ithaca, NY 14850

Professor Lane R. Johnson
Seismographic Station
University of California
Berkeley, CA 94720

Professor Thomas H. Jordan
Department of Earth, Atmospheric
and Planetary Sciences
Mass Institute of Technology
Cambridge, MA 02139

Dr. Alan Kafka
Department of Geology &
Geophysics
Boston College
Chestnut Hill, MA 02167

Professor Leon Knopoff
University of California
Institute of Geophysics
& Planetary Physics
Los Angeles, CA 90024

Professor Charles A. Langston
Geosciences Department
403 Deike Building
The Pennsylvania State University
University Park, PA 16802

Professor Thorne Lay
Department of Geological Sciences
1006 C.C. Little Building
University of Michigan
Ann Arbor, MI 48109-1063

Dr. Randolph Martin III
New England Research, Inc.
P.O. Box 857
Norwich, VT 05055

Dr. Gary McCartor
Mission Research Corp.
735 State Street
P.O. Drawer 719
Santa Barbara, CA 93102 (2 copies)

Professor Thomas V. McEvilly
Seismographic Station
University of California
Berkeley, CA 94720

Dr. Keith L. McLaughlin
S-CUBED,
A Division of Maxwell Laboratory
P.O. Box 1620
La Jolla, CA 92038-1620

Professor William Menke
Lamont-Doherty Geological Observatory
of Columbia University
Palisades, NY 10964

Professor Brian J. Mitchell
Department of Earth & Atmospheric
Sciences
Saint Louis University
Saint Louis, MO 63156

Mr. Jack Murphy
S-CUBED
A Division of Maxwell Laboratory
11800 Sunrise Valley Drive
Suite 1212
Reston, VA 22091 (2 copies)

Professor J. A. Orcutt
Institute of Geophysics and Planetary
Physics, A-205
Scripps Institute of Oceanography
Univ. of California, San Diego
La Jolla, CA 92093

Professor Keith Priestley
University of Nevada
Mackay School of Mines
Reno, NV 89557

Professor Paul G. Richards
Lamont-Doherty Geological
Observatory of Columbia Univ.
Palisades, NY 10964

Wilmer Rivers
Teledyne Geotech
314 Montgomery Street
Alexandria, VA 22314

Dr. Alan S. Ryall, Jr.
Center of Seismic Studies
1300 North 17th Street
Suite 1450
Arlington, VA 22209-2308 (4 copies)

Professor Charles G. Sammis
Center for Earth Sciences
University of Southern California
University Park
Los Angeles, CA 90089-0741

Professor Christopher H. Scholz
Geological Sciences
Lamont-Doherty Geological Observatory
Palisades, NY 10964

Dr. Jeffrey L. Stevens
S-CUBED,
A Division of Maxwell Laboratory
P.O. Box 1620
La Jolla, CA 92038-1620

Professor Brian Stump
Institute for the Study of Earth & Man
Geophysical Laboratory
Southern Methodist University
Dallas, TX 75275

Professor Ta-liang Teng
Center for Earth Sciences
University of Southern California
University Park
Los Angeles, CA 90089-0741

Dr. Clifford Thurber
State University of New York at
Stony Brooks
Dept of Earth and Space Sciences
Stony Brook, NY 11794-2100

Professor M. Nafi Toksoz
Earth Resources Lab
Dept of Earth, Atmospheric and
Planetary Sciences
Massachusetts Institute of Technology
42 Carleton Street
Cambridge, MA 02142

Professor Terry C. Wallace
Department of Geosciences
Building #11
University of Arizona
Tucson, AZ 85721

Weidlinger Associates
ATTN: Dr. Gregory Wojcik
4410 El Camino Real, Suite 110
Los Altos, CA 94022

Professor Francis T. Wu
Department of Geological Sciences
State University of New York
at Binghamton
Vestal, NY 13901

OTHERS (United States)

Dr. Monem Abdel-Gawad
Rockwell Internat'l Science Center
1049 Camino Dos Rios
Thousand Oaks, CA 91360

Professor Shelton S. Alexander
Geosciences Department
403 Deike Building
The Pennsylvania State University
University Park, PA 16802

Dr. Ralph Archuleta
Department of Geological
Sciences
Univ. of California at
Santa Barbara
Santa Barbara, CA

Dr. Muawia Barazangi
Geological Sciences
Cornell University
Ithaca, NY 14853

J. Barker
Department of Geological Sciences
State University of New York
at Binghamton
Vestal, NY 13901

Mr. William J. Best
907 Westwood Drive
Vienna, VA 22180

Dr. N. Biswas
Geophysical Institute
University of Alaska
Fairbanks, AK 99701

Dr. G. A. Bollinger
Department of Geological Sciences
Virginia Polytechnical Institute
21044 Derring Hall
Blacksburg, VA 24061

Dr. James Bulau
Rockwell Int'l Science Center
1049 Camino Dos Rios
P.O. Box 1085
Thousand Oaks, CA 91360

Mr. Roy Burger
1221 Serry Rd.
Schenectady, NY 12309

Dr. Robert Burrige
Schlumberger-Doll Resch Ctr.
Old Quarry Road
Ridgefield, CT 06877

Science Horizons, Inc.
ATTN: Dr. Theodore Cherry
710 Encinitas Blvd., Suite 101
Encinitas, CA 92024 (2 copies)

Professor Jon F. Claerbout
Professor Amos Nur
Dept. of Geophysics
Stanford University
Stanford, CA 94305 (2 copies)

Dr. Anton W. Dainty
AFGL/LWH
Hanscom AFB, MA 01731

Professor Adam Dziewonski
Hoffman Laboratory
Harvard University
20 Oxford St.
Cambridge, MA 02138

Professor John Ebel
Dept of Geology & Geophysics
Boston College
Chestnut Hill, MA 02167

Dr. Donald Forsyth
Dept. of Geological Sciences
Brown University
Providence, RI 02912

Dr. Anthony Gangi
Texas A&M University
Department of Geophysics
College Station, TX 77843

Dr. Freeman Gilbert
Institute of Geophysics &
Planetary Physics
Univ. of California, San Diego
P.O. Box 109
La Jolla, CA 92037

Mr. Edward Giller
Pacific Seirra Research Corp.
1401 Wilson Boulevard
Arlington, VA 22209

Dr. Jeffrey W. Given
Sierra Geophysics
11255 Kirkland Way
Kirkland, WA 98033

Rong Song Jih
Teledyne Geotech
314 Montgomery Street
Alexandria, Virginia 22314

Professor F.K. Lamb
University of Illinois at
Urbana-Champaign
Department of Physics
1110 West Green Street
Urbana, IL 61801

Dr. Arthur Lerner-Lam
Lamont-Doherty Geological Observatory
of Columbia University
Palisades, NY 10964

Dr. L. Timothy Long
School of Geophysical Sciences
Georgia Institute of Technology
Atlanta, GA 30332

Dr. Peter Malin
University of California at Santa Barbara
Institute for Central Studies
Santa Barbara, CA 93106

Dr. George R. Mellman
Sierra Geophysics
11255 Kirkland Way
Kirkland, WA 98033

Dr. Bernard Minster
Institute of Geophysics and Planetary
Physics, A-205
Scripps Institute of Oceanography
Univ. of California, San Diego
La Jolla, CA 92093

Professor John Nabelek
College of Oceanography
Oregon State University
Corvallis, OR 97331

Dr. Geza Nagy
U. California, San Diego
Dept of Ames, M.S. B-010
La Jolla, CA 92093

Dr. Jack Oliver
Department of Geology
Cornell University
Ithaca, NY 14850

Dr. Robert Phinney/Dr. F.A. Dahlen
Dept of Geological
Geophysical Sci. University
Princeton University
Princeton, NJ 08540 (2 copies)

RADIX Systems, Inc.
Attn: Dr. Jay Pulli
2 Taft Court, Suite 203
Rockville, Maryland 20850

Dr. Norton Rimer
S-CUBED
A Division of Maxwell Laboratory
P.O. 1620
La Jolla, CA 92038-1620

Professor Larry J. Ruff
Department of Geological Sciences
1006 C.C. Little Building
University of Michigan
Ann Arbor, MI 48109-1063

Dr. Richard Sailor
TASC Inc.
55 Walkers Brook Drive
Reading, MA 01867

Thomas J. Sereno, Jr.
Service Application Int'l Corp.
10210 Campus Point Drive
San Diego, CA 92121

Dr. David G. Simpson
Lamont-Doherty Geological Observ.
of Columbia University
Palisades, NY 10964

Dr. Bob Smith
Department of Geophysics
University of Utah
1400 East 2nd South
Salt Lake City, UT 84112

Dr. S. W. Smith
Geophysics Program
University of Washington
Seattle, WA 98195

Dr. Stewart Smith
IRIS Inc.
1616 N. Fort Myer Drive
Suite 1440
Arlington, VA 22209

Rondout Associates
ATTN: Dr. George Sutton,
Dr. Jerry Carter, Dr. Paul Pomeroy
P.O. Box 224
Stone Ridge, NY 12484 (4 copies)

Dr. L. Sykes
Lamont Doherty Geological Observ.
Columbia University
Palisades, NY 10964

Dr. Pradeep Talwani
Department of Geological Sciences
University of South Carolina
Columbia, SC 29208

Dr. R. B. Tittmann
Rockwell International Science Center
1049 Camino Dos Rios
P.O. Box 1085
Thousand Oaks, CA 91360

Professor John H. Woodhouse
Hoffman Laboratory
Harvard University
20 Oxford St.
Cambridge, MA 02138

Dr. Gregory B. Young
ENSCO, Inc.
5400 Port Royal Road
Springfield, VA 22151-2388

OTHERS (FOREIGN)

Dr. Peter Basham
Earth Physics Branch
Geological Survey of Canada
1 Observatory Crescent
Ottawa, Ontario
CANADA K1A 0Y3

Ms. Eva Johannisson
Senior Research Officer
National Defense Research Inst.
P.O. Box 27322
S-102 54 Stockholm
SWEDEN

Dr. Eduard Berg
Institute of Geophysics
University of Hawaii
Honolulu, HI 96822

Tormod Kvaerna
NTNF/NORSAR
P.O. Box 51
N-2007 Kjeller, NORWAY

Dr. Michel Bouchon - Universite
Scientifique et Medicale de Grenob
Lab de Geophysique - Interne et
Tectonophysique - I.R.I.G.M-B.P.
38402 St. Martin D'Herès
Cedex FRANCE

Mr. Peter Marshall, Procurement
Executive, Ministry of Defense
Blacknest, Brimpton,
Reading RG7-4RS
UNITED KINGDOM (3 copies)

Dr. Hilmar Bungum/NTNF/NORSAR
P.O. Box 51
Norwegian Council of Science,
Industry and Research, NORSAR
N-2007 Kjeller, NORWAY

Dr. Ben Menaheim
Weizman Institute of Science
Rehovot, ISRAEL 951729

Dr. Michel Campillo
I.R.I.G.M.-B.P. 68
38402 St. Martin D'Herès
Cedex, FRANCE

Dr. Svein Mykkeltveit
NTNF/NORSAR
P.O. Box 51
N-2007 Kjeller, NORWAY (3 copies)

Dr. Kin-Yip Chun
Geophysics Division
Physics Department
University of Toronto
Ontario, CANADA M5S 1A7

Dr. Robert North
Geophysics Division
Geological Survey of Canada
1 Observatory crescent
Ottawa, Ontario
CANADA, K1A 0Y3

Dr. Alan Douglas
Ministry of Defense
Blacknest, Brimpton,
Reading RG7-4RS
UNITED KINGDOM

Dr. Frode Ringdal
NTNF/NORSAR
P.O. Box 51
N-2007 Kjeller, NORWAY

Dr. Manfred Henger
Fed. Inst. For Geosciences & Nat'l Res.
Postfach 510153
D-3000 Hannover 51
FEDERAL REPUBLIC OF GERMANY

Dr. Jorg Schlittenhardt
Federal Inst. for Geosciences & Nat'l Res.
Postfach 510153
D-3000 Hannover 51
FEDERAL REPUBLIC OF GERMANY

Dr. E. Husebye
NTNF/NORSAR
P.O. Box 51
N-2007 Kjeller, NORWAY

University of Hawaii
Institute of Geophysics
ATTN: Dr. Daniel Walker
Honolulu, HI 96822

FOREIGN CONTRACTORS

Dr. Ramon Cabre, S.J.
c/o Mr. Ralph Buck
Economic Consular
American Embassy
APO Miami, Florida 34032

Professor Peter Harjes
Institute for Geophysik
Rhur University/Bochum
P.O. Box 102148, 4630 Bochum 1
FEDERAL REPUBLIC OF GERMANY

Professor Brian L.N. Kennett
Research School of Earth Sciences
Institute of Advanced Studies
G.P.O. Box 4
Canberra 2601
AUSTRALIA

Dr. B. Massinon
Societe Radiomana
27, Rue Claude Bernard
7,005, Paris, FRANCE (2 copies)

Dr. Pierre Mechler
Societe Radiomana
27, Rue Claude Bernard
75005, Paris, FRANCE

GOVERNMENT

Dr. Ralph Alewine III
DARPA/NMRO
1400 Wilson Boulevard
Arlington, VA 22209-2308

Dr. Robert Blandford
DARPA/NMRO
1400 Wilson Boulevard
Arlington, VA 22209-2308

Sandia National Laboratory
ATTN: Dr. H. B. Durham
Albuquerque, NM 87185

Dr. Jack Evernden
USGS-Earthquake Studies
345 Middlefield Road
Menlo Park, CA 94025

U.S. Geological Survey
ATTN: Dr. T. Hanks
Nat'l Earthquake Resch Center
345 Middlefield Road
Menlo Park, CA 94025

Dr. James Hannon
Lawrence Livermore Nat'l Lab.
P.O. Box 808
Livermore, CA 94550

Paul Johnson
ESS-4, Mail Stop J979
Los Alamos National Laboratory
Los Alamos, NM 87545

Ms. Ann Kerr
DARPA/NMRO
1400 Wilson Boulevard
Arlington, VA 22209-2308

Dr. Max Koontz
US Dept of Energy/DP 5
Forrestal Building
1000 Independence Ave.
Washington, D.C. 20585

Dr. W. H. K. Lee
USGS
Office of Earthquakes, Volcanoes,
& Engineering
Branch of Seismology
345 Middlefield Rd
Menlo Park, CA 94025

Dr. William Leith
USGS
Mail Stop 928
Reston, VA 22092

Dr. Richard Lewis
Dir. Earthquake Engineering and
Geophysics
U.S. Army Corps of Engineers
Box 631
Vicksburg, MS 39180

Dr. Robert Masse'
Box 25046, Mail Stop 967
Denver Federal Center
Denver, Colorado 80225

Richard Morrow
ACDA/VI
Room 5741
320 21st Street N.W.
Washington, D.C. 20451

Dr. Keith K. Nakanishi
Lawrence Livermore National Laboratory
P.O. Box 808, L-205
Livermore, CA 94550 (2 copies)

Dr. Carl Newton
Los Alamos National Lab.
P.O. Box 1663
Mail Stop C335, Group E553
Los Alamos, NM 87545

Dr. Kenneth H. Olsen
Los Alamos Scientific Lab.
Post Office Box 1663
Los Alamos, NM 87545

Howard J. Patton
Lawrence Livermore National
Laboratory
P.O. Box 808, L-205
Livermore, CA 94550

Mr. Chris Paine
Office of Senator Kennedy
SR 315
United States Senate
Washington, D.C. 20510

AFOSR/NP
ATTN: Colonel Jerry J. Perrizo
Bldg 410
Bolling AFB, Wash D.C. 20332-6448

HQ AFTAC/TT
Attn: Dr. Frank F. Pilotte
Patrick AFB, Florida 32925-6001

Mr. Jack Rachlin
USGS - Geology, Rm 3 C136
Mail Stop 928 National Center
Reston, VA 22092

Robert Reinke
AFWL/NTEG
Kirtland AFB, NM 87117-6008

HQ AFTAC/TGR
Attn: Dr. George H. Rothe
Patrick AFB, Florida 32925-6001

Donald L. Springer
Lawrence Livermore National Laboratory
P.O. Box 808, L-205
Livermore, CA 94550

Dr. Lawrence Turnbull
OSWR/NED
Central Intelligence Agency
CIA, Room 5G48
Washington, D.C. 20505

Dr. Thomas Weaver
Los Alamos Scientific Laboratory
Los Alamos, NM 97544

AFGL/SULL
Research Library
Hanscom AFB, MA 01731-5000 (2 copies)

Secretary of the Air Force (SAFRD)
Washington, DC 20330
Office of the Secretary Defense
DDR & E
Washington, DC 20330

HQ DNA
ATTN: Technical Library
Washington, DC 20305

DARPA/RMO/RETRIEVAL
1400 Wilson Blvd.
Arlington, VA 22209

DARPA/RMO/Security Office
1400 Wilson Blvd.
Arlington, VA 22209

AFGL/XO
Hanscom AFB, MA 01731-5000

AFGL/LW
Hanscom AFB, MA 01731-5000

DARPA/PM
1400 Wilson Boulevard
Arlington, VA 22209

Defense Technical
Information Center
Cameron Station
Alexandria, VA 22314
(5 copies)

Defense Intelligence Agency
Directorate for Scientific &
Technical Intelligence
Washington, D.C. 20301

Defense Nuclear Agency/SPSS
ATTN: Dr. Michael Shore
6801 Telegraph Road
Alexandria, VA 22310

AFTAC/CA (STINFO)
Patrick AFB, FL 32925-6001

Dr. Gregory van der Vink
Congress of the United States
Office of Technology Assessment
Washington, D.C. 20510

Mr. Alfred Lieberman
ACDA/VI-OA'State Department Building
Room 5726
320 - 21st Street, NW
Washington, D.C. 20451

TACTEC
Battelle Memorial Institute
505 King Avenue
Columbus, OH 43201 (Final report only)